

# Microstructure and Mechanical Properties of Cold Sprayed Aluminum and Titanium Alloys

by

Trevor Graham Bond

A Thesis

Submitted to the Faculty

of the

WORCESTER POLYTECHNIC INSTITUTE

In partial fulfillment of the requirements for the

Degree of Master of Science

in

Mechanical Engineering

November 2019

APPROVED:

Winston Soboyejo, Major Advisor

Cagdas Onal, Graduate Committee Representative

Danielle Cote, Committee Member

Carl Soderhjelm, Committee Member

## Abstract

A combination of experimental and computational methods is used to explore the microstructure and mechanical behavior of cold sprayed 6061 aluminum alloy and Ti-6Al-4V alloy and their substrate materials. A variety of microscopic methods are used for characterization of the microstructure. The indentation size effect and characteristic length of strain gradient plasticity for the substrate materials are determined. An FEA simulation describes the behavior of a worn Berkovich nanoindenter. Stress strain is studied experimentally in the substrate materials for future comparison with bulk cold-sprayed materials. Abaqus FEA models are used to simulate a single particle impact for a particle with an oxide layer using a linear Johnson-Cook plasticity model and a bilinear Johnson-Cook plasticity model. The implications of the results are discussed for cold spray processes.

## Preface

I want to extend my gratitude to all of those who supported me academically; my advisor, Wole Soboyejo, and professors in our research group; John Obayemi, Nima Rahbar, Oluwaseun (Kenny) Oyewole, Adebayo Badmos, and Vahid Rahneshin. Randy Paffenroth graciously provided his support and advice for the data science aspects of the work. In addition, the rest of our research group provided me with valuable guidance throughout the work. I also would like to thank my wife for supporting and motivating me to produce my best work. The work was funded and supported by the Army Research Lab (ARL). This paper would not have been possible without all of your help.

As an enthusiastic supporter of scientific advancement, I have made data and programs that I have generated available for public use wherever possible. I hope it can be of future benefit. Likewise, please feel welcome to reach out to me with questions or requests for original data.

## Table of Contents

Abstract.....	2
Preface .....	2
List of Figures .....	5
List of Tables .....	9
List of Equations.....	10
Chapter 1: Background and Scope.....	12
1.1    Background .....	12
1.1.1 Cold Spray Overview .....	12
1.1.2 Powder Production .....	12

1.1.3 Cold Spray Parameters.....	14
1.1.4 Mechanism of Cold Spray Bonding .....	15
1.2 Unresolved Issues .....	17
1.3 Scope of Current Work.....	17
Chapter 2: Literature Survey.....	18
2.1 Microstructure and Physical Metallurgy of Aluminum Alloys .....	18
2.1.1 Bulk 6061 Aluminum Alloy Metallurgy and Microstructure .....	18
2.1.2 6061 Aluminum Alloy Powder Microstructure .....	19
2.1.3 Bulk Cold Sprayed 6061 Aluminum Alloy Microstructure.....	20
2.1.4 Bulk Cold Sprayed 6061 Aluminum Alloy Mechanical Properties.....	22
2.2 Microstructure and Physical Metallurgy of Titanium Alloys.....	23
2.2.1 Commercially Pure Titanium Metallurgy and Microstructure .....	23
2.2.2 Bulk Ti-6Al-4V Metallurgy .....	24
2.3.3 Ti-6Al-4V Powder Metallurgy and Microstructure .....	26
2.3.4 Bulk Cold Sprayed Ti-6Al-4V Microstructure .....	28
2.3.5 Bulk Cold Sprayed Ti-6Al-4V Mechanical Properties .....	29
2.3 The Indentation Size Effect .....	32
2.3.1 Statistically Stored Dislocations .....	32
2.3.2 Geometrically Necessary Dislocations .....	32
2.3.3 Experimental Determination of Hardness .....	33
2.3.4 Discrete Dislocations.....	35
2.3.5 Material Length Scale.....	36
2.3.6 Nanoindentation Methods .....	37
2.3.7 Microhardness Methods.....	37
2.3.8 Corrections for Non-Ideal Geometries.....	39
2.3.9 Current Experimental Results for Aluminum and Titanium Alloys .....	40
2.4 Fracture.....	43
2.4.1 General Discussion.....	43
2.4.2 Wrought 6061 Aluminum Alloy .....	45
2.4.3 Cold Sprayed 6061 Aluminum Alloy.....	48
2.4.4 Ti-6Al-4V Bulk Material .....	48
2.4.5 Cold Sprayed Ti-6Al-4V.....	50

2.5.6 Fracture of Cold Spray Coatings.....	50
2.5 Fatigue.....	52
2.5.1 General Discussion.....	52
2.5.2 Wrought 6061 Aluminum Alloy .....	54
2.5.3 Cold Sprayed 6061 Aluminum Alloy.....	55
2.5.4 Ti-6Al-4V Bulk Material .....	56
2.5.5 Cold Sprayed Ti-6Al-4V.....	57
2.6 Data Science Approach to Materials Science.....	58
2.6.1 Introduction to Data Science Methods.....	58
2.6.2 Applications of Data Science in Materials Science.....	67
Chapter 3: Microstructure and Mechanical Properties of Extruded 6061 Aluminum and Cold-sprayed 6061 Aluminum Alloys .....	68
3.1 Microstructure of Aluminum – Magnesium - Silicon Alloy 6061 .....	68
3.1.1 6061 Aluminum Alloy Plate.....	68
3.1.2 6061 Aluminum Alloy Powder .....	73
3.2 Stress-Strain Behavior of 6061 Aluminum Alloy .....	75
3.3 Indentation Size Effect in 6061 Aluminum Alloys.....	81
3.3.1 Vickers Microhardness.....	81
3.3.2 Simulation of Low Load Nanoindentation with an Imperfect Berkovich Tip.....	85
3.4 Prediction of Hardness Using Machine Learning and Microstructural Images .....	87
3.5 Simulation of Cold Spray 6061 Impact- Effect of Oxide Layer .....	89
3.6 Fatigue of 6061 Aluminum Alloy.....	94
3.7 Implications.....	97
Chapter 4: Microstructure and Mechanical Properties of Extruded CP Ti, Ti-6Al-4V and Cold-sprayed Ti-6Al-4V.....	99
4.1 Microstructure of Titanium Alloys .....	99
4.1.1 Ti-6Al-4V Rod and Plate .....	99
4.1.2 Commercially Pure Titanium Powder .....	102
4.1.3 Ti-6Al-4V Powder .....	104
4.2 Stress-Strain Behavior of Titanium Alloys.....	106
4.3 Indentation Size Effect in CP Titanium and Ti-6Al-4V .....	109
4.3.1 Vickers Microhardness.....	109

4.3.2 Simulation of Low Load Ti-6Al-4V Nanoindentation with Imperfect Berkovich Tip .....	110
4.4 Simulation of Cold Spray Ti-6Al-4V Impact .....	113
4.5 Implications.....	117
Chapter 5: Conclusions and Future Work .....	119
5.1 Conclusions of 6061 Aluminum Alloy Findings .....	119
5.2 Conclusions of Ti-6Al-4V Findings .....	119
5.3 Future Work .....	119
References .....	121
Appendix .....	130
A1.1 Additional Reference Images.....	130

## List of Figures

Figure 1: Relative deposition efficiency and part fidelity of various additive manufacturing processes...	12
Figure 2: Gas Atomization Process.....	13
Figure 3: Simplified diagram of components in cold spray process .....	14
Figure 4: Typical powder diameters for different materials.....	15
Figure 5: Particle impact response at different velocities .....	16
Figure 6: Proposed shock wave bonding mechanism.....	16
Figure 7: 6061-T6 sheet with insoluble $(Fe,Cr)_3SiAl_{12}$ (lighter gray color) and excess soluble $Mg_2Si$ particles (darker color).....	18
Figure 8: 6061 Aluminum alloy powder particle size distribution .....	19
Figure 9: 6061 Aluminum alloy powder morphology and microstructure .....	20
Figure 10: Cross section of sprayed 6061 plate and size distribution of the particle splats .....	20
Figure 11: Cross section of cold sprayed 6061 aluminum alloy deposit with red arrows highlighting voids and porosity between particles .....	21
Figure 12: Nanoscale precipitates in cold spray deposit .....	21
Figure 13: Tensile properties of wrought and cold-sprayed 6061 aluminum alloy.....	22
Figure 14: Varying grain structure of CP titanium etched with Kroll's reagent showing lighter colored alpha grains and dark spots of iron-stabilized beta phase .....	24
Figure 15: Hydride needles formed in CP titanium.....	24
Figure 16: Diagram showing primary $\alpha$ , transformation $\alpha$ , and retained $\beta$ .....	25
Figure 17: Annealed Ti-6Al-4V ELI (R56401) showing primary alpha grains and alpha-beta matrix structure.....	26
Figure 18: Exterior cellular structure (a) and interior lathe structures (b) in Ti-6Al-4V .....	27
Figure 19: Particles produced by the Armstrong process showing porosity and non-uniform topography (a) and equiaxed alpha microstructure (b) .....	27

Figure 20: Particles produced by the hydride-dehydride process with angular morphology (a) and equiaxed alpha grain structure with intergranular beta (b) .....	28
Figure 21: Ti-6Al-4V deposits with 0.3% porosity and 8.1% porosity sprayed with helium and nitrogen gas respectively .....	29
Figure 22: Ti-6Al-4V deposits showing equiaxed/elongated grains.....	29
Figure 23: Typical stress-strain curves for Ti-6Al-4V substrate, helium and nitrogen sprayed coatings and coatings after heat treatment.....	30
Figure 24: Vickers microhardness measurements on Ti-6Al-4V cold spray coatings .....	31
Figure 25: Particle debonding during microindentation.....	32
Figure 26: Schematic representing theory of geometrically necessary dislocations.....	33
Figure 27: Hardness as a function of plastic depth for silver single crystals .....	33
Figure 28: Linearized relationship between hardness and depth. The slope of the line is $h^*$ while the y intercept is $H_0$ . Experimentally finding the hardness based upon statistically stored dislocations .....	34
Figure 29: Dislocation mechanics scales .....	35
Figure 30: Diagram representing discrete dislocation theory .....	36
Figure 31: Diagram of Vickers indentation .....	38
Figure 32: Diagram showing pile-up .....	39
Figure 33: Indenter tip rounding diagram .....	39
Figure 34: Transition from spherical to sharp indenter .....	40
Figure 35: Average indentation stress, $\sigma_{ind}$ , versus indentation depth, $h$ , for 6061 aluminum alloy test material, indented at four loading rates, in 6061-O (a), and 6061-T6 (b) conditions .....	41
Figure 36: Linearized Meyer's harnesses from an instrumented Vickers hardness tester .....	42
Figure 37: Fracture modes .....	44
Figure 38: Crack-tip shielding mechanisms.....	45
Figure 39: Relationship between yield strength and KIC for aluminum alloys.....	46
Figure 40: Impact of Fe and Si content on fracture toughness of aluminum alloys .....	48
Figure 41: Fractography of a Ti-6Al-4V coating showing crack propagation along intersplat boundaries. 50	
Figure 42: Mode mixity of an interfacial crack .....	51
Figure 43: Four-point bending delamination specimen .....	52
Figure 44: Idealized crack growth cycle with three primary regimes.....	53
Figure 45: Fatigue crack growth rates for various aluminum alloys.....	55
Figure 46: Applied (a) and closure-corrected (b) long and small fatigue crack growth data for annealed 6061 cold-spray and rolled 6061-T6 alloys .....	56
Figure 47: Fatigue crack growth rate versus stress and effective stress intensity factor ranges for Ti-6Al-4V .....	57
Figure 48: Encoding the seasons using the unit circle .....	59
Figure 49: Example of overfitting on roughly linear data .....	60
Figure 50: Bias-variance tradeoff.....	60
Figure 51: Data points from sine wave with a linear fit.....	62
Figure 52: Noisy Sine Wave Decision Tree Regression .....	63
Figure 53: Transformation of data using PCA .....	64
Figure 54: Simple feed forward neural network.....	66

Figure 55: Gradient descent diagram .....	66
Figure 56: Inverted reflective light microscope color image of 6061-O aluminum (S13) polished with colloidal silica .....	68
Figure 57: Inverted reflective light microscope color image of 6061-T6 aluminum (S11) etched for 55s using Keller’s Reagent .....	69
Figure 58: 6061-T6 aluminum (S8) top of plate section- etched with Keller’s Reagent for 55s using a visual light microscope (a), with a polarizing filter (b). Below the images is a histogram of the grain diameters seen (c).....	70
Figure 59: Electron interaction volume for different datatypes (a) .....	71
Figure 60: SEM image with EDS inserts on 6061-O aluminum (S2) polished with AlO <sub>2</sub> and unetched. ....	71
Figure 61: SEM topographic image with EDS inserts identifying existing elements at specific points.....	72
Figure 62: Particle size distribution of gas-atomized 6061 powders.....	73
Figure 63: Gas atomized 6061 aluminum alloy powder showing size and shape of powders as well as cellular structures on the surface of the powders.....	74
Figure 64: Inverted light microscope dark-field image of 6061 aluminum alloy powders (P1) mounted in a phenolic epoxy and polished with colloidal silica (a). Histogram of grain boundary diameters within the powder (b).....	75
Figure 65: 6061 aluminum alloy tensile specimen dimensions in mm.....	76
Figure 66: 6061-T6 aluminum wrought plate true stress versus true strain. ....	77
Figure 67: Methodology for finding Ramberg-Osgood parameters using a linear fit of the log-log stress strain curve within the plastic zone .....	78
Figure 68: Ramberg-Osgood representations of lateral and longitudinal samples compared with the raw true stress-strain curve from a longitudinal sample of 6061-T6 aluminum alloy.....	79
Figure 69: SEM images of a tensile specimen (S17) cross-section after testing show a reduction in cross-sectional area (a) and ductile dimples (b), characteristic of necking .....	81
Figure 70: Hardness versus depth in two samples of annealed 6061 aluminum alloy .....	82
Figure 71: Hardness versus depth in 6061-T6 aluminum plate of indents on the top face of the plate....	82
Figure 72: Plot of $H^2$ to $1/h$ used to find the value of $H_0$ for 6061-O aluminum.....	83
Figure 73: Linearized plot of hardness and indentation depth for 6061-O aluminum alloy .....	84
Figure 74: Cut-away of 3D Von Mises stress plot showing multiple stress profiles .....	86
Figure 75: 3D plot of vertical displacement in vertical direction (a) and along path marked on plot (b) ..	86
Figure 76: Zone of yielded material with criteria that 75% of the element exceed the yield strength .....	87
Figure 77: Etched surface of 6061 aluminum samples before (a) and after indentation (b) .....	88
Figure 78: Plot of tensor image input (a) into autoencoder and output (b) of autoencoder.....	89
Figure 79: Stress evolution of 6061 aluminum alloy particle impact on 6061 aluminum alloy substrate using Johnson-Cook plasticity mode at velocity of 770 m/s.....	90
Figure 80: Stress evolution of 6061 aluminum alloy particle impact on 6061 substrate using Johnson-Cook plasticity with 5 nm aluminum oxide layers at 770 m/s.....	91
Figure 81: Stress evolution over time for 6061 aluminum alloy particle impact on 6061 substrate using bilinear Johnson-Cook plasticity mode at 770 m/s.....	92
Figure 82: Stress evolution over time for 6061 aluminum alloy particle impact on 6061 substrate using bilinear Johnson-Cook plasticity model with 5 nm oxide layers at 770 m/s .....	93

Figure 83: Aluminum oxide layer left after 100 ns in the bilinear Johnson-Cook simulation at 500 m/s (a) and 900 m/s (b).....	94
Figure 84: Three point bend representative fixture .....	94
Figure 85: Fracture specimen used in bulk material work (dimensions in mm) (a). Strait through narrow notch criteria (b) .....	95
Figure 86: Fatigue loading conditions used for 6061 aluminum alloy SEB samples.....	96
Figure 87: Crack growth at different stress concentrations for a 6061 aluminum alloy single edged bend specimen .....	97
Figure 88: Ti-6Al-4V rod cross-section taken with a visual light microscope revealing lighter colored equiaxed grains of $\alpha$ phase (HCP) and darker sections of discontinuous $\beta$ phase (BCC). Etched with Kroll's reagent by swabbing with q-tip for 20s. ....	99
Figure 89: Ti-6Al-4V taken with a visual light microscope showing equiaxed grains across the extrusion direction (longitudinal cross-section)(a), but elongated grains along the extrusion direction (lateral cross-section)(b). Etched with Kroll's reagent by swabbing with q-tip for 20s.....	100
Figure 90: SEM topographic image with EDS data taken at two locations confirming $\alpha$ and $\beta$ phases in Ti-6Al-4V. Etched with Kroll's reagent by swabbing with a q-tip for 20s.....	101
Figure 91: Three dimensional composite visual light microscopy image showing the etched cross-sections of Ti-6Al-4V plate in each direction .....	102
Figure 92: Particle size distribution of gas-atomized commercially pure titanium powders .....	103
Figure 93: External topography of CP-Ti powder showing evidence of rapid solidification.....	103
Figure 94: Cross-section of CP-Ti powder etched with Kroll's reagent for 10s to show acicular microstructure. Powders were mounted in a phenolic epoxy and polished before etching. ....	104
Figure 95: Particle size distribution of gas-atomized Ti-6Al-4V powders .....	105
Figure 96: SEM topographic image of Ti-6Al-4V powders showing plate-like (a) and cellular grain structures (b).....	105
Figure 97: Cross-section of Ti-6Al-4V powder etched with Kroll's reagent for 10s to show acicular microstructure. Powders were mounted in a phenolic epoxy and polished before etching. ....	106
Figure 98: Stress strain curves of Ti-6Al-4V tensile samples in longitudinal and lateral directions .....	107
Figure 99: Ramberg-Osgood representations of lateral and longitudinal samples compared with the raw true stress-strain curve from a longitudinal sample of Ti-6Al-4V.....	107
Figure 100: SEM images of Ti-6Al-4V fracture surfaces show a moderate amount of necking, as well as shear at a $45^\circ$ angle to the loading axis .....	109
Figure 101: Hardness versus depth for commercially pure grade 2 titanium rod showing ISE.....	109
Figure 102: Hardness versus depth for Ti-6Al-4V rod showing ISE in two material orientations .....	110
Figure 103: Von-Mises stress in Berkovich indent of Ti-6Al-4V .....	111
Figure 104: Surface topography scan using Berkovich tip for contact measurement.....	112
Figure 105: Measurements of pileup along paths using experimental data from AFM in Gwyddion (a) as well as Abaqus (b) .....	113
Figure 106: Stress evolution of an 800m/s Ti-6Al-4V particle impacting Ti-6Al-4V substrate without an oxide layer and using Johnson-Cook plasticity .....	114
Figure 107: Stress evolution of Ti-6Al-4V particle impacting Ti-6Al-4V substrate with a titanium dioxide layer and using Johnson-Cook plasticity for Ti-6Al-4V.....	115

Figure 108: Stress evolution of an 800m/s Ti-6Al-4V particle impacting a Ti-6Al-4V substrate using bilinear Johnson-Cook plasticity .....	116
Figure 109: Stress evolution of an 800m/s Ti-6Al-4V particle impacting Ti-6Al-4V substrate with a titanium dioxide layer and using Johnson-Cook plasticity.....	116
Figure 110: Stress evolution of a 1020 m/s Ti-6Al-4V particle oxide layer impacting Ti-6Al-4V substrate using bilinear Johnson-Cook plasticity.....	117
Figure 111: : Titanium oxide layer left after 100 ns in the bilinear Johnson-Cook simulation at 600 m/s (a) and 1300 m/s (b).....	117

## List of Tables

Table 1: Composition of wrought 6061 aluminum alloy plate .....	18
Table 2: Comparison of 6061 aluminum alloy CS deposit mechanical properties with that of wrought 6061 .....	23
Table 3: Composition of grade 2 commercially pure titanium .....	23
Table 4: Composition of Ti-6Al-4V-ELI .....	25
Table 5: Composition of Ti-6Al-4V Powder.....	26
Table 6: Variation of statistically stored hardness, H <sub>0</sub> , and characteristic length, h* with quenching temperature.....	42
Table 7: Hardness and modulus comparison for wrought 6061-T6 aluminum and 6061-T6 cold spray powder deposits .....	43
Table 8: Nanohardness of Ti-6Al-4V cold spray coatings compared with bulk Ti-6Al-4V plate.....	43
Table 9: Fracture toughness of common structural alloys from CT specimens.....	46
Table 10: Impact of interrupted aging and secondary hardening on fracture toughness of aluminum alloys .....	47
Table 11: Comparison of mean values of J <sub>c</sub> for various specimen geometries and alloys.....	47
Table 12: Titanium structural alloys dependence of fracture toughness on alpha phase morphology.....	49
Table 13: Impact of hydrogen and oxygen content on Ti-6Al-4V mode I fracture toughness .....	49
Table 14: Impact of processing texture on tensile properties and K <sub>Ic</sub> .....	49
Table 15: Example dataset showing unscaled predictors and responses.....	59
Table 16: Composition of 6061 aluminum alloy plate used in this work as reported by manufacturer ....	68
Table 17: 6061-T6 mechanical reference parameters.....	80
Table 18: Summary of 6061-T6 aluminum mechanical properties found during tensile testing .....	80
Table 19: Summary of material parameters found by applying Nix and Gao's methods to Vickers microindentation of 6061 aluminum alloys.....	84
Table 20: Parameters used in 6061 aluminum alloy cold spray particle impact simulation .....	90
Table 21: Composition of Ti-6Al-4V rod as reported by the manufacturer.....	99
Table 22: Ti-6Al-4V mechanical reference parameters .....	108
Table 23: Summary of Ti-6AL-4V mechanical properties found during tensile testing .....	108
Table 24: Summary of material parameters found by applying Nix and Gao's methods to Vickers microindentation of 6061 aluminum alloy .....	110

Table 25: Parameters used in Ti-6Al-4V cold spray particle impact simulation .....	114
--	-----

## List of Equations

Equation 1: Nix and Gao linearized ISE relationship.....	34
Equation 2: Characteristic length from statistically stored dislocation hardness.....	34
Equation 3: Material length scale.....	36
Equation 4: Material length scale from statistically stored dislocations.....	36
Equation 5: SSD hardness.....	37
Equation 6: Density of statistically stored dislocations.....	37
Equation 7: Mean contact pressure/ Meyer’s hardness.....	37
Equation 8: Reduced modulus.....	37
Equation 9: Surface area of Vickers indenter tip.....	38
Equation 10: Vickers hardness from load and area.....	38
Equation 11: Projected area for Vickers tip geometry.....	38
Equation 12: Tip rounding geometrical correction.....	40
Equation 13: Correction for true indent depth.....	40
Equation 14: Tip area function calibration.....	40
Equation 15: Relation of fraction toughness to strain energy release rate.....	44
Equation 16: Recommended ligament size for aluminum alloy KIC measurements.....	48
Equation 17: Dundurs' parameters.....	51
Equation 18: Elastic parameter based on Dundurs' parameter $\beta$ .....	51
Equation 19: Strain energy release rate for interfacial cracks.....	52
Equation 20: Phase angle of loading for describing mode mixity.....	52
Equation 21: Strain energy release rate for delamination in four-point bend specimen.....	52
Equation 22: Paris’ law.....	53
Equation 23: Multi-parameter crack propagation model.....	54
Equation 24: Euclidian Distance.....	58
Equation 25: Z score normalization.....	58
Equation 26: Mean-squared error.....	61
Equation 27: Linear regression.....	62
Equation 28: First principal component.....	64
Equation 29: Lasso regression.....	65
Equation 30: Gradient descent.....	67
Equation 31: Total strain is the sum of elastic and plastic components.....	77
Equation 32: Ramberg-Osgood relationship.....	77
Equation 33: Hollomon Strain Hardening.....	77

Equation 34: Strain hardening coefficient from stress strain data.....	78
Equation 35: Density of statistically stored dislocations.....	84
Equation 36: Johnson-Cook plasticity model.....	89
Equation 37: Linear-elastic stress concentration for SEB specimen.....	95
Equation 38: Geometric constant based on ratio of crack length to specimen height.....	95
Equation 39: Simplified linear-elastic stress concentration for SEB sample.....	95
Equation 40: Load for SEB specimen given stress concentration.....	96

## Chapter 1: Background and Scope

### 1.1 Background

#### 1.1.1 Cold Spray Overview

Cold spray (CS), also called Cold Gas Dynamic Spray (CGDS), is an additive manufacturing technology which allows for dense deposition of materials at temperatures below their respective melting points. The process accelerates micro-sized particles to high velocities (typically 300 m/s to 1200 m/s, but dependent upon the material) to adhere to various substrates (Moridi et al. 2014, Schmidt et al. 2006). CS has the benefit of avoiding residual tensile stresses and oxidation issues for various materials which may be produced using thermal energy technologies. The technology is also able to approach produce deposits approaching 99% density in some materials and can have mechanical properties near that of wrought materials (Champagne and Helfritch 2014). CS has been used in industry to coat various metal substrates with thin layers of other metals as well as dimensional repair in corroded or damaged metal parts (Champagne 2008). Research has been conducted into use of CS technology for composites, polymers, and ceramics (Moridi 2014). The CS process has much higher deposition rates than most other additive manufacturing techniques and has been employed for the creation of near net shape parts (Pattison et al. 2007). Cold spray has the disadvantages of poor surface finish and dimensional control as well as high cost of helium used for the higher velocity sprays.

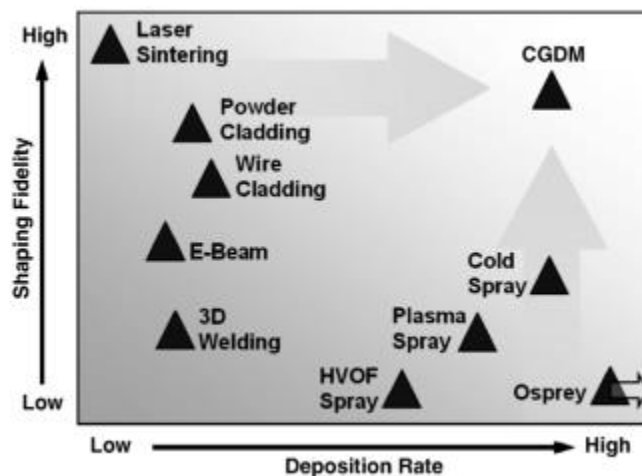


Figure 1: Relative deposition efficiency and part fidelity of various additive manufacturing processes (Pattison et al. 2007)

#### 1.1.2 Powder Production

The powders produced for cold spray make use of many of the existing methods of powder production for thermal spray and sintering processes. Atomization processes are often used for

metallic and polymer powders for a more consistent spherical shape, while mechanical crushing processes are frequently used for high temperature alloys and ceramics (Neikov, 2009).

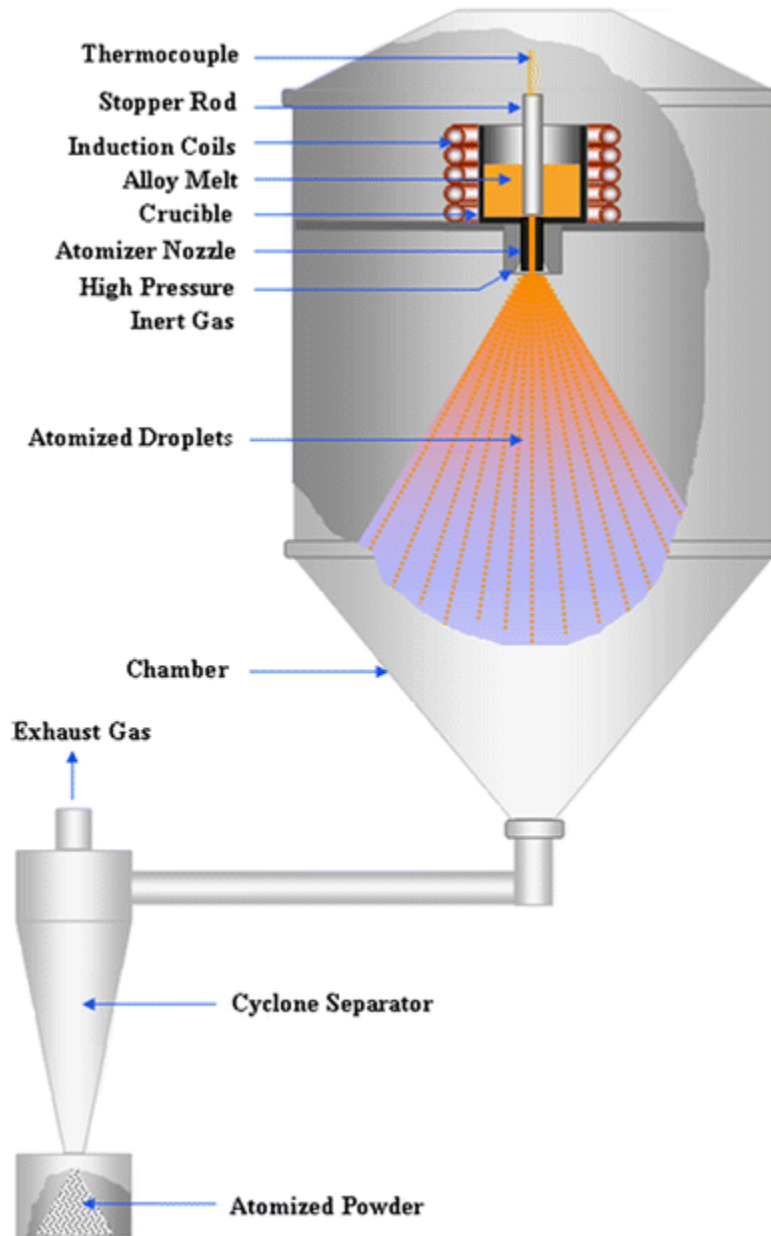


Figure 2: Gas Atomization Process (Zheng et al. 2009)

Production of refractory metal powders typically involves hydriding for purposeful embrittlement and crushing or milling of the bulk material. The subsequent powders have oxides removed by heating with magnesium and the hydrides removed by chemical leaching (Yang, 2019, Neikov, 2009).

### 1.1.3 Cold Spray Parameters

Cold Spray is a technology which allows for the deposition of various materials at a high rate and high density through the use of a fine particle spray at high velocities. This process deposits the solid state particles at well below their melting points and only provides extremely localized heating to the substrate surface being sprayed onto. In order to adhere to the surface of a substrate the particle velocity must hit a critical velocity which is high enough to keep the particle from rebounding from the surface. Velocities above the critical velocity will provide better adhesion to the surface up to a limit. Particles in experiments with explosives and micro-asteroid impacts with velocities from 1000 – 3000 m/s have caused super-deep penetration (defined as penetration distances  $10^3$ - $10^4$  times the particle diameter) and damage to the surfaces they contact (Klinkov et al. 2005). Typically critical velocities range from 300 to 1200 m/s depending upon the specific properties of the powder feedstock and the substrate. The basic components of cold spray technology are the following (Moridi et al. 2014, Champagne and Barnett 2012, Kay and Karthikeyan 2016):

- Solid powder feedstock
- High pressure supply gas
- Nozzle- typically convergent-divergent to increase gas and particle velocity

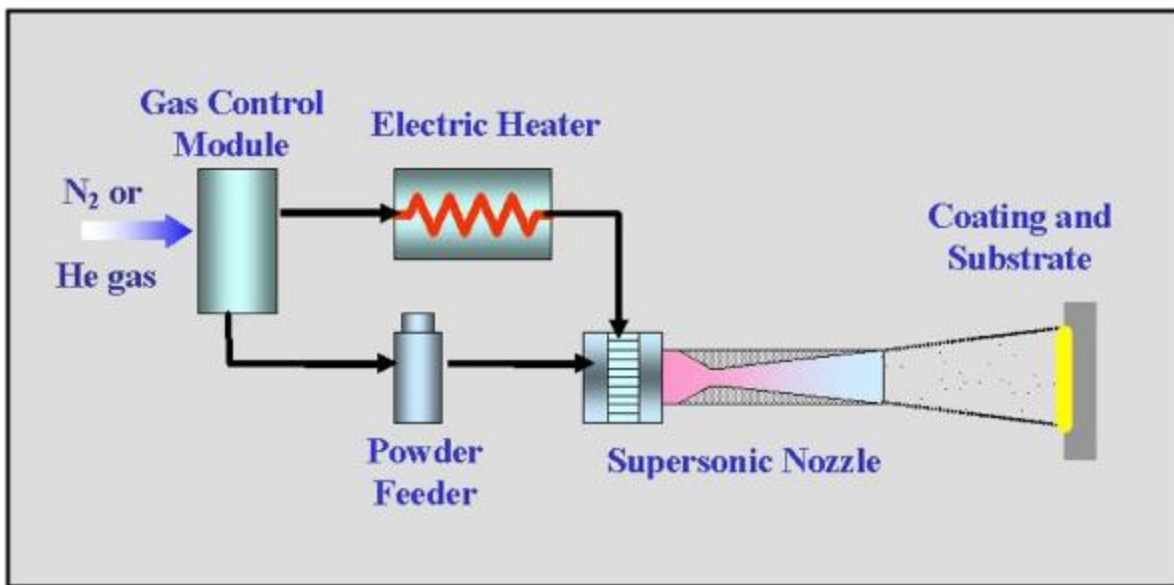


Figure 3: Simplified diagram of components in cold spray process (Champagne 2010). See appendix A1.1 for more complete diagram.

Each of these inputs can be changed in order to alter the process depending on the desired outcome. For example, the nozzle type can be solely convergent for lower speed impacts such as those used for polymer deposits (Champagne and Barnett 2012). Additionally, the supply gas is commonly changed between air, nitrogen, and helium depending upon the desired speed and

constraining costs. Particle size, shape, and material type can be changed in order to fit the desired application, but typical size ranges are reported in Figure 4 below.

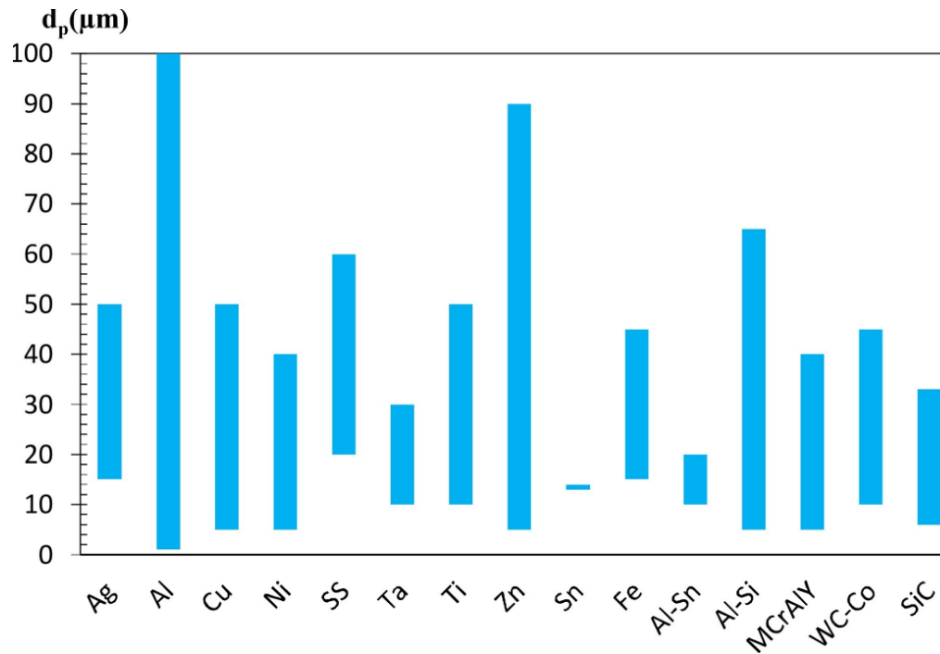


Figure 4: Typical powder diameters for different materials (Raelison et al. 2018)

#### 1.1.4 Mechanism of Cold Spray Bonding

The mechanism responsible for bonding in the cold spray of metals is still under debate. The impact phenomena differ at varying particle sizes and velocities as shown in Figure 5. At very low velocities ( $<100$  m/s), the particles may be collected on the surface due to van der Waals and electrostatic forces, but strong bonds are not formed. At faster speeds still below the critical velocity, the particles simply rebound from the substrate surface. Larger particles are more likely to rebound at these low speeds, but very large (1-10mm) particles may leave plastic prints on the surface after rebounding. So-called hypervelocity impacts turn particles to liquid upon impact and form severe shockwaves. At these speeds the damage done by smaller particles is less than by larger particles. Super deep penetration (defined as penetration distances  $10^3$ - $10^4$  times the particle diameter) is possible at velocities of 1000 – 3000 m/s (Klinkov 2005).

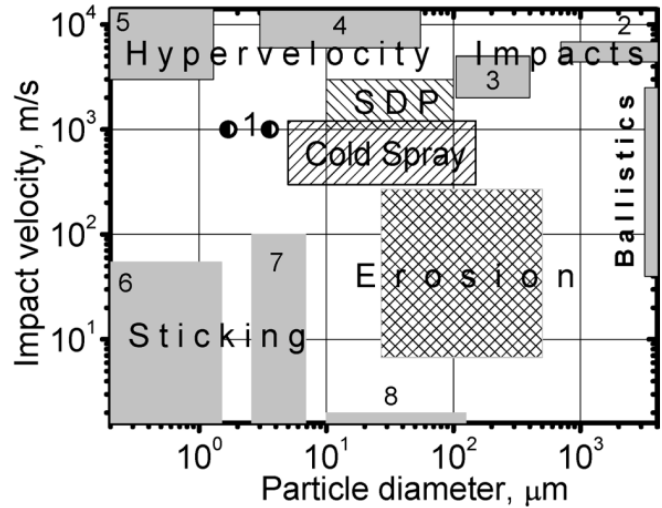


Figure 5: Particle impact response at different velocities (Klinkov 2005)

Experiments observe a critical velocity for bonding in which the kinetic energy of the particle is usually much lower than the energy which would be required to melt the particle. As a result, it is believed that the bonding is mostly or entirely solid-state (Grujicic 2004). The critical velocity for a perpendicular CS impact is primarily a function of the spray material, powder quality, particle size, and particle impact temperature (Schmidt 2006). Two primary theories for the bonding mechanism have emerged. One school of thought believes adiabatic shear instability is responsible (Assasi 2003, Grujicic 2004), while the other believes a hydrodynamic plasticity process is responsible and adiabatic shear instability is not necessary. In the latter theory, jetting removes oxides and surface asperities to enable metallic bonding (Hassani-Gangarai 2018, 2019). In the second theory, the bulk speed of sound in the material provides a strong correlation with the critical velocity.

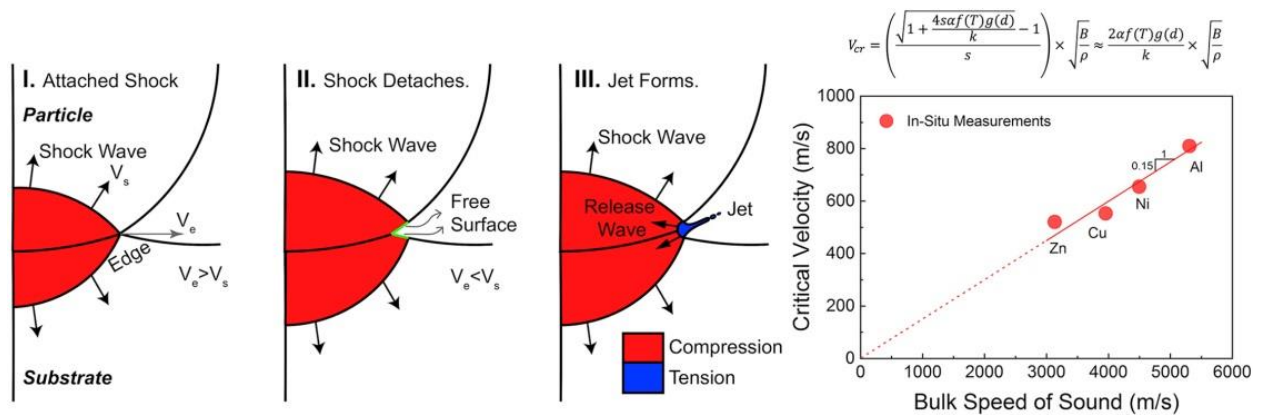


Figure 6: Proposed shock wave bonding mechanism (Hassani-Gangarai 2018)

## [1.2 Unresolved Issues](#)

There are many boundaries to be overcome before cold spray can be used to its full potential as a method for spraying structural materials. The cost of spraying with helium can be prohibitive for many applications, while spraying with other gases such as nitrogen often result in inferior mechanical properties. Many new materials continue to be sprayed through CS processes. However, development of the optimal spray parameters is still often a trial and error process. Better understanding of the bonding process and modeling of that process will allow for optimal spray parameters and mechanical properties to be predicted. More established cold spray materials such as aluminum and copper have tweaked process parameters to get better tensile properties, but fracture, fatigue, corrosion, and wear are just beginning to be studied (Moridi 2014). For repairs and additively manufactured parts to be used in structural situations, fracture and fatigue properties in CS must be understood. Likewise, for CS coatings to be trusted for long term service on critical components (Keech et al. 2014), wear and corrosion properties must be well understood.

## [1.3 Scope of Current Work](#)

- 1.3.1 Microstructure of Wrought and Powder 6061 Aluminum Alloy and Ti-6Al-4V
- 1.3.2 Indentation Size Effect and Strain Gradient Plasticity Length Scales for 6061 Aluminum Alloy, CP-Ti, and Ti-6Al-4V
- 1.3.3 FEA Simulation of Nanodentation and Resultant Pile-up
- 1.3.4 Stress-Strain Behavior of 6061 Aluminum Alloy and Ti-6Al-4V
- 1.3.5 FEA Simulation of Cold Spray Powder Impact With Oxide Layers and Bilinear Johnson-Cook Plasticity Model
- 1.3.6 Fatigue Crack Growth in Wrought 6061 Aluminum Alloy
- 1.3.7 Machine Learning of Hardness Images

## Chapter 2: Literature Survey

### 2.1 Microstructure and Physical Metallurgy of Aluminum Alloys

#### 2.1.1 Bulk 6061 Aluminum Alloy Metallurgy and Microstructure

6061 aluminum alloy is a wrought alloy comprised of face centered cubic (fcc) aluminum primarily alloyed with elements Cu, Fe, Mg, and Si. Different manufacturers' blends will have slightly different percentages of those alloying elements and typically contain small amounts of other elements such as Cr, Mn, Zn, and Ti (ASTM B209M-14).

Table 1: Composition of Wrought 6061 Aluminum Alloy Plate

Chemical Composition 6061 Aluminum Alloy Plate/Sheet ASTM Specification B209M - 14									Others (each 0.05)
Main Alloying Elements									
Al	Mg	Si	Fe	Cu	Cr	Mn	Zn	Ti	Total
Remainder	0.8-1.2	0.40-0.8	0.7	0.15-0.40	0.04-0.35	0.15	0.25	0.15	0.15

As with the rest of the 6000 series aluminum alloys, 6061 primarily uses  $Mg_2Si$  to provide precipitation strengthening. Some 6000 series aluminum dissolve nearly all the  $Mg_2Si$ , but 6061 often has supersaturated solution at the solutionizing temperature. 6061 aluminum alloy is age hardenable by controlling the size and number of precipitates. Iron, manganese, and chromium secondary phases ( $Fe_2Si_2Al_9$ ,  $(Fe, Mn, Cr)_3SiAl_{12}$ ) often form as inclusions in the material (Hatch, 1984).

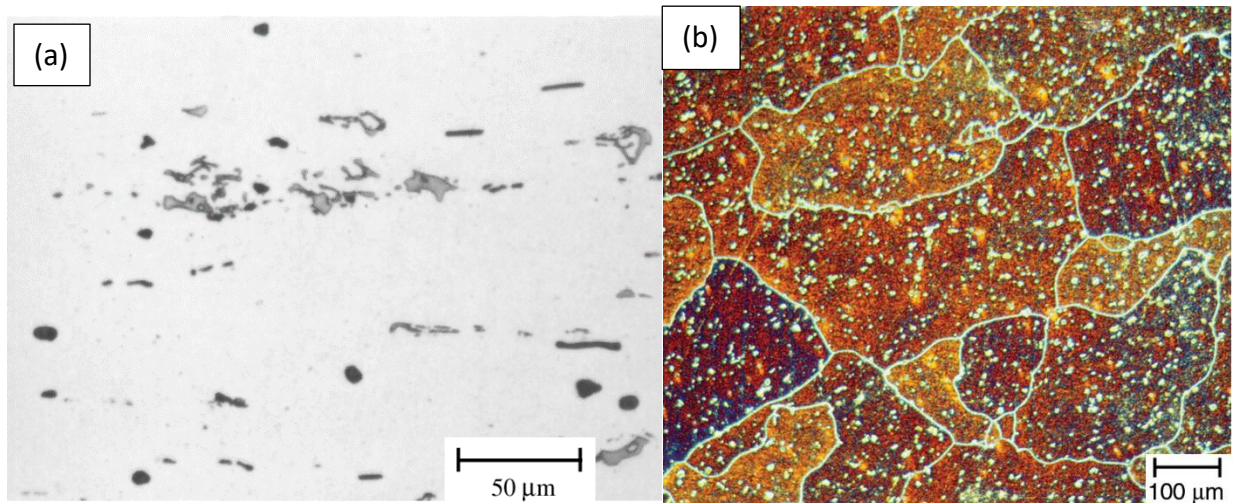


Figure 7: 6061-T6 sheet with insoluble  $(Fe,Cr)_3SiAl_{12}$  (lighter gray color) and excess soluble  $Mg_2Si$  particles (darker color). Etched with 0.5% hydrofluoric acid (a) (Lyman 1972). 6061- T651 Aluminum etched with Weck's reagent showing grain diameters of a few hundred  $\mu m$  (b) (Vander Voort 2004)

Grain sizes in aluminum alloys are heavily dependent upon the processing techniques and heat treatment. Different cross-sections of material which has been stressed can cause order of magnitude differences in grain size (Nakai and Itoh, 2014). Some specially processed aluminum alloys have grain diameters which are hundreds of nanometers (Lee et al. 2002), but most range from a few micrometers to hundreds of micrometers as seen in Figure 7b (Easton and St. John, 2008). 6061-O alloy undergoes an annealing heat treatment process at 415 °C for 2-3 hours to reduce stress concentration and reduce precipitation strengthening so that the alloy is weaker but more ductile (ASM Volume 4, 1991). Contrarily, 6061-T6 is precipitation strengthened to its maximum point.

### 2.1.1.2 6061 Aluminum Alloy Powder Microstructure

Aluminum alloy powders for use in cold spray are frequently produced by a gas atomization process, which can produce spherical powders with chemical compositions similar to the bulk alloys. For 6061 gas atomized powders, the particle size typically varies from less than 5 μm to around 80 μm, but average diameters for a given feedstock are typically around 25-40 μm (Rokni et al. 2013, Bedard et al. 2018, Gavras et al. 2018).

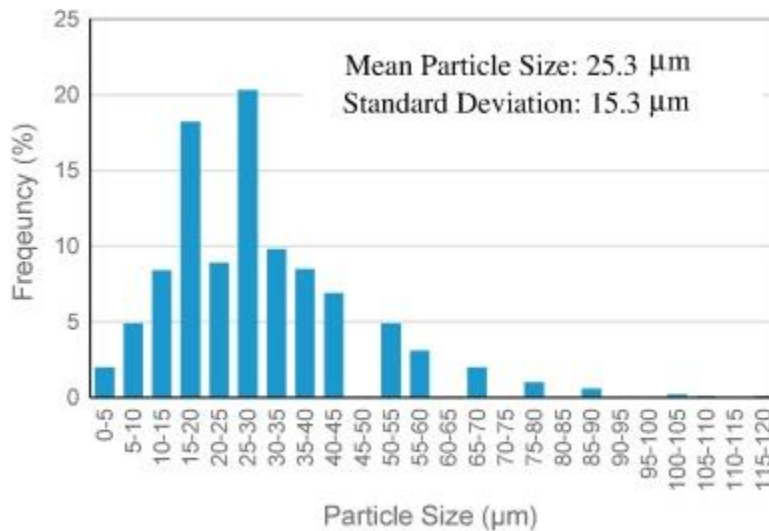


Figure 8: 6061 Aluminum alloy powder particle size distribution (Gavras et al. 2018)

Different powder size distributions can be produced by sifting the powders or by altering the gas atomization process parameters if desired. Though the chemical composition of 6061 powders is similar to that of wrought 6061, the microstructure has significant differences.

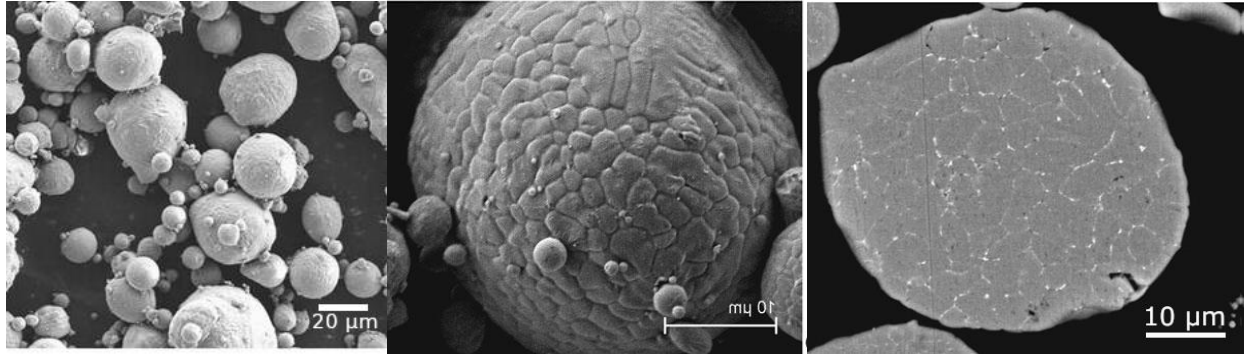


Figure 9: 6061 Aluminum alloy powder morphology and microstructure (Rokni et al. 2013)

Rokni et al. (2013) found the powder subgrains were primarily equiaxed but contained high dislocation densities as a result of residual stresses from rapid cooling. Grain boundaries were typically low angle and also have a higher concentration of Mg, Si, and Fe (Bedard et al. 2018).

### 2.1.3 Bulk Cold Sprayed 6061 Aluminum Alloy Microstructure

As the particles undergo significant plastic deformation upon impact, splat diameters generally increase from the diameter of the original particle. The boundaries between splats can be clearly identified after etching and deposition porosities have been found around 2% by area for pure aluminum (Rech et al. 2010). Since critical velocity and quality are significantly affected by oxides present in the particles (Champagne 2018, Hassani-Gangarai 2019), it is possible that proper powder handling can further reduce this porosity.

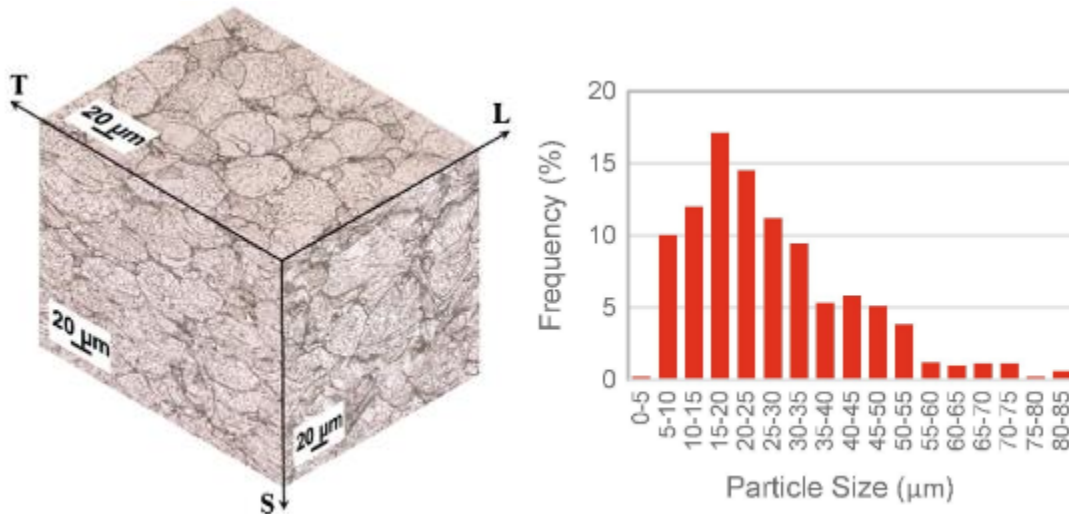
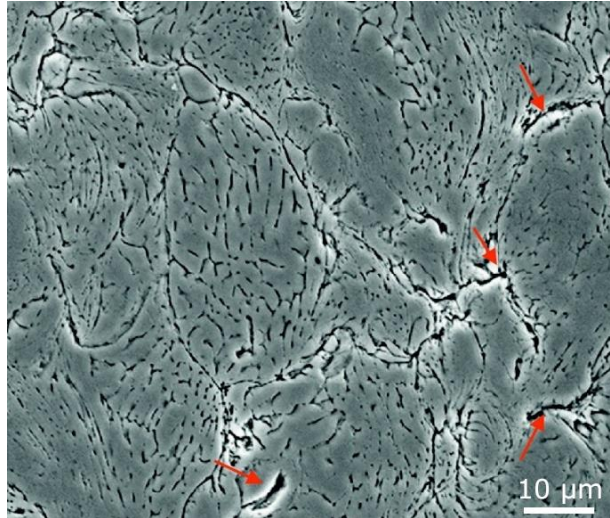
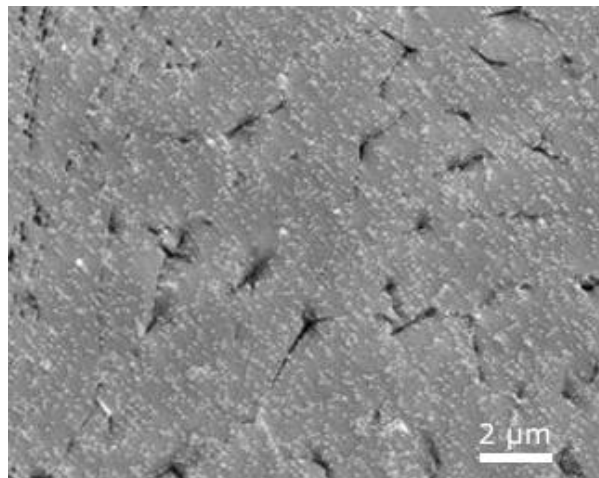


Figure 10: Cross section of sprayed 6061 plate and size distribution of the particle splats (Gavras et al. 2018)



*Figure 11: Cross section of cold sprayed 6061 aluminum alloy deposit with red arrows highlighting voids and porosity between particles (Rokni et al. 2017)*

A bimodal microstructure and grain size distribution has been reported due to the deformation of the particles. Grain diameters in the center of the cold spray sprayed were 1- 10 μm, similar to that in the powder before spraying. However, the boundaries of the particle splats contained pancaked and ultrafine grains down to around 100 nm (Rokni et al. 2013, 2014, and 2017). Lower pressure sprays had expectedly less particle deformation and weaker bonding (Bedard et al. 2018). If the deposition was inspected before any post-heat-treatment, a high level of stress, dislocations, and crystal lattice distortions were reported, while annealing and T6 heat treatments reduced dislocations, grew larger precipitates, and increased grain size (Rokni et al. 2014). Lamellar grains in the y directions were found be high angle, while the grains in the z direction were found be a mix of high and low angles (Rokni et al. 2013). Finally, nanoscale precipitates have been detected within the 6061 cold spray deposit.



*Figure 12: Nanoscale precipitates in cold spray deposit (Rokni et al. 2013)*

#### 2.1.4 Bulk Cold Sprayed 6061 Aluminum Alloy Mechanical Properties

The results have shown that CS deposits of 6061 powder with helium feedstock gas have tensile strengths comparable or exceeding that of wrought 6061, while the percent elongation is typically only a few percent in comparison with the 10-25% typically seen in wrought 6061 (Champagne and Helfritch, 2014, Rokni et al. 2017). Other researchers have found approximately 10% reductions of yield strength and tensile strength for CS 6061 compared with wrought 6061 (Gavras et al. 2018). Work by Rokni et al. (2018) found that tensile properties within a 5056 CS deposit have significant differences depending upon the direction. The best properties were found in the direction or the path of the spray nozzle, while the worst were in the layer direction (z). Micro-pillar compression tests found the yield and ultimate tensile strengths of the sprayed deposit to be approximately double those in the powder (Bedard 2018). Fractography conducted on tensile samples 6061 CS deposits found a combination of ductile void coalescence and smooth particle-particle separation (Rokni 2017).

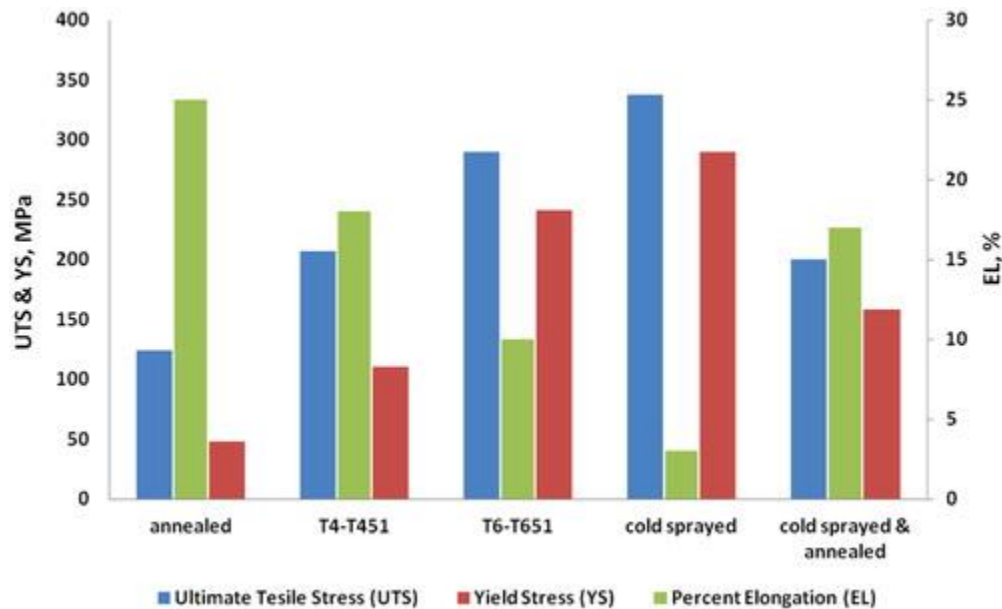


Figure 13: Tensile properties of wrought and cold-sprayed 6061 aluminum alloy (Champagne and Helfritch, 2014)

Nanohardness testing has revealed that particle interfaces are harder than particle interiors (1.8 GPa vs 1.4 GPa), but both are harder than the powder before spraying (1.0 GPa) (Rokni et al. 2017). Other researchers have found the hardness and elastic modulus of the CS deposit to be similar to that of the wrought material.

Table 2: Comparison of 6061 aluminum alloy CS deposit mechanical properties with that of wrought 6061 (Gavras et al. 2018)

Alloy	Microhardness	$\sigma_{Y(0.2\%)}$	$\sigma_{UTS}$	Elongation	$E$
	[HV <sub>100</sub> ]	(MPa)	(MPa)	(el%)	(GPa)
Cold-spray 6061 – As-sprayed	105.0	262.0	286.8	2.0	67.5
Cold-spray 6061 – Annealed	65.7	147.5	195.1	13.0	64.1
Cold-spray 6061 – T6	120.0	203.4	216.5	1.8	65.1
Rolled 6061-T6	107.0	291.6	317.1	17.0	70.3

## 2.2 Microstructure and Physical Metallurgy of Titanium Alloys

### 2.2.1 Commercially Pure Titanium Metallurgy and Microstructure

Titanium at room temperature exists in a hexagonal close packed (hcp) crystal structure called  $\alpha$  phase. At temperatures of 888°C and above, the hcp crystal structure of titanium converts into a body centered cubic (bcc) crystal structure called  $\beta$  phase (Donachie 2002). Commercially pure titanium is considered an  $\alpha$  phase titanium alloy at room temperature as it contains little  $\beta$  stabilizing elements (Wanhill and Barter 2012).

Table 3: Composition of grade 2 commercially pure titanium

Chemical Composition Grade 2 CP Titanium (R50400)- ASTM Specification B265 - 15						
Main Alloying Elements						Others (each 0.1)
Ti	C (max)	O (max)	N (max)	H (max)	Fe (max)	Total
Remainder	0.08	0.25	0.03	0.015	0.30	0.4

Oxygen content controls the tensile properties of CP titanium to a large extent, with larger concentrations increasing the tensile strength. Iron serves as a beta stabilizer (Donachie, 2002). Grain size can vary depending upon the processing condition and the microstructure is sensitive to external factors such as hydrogen or stress as seen in the comparison in Figure 14. Hydride needles can often form through hydrogen absorption, producing a very different structure shown in Figure 15 below.

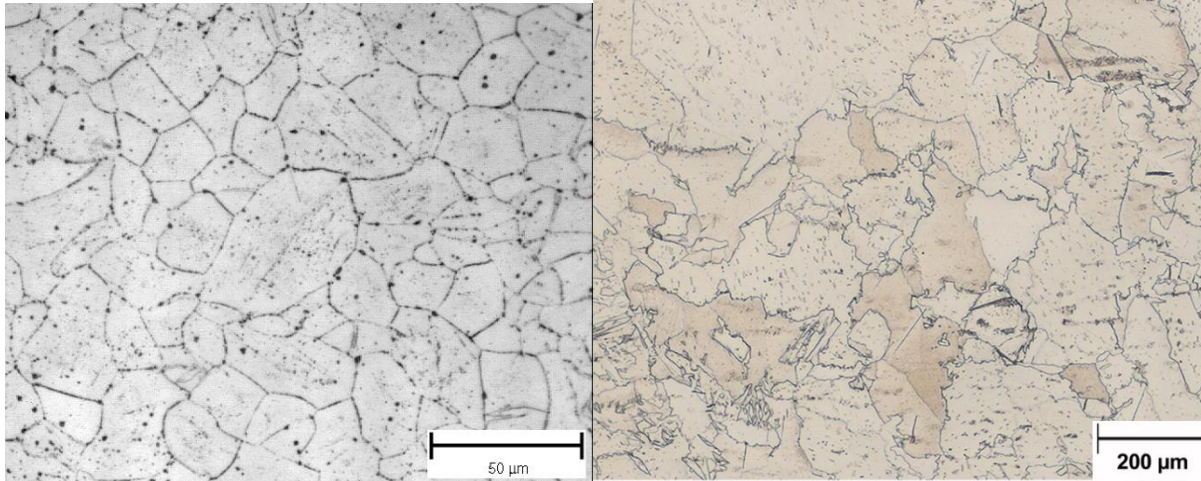


Figure 14: Varying grain structure of CP titanium etched with Kroll's reagent showing lighter colored alpha grains and dark spots of iron-stabilized beta phase (ASM Micrograph Database ti0100 and ti0308)

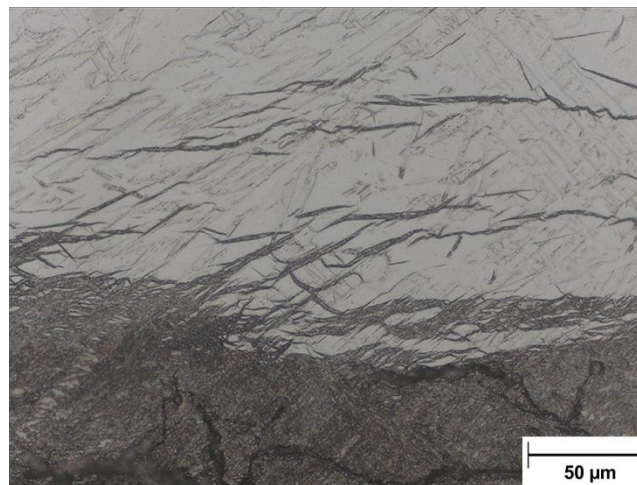


Figure 15: Hydride needles formed in CP titanium (ASM Micrograph Database ti0310)

### 2.2.2 Bulk Ti-6Al-4V Metallurgy

Ti-6Al-4V (also shortened as Ti64) is a common  $\alpha$ - $\beta$  titanium alloy in which vanadium serves as a  $\beta$  phase stabilizer, while aluminum stabilizes  $\alpha$  phase. Other elements are available in small percentages which are almost impossible to eliminate, but can be reduced. The Ti64 with reduced levels of other interstitial elements is called ELI (extra low interstitial).

Table 4: Composition of Ti-6Al-4V-ELI

Chemical Composition Grade 5 Ti-6Al-4V (R56400)- ASTM Specification B265 - 15								
Main Alloying Elements								Others (each 0.1)
Ti	C (max)	O (max)	N (max)	H (max)	Fe (max)	Al	V	Total
Remainder	0.08	0.20	0.05	0.015	0.40	5.5-6.75	3.5-4.5	0.4

$\alpha$  phase can be separated into primary and transformation  $\alpha$  in which  $\beta$  phase has transformed into co-oriented  $\alpha$  lamellae (Wanhill and Barter 2012).

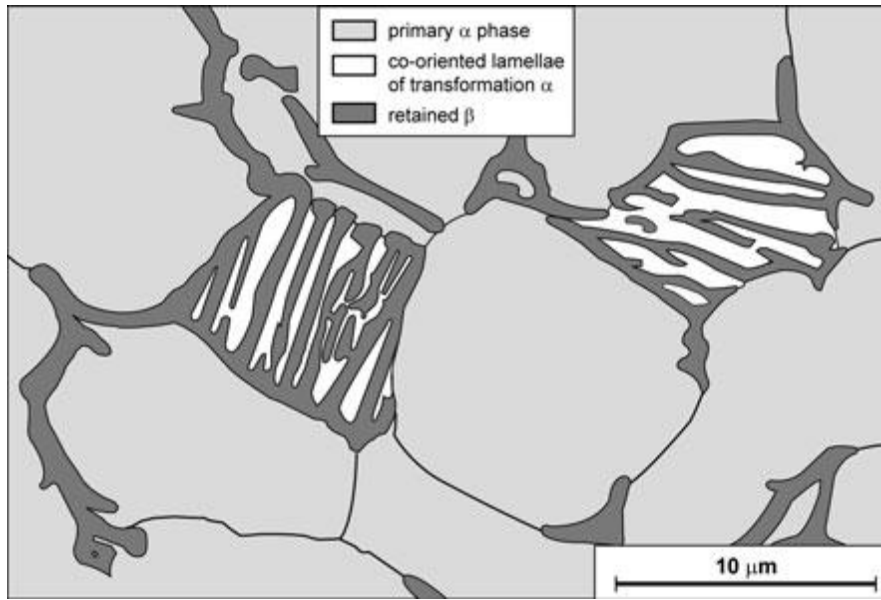


Figure 16: Diagram showing primary  $\alpha$ , transformation  $\alpha$ , and retained  $\beta$  (Wanhill and Barter 2012)

A  $\beta$  annealing heat treatment process is often used to improve properties for fatigue crack growth, fracture toughness and stress corrosion cracking at the expense of tensile strength.

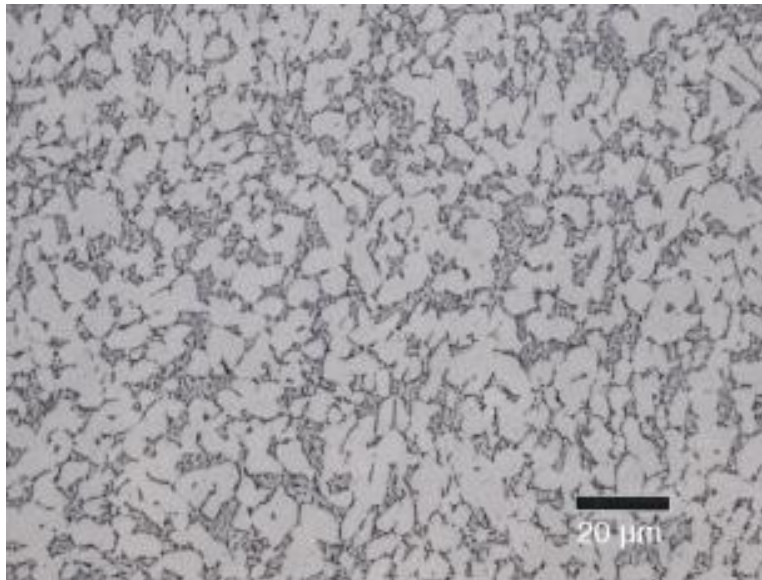


Figure 17: Annealed Ti-6Al-4V ELI (R56401) showing primary alpha grains and alpha-beta matrix structure (ASM Microstructure Database ti0230)

Rapid cooling may form a Widmanstatten pattern (with acicular alpha) from decomposed  $\beta$ , while slower cooling and annealing tend to produce less needle-like structures and more equiaxed or elongated grains with stable  $\beta$  around grain boundaries (Donachie 2002).

### 2.3.3 Ti-6Al-4V Powder Metallurgy and Microstructure

Similar to many 6061 powders, Ti64 powders are often produced by an atomization process which results in a spherical shape such as that seen in Figure 18. The composition of the atomized powders is typically close to bulk Ti64 ELI.

Table 5: Composition of Ti-6Al-4V Powder (Birt et al. 2015)

Chemical Composition Grade 5 Ti-6Al-4V Powder											
Main Alloying Elements											Others
Ti	Al	V	Fe	O	Si	N	H	C	Cu	Sn	Total
Rem.	6.39	4.1	0.2	0.126	0.017	0.015	0.0095	0.009	0.0031	<0.002	< 0.3

The powders can also be produced by a hydride-dehydride process which produces angular and non-uniform shapes seen in Figure 20 (Bhattiprolu et al. 2018) or the Armstrong process which produces porous irregular shapes shown in Figure 19 (Munagala et al. 2018). The powder size typically ranges from 0-45  $\mu\text{m}$ , but can be larger as well (Birt et al. 2015, Bhattiprolu et al. 2018, Vo et al. 2013). The spherical powders typically have a martensitic lath structure due to the rapid cooling in the fabrication process (Vo et al. 2013). The exterior of the powders often have a cellular structure from rapid nucleation and solidification. Smaller diameter powders may

have a mix of equiaxed and acicular grains or homogenous features with a smooth outer surface.

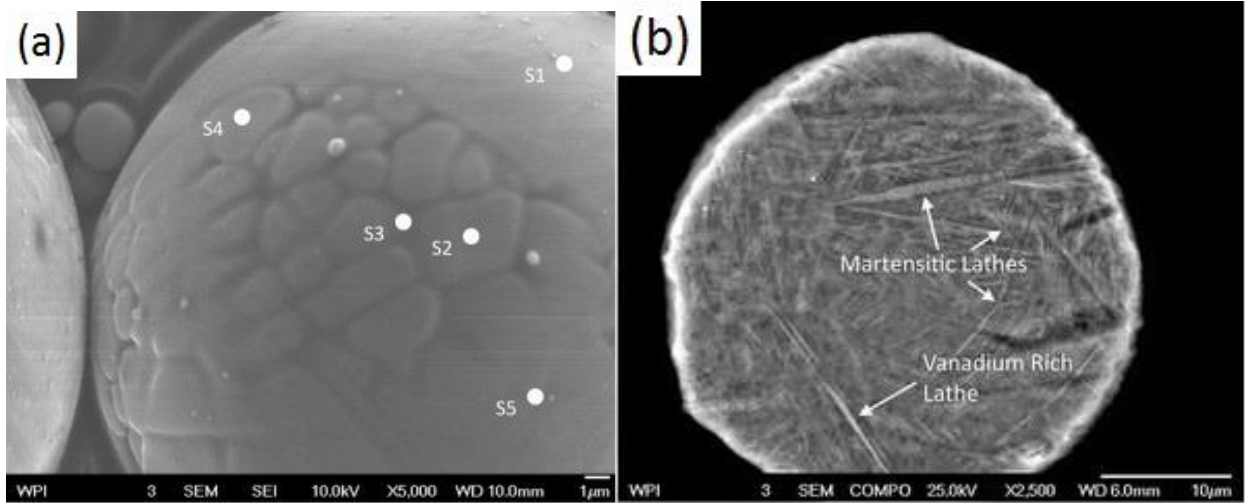


Figure 18: Exterior cellular structure (a) and interior lath structures (b) in Ti-6Al-4V (Birt et al. 2015)

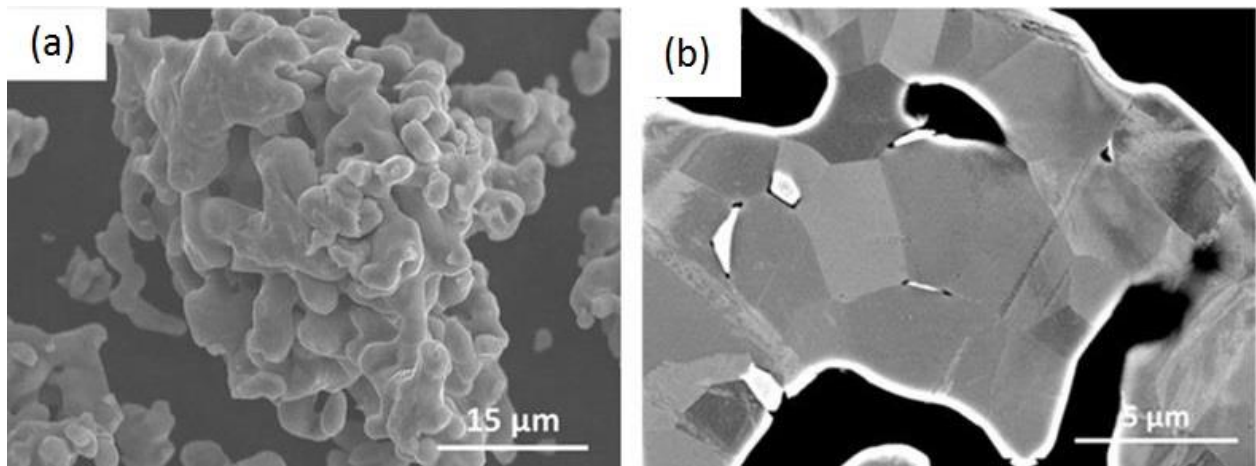


Figure 19: Particles produced by the Armstrong process showing porosity and non-uniform topography (a) and equiaxed alpha microstructure (b) (Munagala et al. 2018).

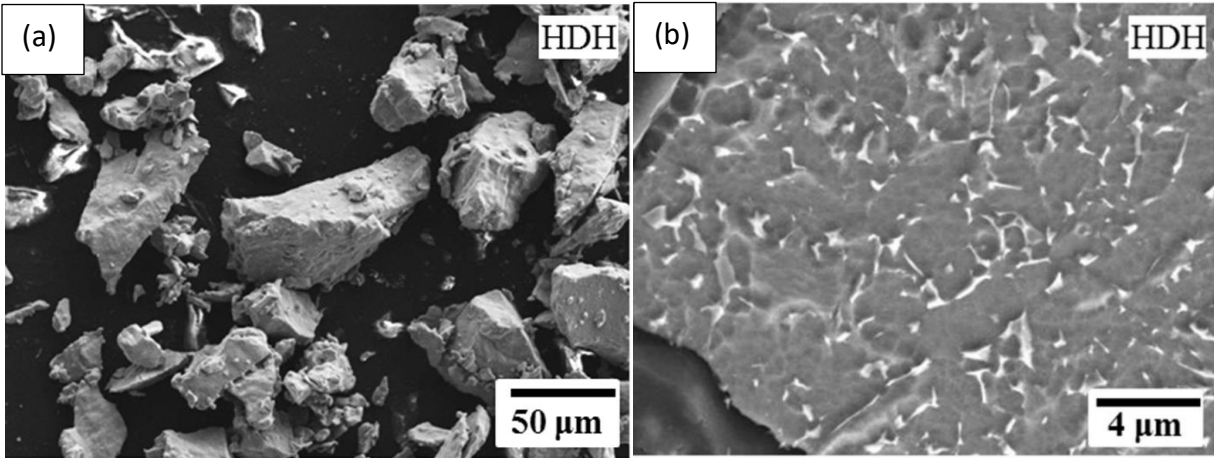


Figure 20: Particles produced by the hydride-dehydride process with angular morphology (a) and equiaxed alpha grain structure with intergranular beta (b) (Bhattiprolu et al. 2018)

Nanohardness values ranged from 1.8 GPa to 3 GPa with the highest hardness found in the martensitic structures of the larger particles. (Birt et al. 2015). On the other hand Bhattiprolu et al. found nanohardness values ranging from 3.7 GPa to 4.5 GPa for their gas atomized, plasma atomized, and crushed powders.

#### 2.3.4 Bulk Cold Sprayed Ti-6Al-4V Microstructure

The particle layup process for Ti64 is very similar to that of aluminum alloys. However, higher velocities are required for quality depositions. Birt et al. (2015) found porosities of around 11% for their plasma atomized powders sprayed with nitrogen and 2% for deposits sprayed with helium. Other researchers found porosities under 3% for spherical and angular powders sprayed with helium, while under 1% for the Armstrong process powders (Bhattiprolu et al. 2018, Munagala et al. 2018, and Vo et al. 2013). Much less particle deformation and jetting was seen in the porous materials sprayed by nitrogen in comparison with that sprayed by helium (Birt et al. 2015, Vo et al. 2013).

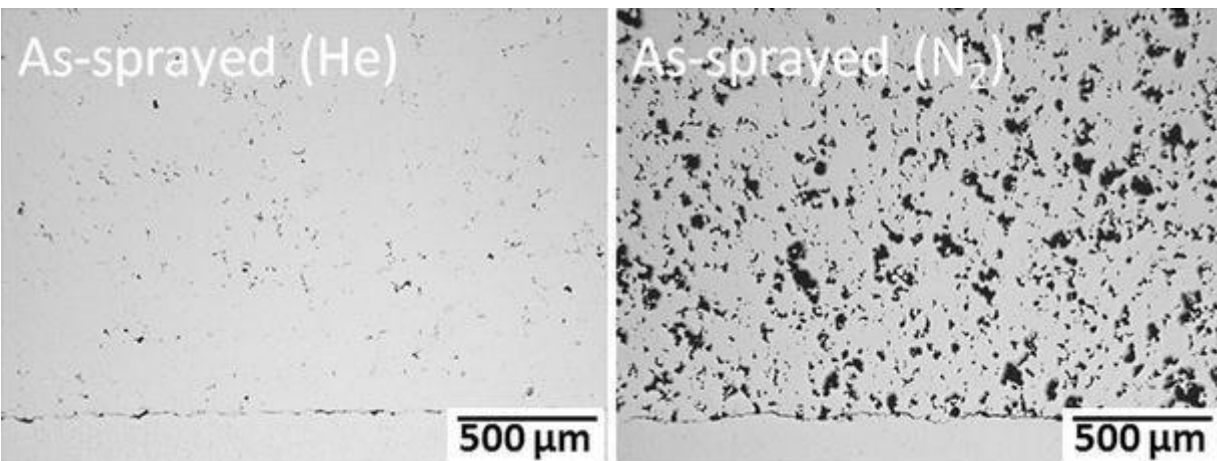


Figure 21: Ti-6Al-4V deposits with 0.3% porosity and 8.1% porosity sprayed with helium and nitrogen gas respectively (Vo et al. 2013)

Microcracks were found to have formed near particle-particle interfaces (Bhattiprolu et al. 2018). The Ti64 CS deposits largely retained the original microstructures of the powder. Equiaxed powders produced equiaxed and elongated grain structures in the CS deposit, while acicular powders produced broken martensitic structures (Birt et al. 2015) and acicular  $\alpha$  in the cold spray deposit (Vo et al. 2013, Bhattiprolu et al. 2018).

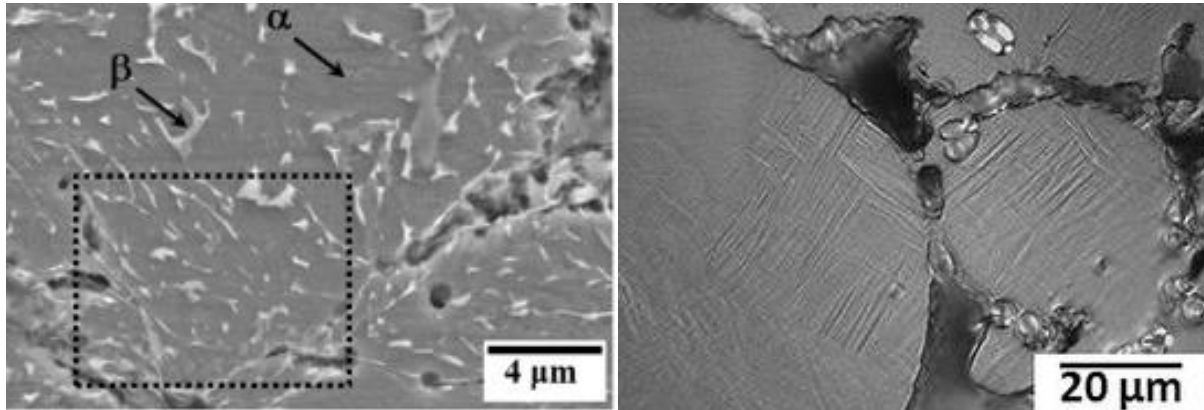


Figure 22: Ti-6Al-4V deposits showing equiaxed/elongated grains (Bhattiprolu et al. 2018) and acicular  $\alpha$  structures (Vo et al. 2013)

### 2.3.5 Bulk Cold Sprayed Ti-6Al-4V Mechanical Properties

More work needs to be done on the bulk mechanical properties of CS Ti64. Some work has been done testing the adhesion of the Ti64 as a coating using glue bond tests (Tan et al. 2017, Bhattiprolu et al. 2018) or bend tests. The glue often failed between the CS bond, making the true strength unknown. Tan et al. (2018) also did a couple tensile samples of a CS T64 coating on Ti64 substrate and found a bond strength of 90 MPa. Vo et al. (2017) on the other hand found ultimate tensile strengths around 450 MPa and 4% elongation which would be improved with post-process heat treatment. The fracture surfaces from the tensile tests were mixed of ductile dimples and smooth brittle failure between particles.

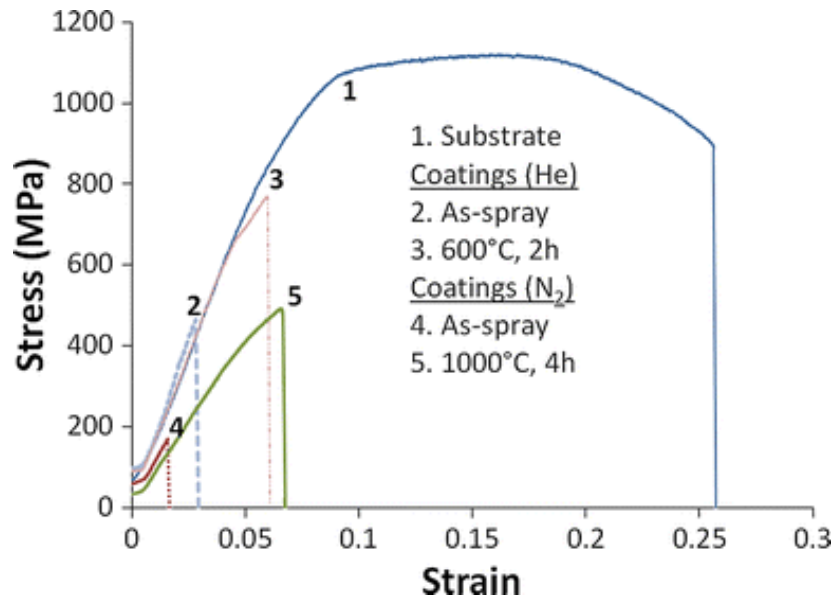


Figure 23: Typical stress-strain curves for Ti-6Al-4V substrate, helium and nitrogen sprayed coatings and coatings after heat treatment (Vo et al. 2017)

Nano and microhardness measurements were taken by several researchers so far, but the results have been, to the opinion of this author, rather inconclusive. Bhattiprolu et al. (2018) found that the hardness varied depending on powder manufacture, spray temperature, and nozzle length. Vickers microhardness value averages ranged from around 350 HV to 425 HV with standard deviations around  $\pm 25$  HV making it difficult to draw conclusions.

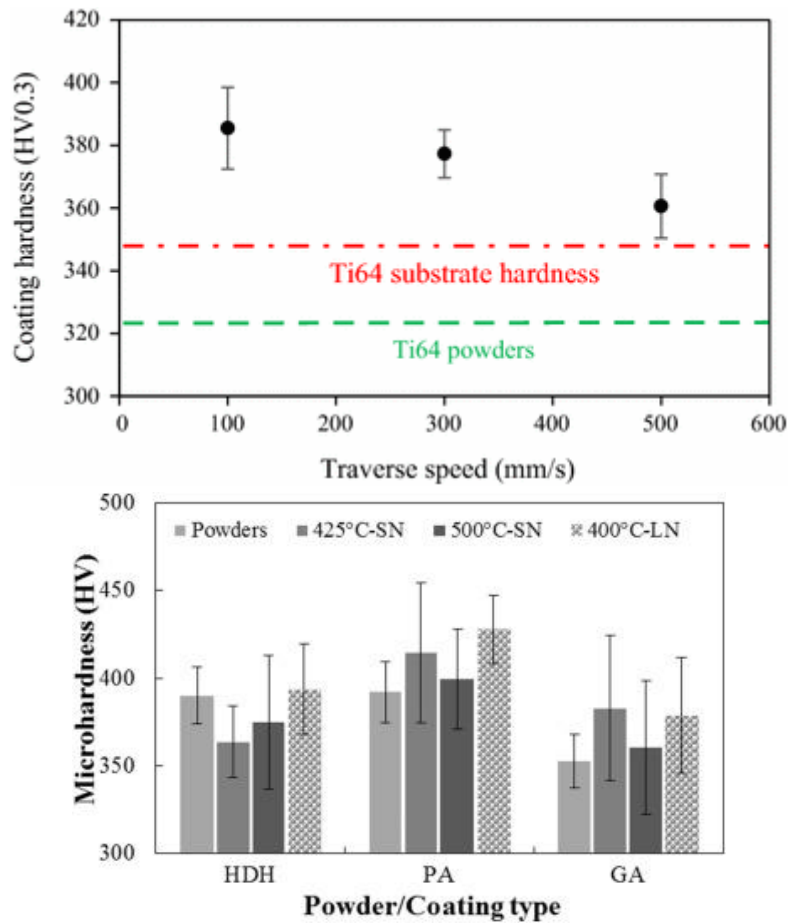


Figure 24: Vickers microhardness measurements on Ti-6Al-4V cold spray coatings (Tan et al. 2017) and (Bhattiprolu et al. 2018)

Similarly, Munagala et al. (2018) found significant scatter in microhardness results and reported interparticular slipping/debonding during the indentation, which accounted for lower hardness values when compared to bulk Ti64 plate.

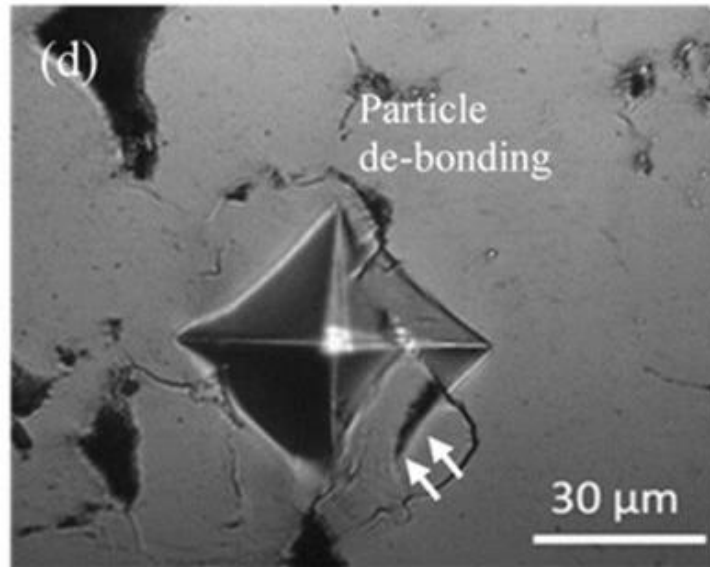


Figure 25: Particle debonding during microindentation (Munagala et al. 2018)

Nanohardness averages on etched (not indicative of the true surface) samples were found to be 2.1 GPa for nitrogen sprayed samples and 5.1 GPa for helium sprayed samples (Birt et al. 2015).

### [2.3 The Indentation Size Effect](#)

#### [2.3.1 Statistically Stored Dislocations](#)

Metals are thought to contain statistically stored dislocations (SSD) which are created by homogeneous strain and are dependent upon the material and processing conditions (Nix and Gao 1998). These dislocations increase material hardness by increasing flow stress through dislocation blocking mechanisms (Askeland and Wendelin 2016).

#### [2.3.2 Geometrically Necessary Dislocations](#)

It has been widely observed in literature that there is a so-called “indentation size effect” (ISE) in which smaller indentation sizes result in higher measured hardness’s (Pharr et al. 2010). This effect is believed to be a result of geometrically necessary dislocations (GND) being added to the effect of statistically stored dislocations. Geometrically necessary dislocations are thought to be a result of additional nucleated dislocations required to accommodate the permanent shape change as seen in Figure 26 below.

W. D. NIX and H. GAO  
**Geometrically Necessary Dislocations**

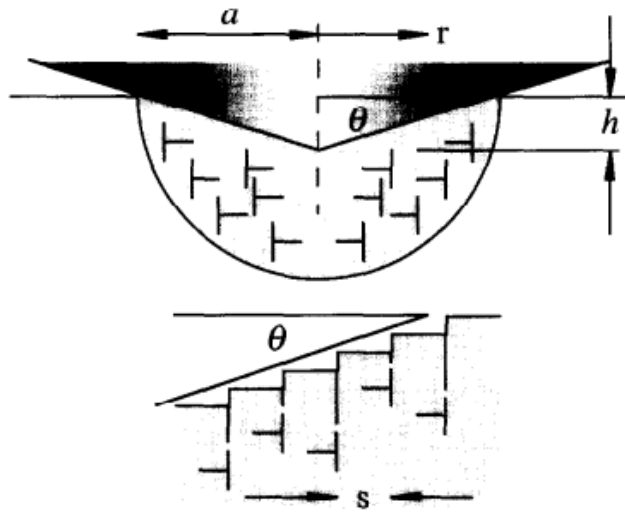


Figure 26: Schematic representing theory of geometrically necessary dislocations (Nix and Gao, 1998)

The impact of geometrically necessary dislocations can be seen in Figure 27 which shows the hardness as a function of depth. As the depth increases the impact of GNDs is less pronounced and the hardness values decrease along a logarithmic curve.

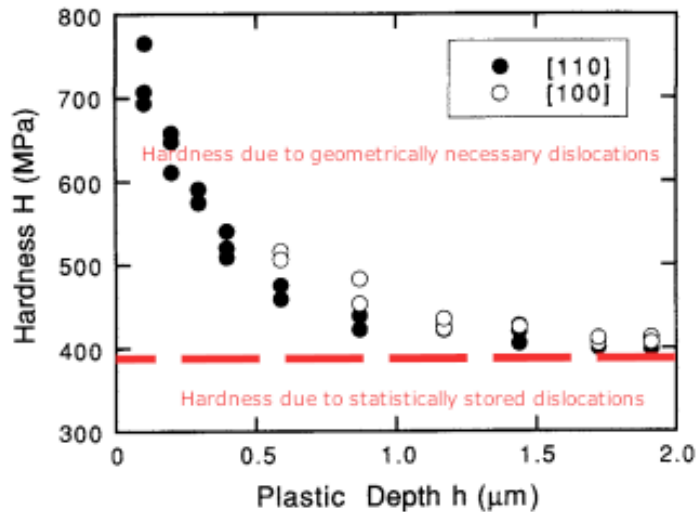


Figure 27: Hardness as a function of plastic depth for silver single crystals (Ma and Clarke, 1995)<sup>1</sup>

### 2.3.3 Experimental Determination of Hardness

As the statistically stored dislocations are not typically dependent on the depth of the material (though the method of manufacture can affect this), we would like to have a measurement of

<sup>1</sup> Red parts of image are modifications made by myself to the original figure

the hardness considering only SSDs to make comparisons between experiments easier. This can be seen if there is a plateau in the hardness data at a certain depth, as we are starting to see in Figure 27 above. Additionally, we can find the hardness based on SSDs,  $H_0$ , using the relationship determined by Nix and Gao (1998).

$$\frac{H}{H_0} = \sqrt{1 + \frac{h^*}{h}} \quad (1)$$

The above equation models a linear relationship where  $H$  is the measured hardness,  $h^*$  characterizes the depth dependence of the hardness, and  $h$  is the indentation depth. In Figure 28 seen below, the slope of the line of best fit corresponds to  $h^*$ .  $H_0$  is determined by finding the intercept point of the line of best fit for a plot of the hardness squared to the inverse of the indentation depth.

Nix and Gao also derive a method to calculate the characteristic length,  $h^*$ , based upon the shear modulus,  $\mu$ , and burgers vector,  $b$ , for the material.  $\alpha$  is a material constant typically around 0.5 while  $\vartheta$  is the angle between the indenter tip surface and the surface of the substrate.

$$h^* = \frac{81}{2} b \alpha^2 \tan^2 \theta \left( \frac{\mu}{H_0} \right)^2 \quad (2)$$

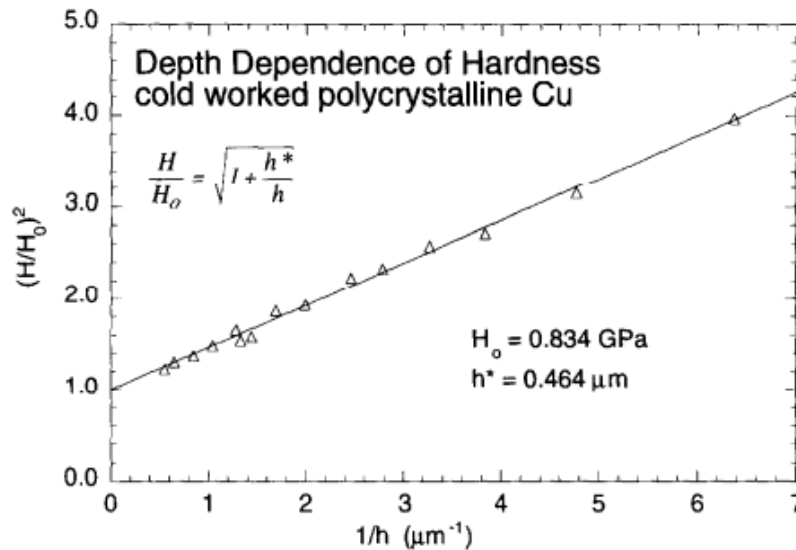


Figure 28: Linearized relationship between hardness and depth. The slope of the line is  $h^*$  while the y intercept is  $H_0$ . Experimentally finding the hardness based upon statistically stored dislocations (Nix and Gao, 1998)

#### 2.3.4 Discrete Dislocations

Work by Zong (2005) suggests three separate size scales of importance for indentation. According to her work, indentation sizes above  $10\ \mu\text{m}$  can be represented with conventional plasticity theory. Sizes between approximately  $100\ \text{nm}$  and  $10\ \mu\text{m}$  should be represented with strain gradient plasticity theory, while sizes below  $100\ \text{nm}$  should be simulated using discrete dislocation theory.

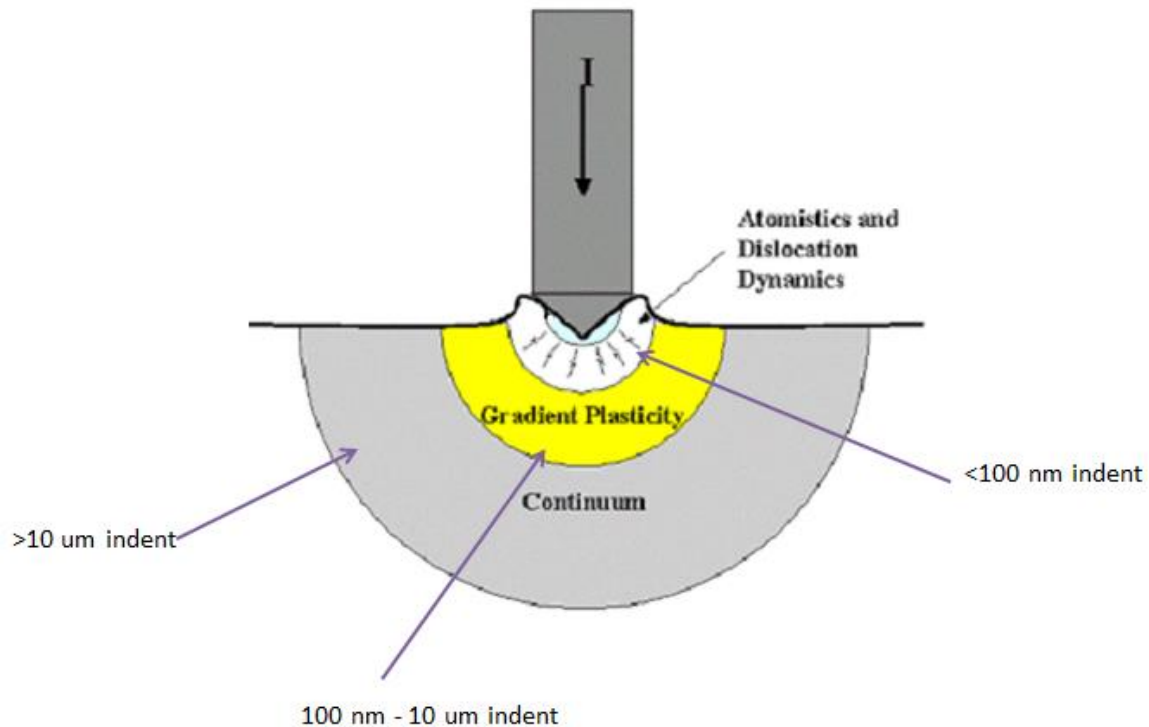


Figure 29: Dislocation mechanics scales (Zong et al. ASME)

Indentations on the nanoscale are able to impress on the surface in between dislocations as modeled in Figure 30. This requires dislocations to be nucleated resulting in a higher required load and therefore a higher measured hardness.

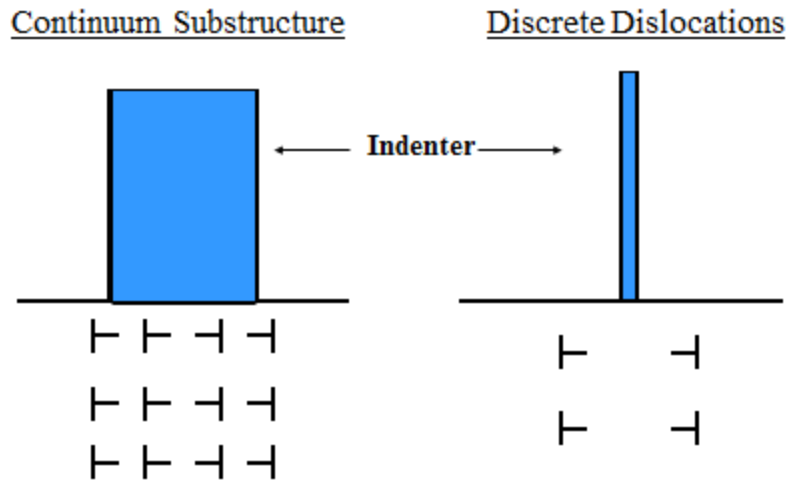


Figure 30: Diagram representing discrete dislocation theory (Zong et al. ASME)

### 2.3.5 Material Length Scale

The material length scale ( $l$ ) is defined by Nix and Gao as the length at which a strain gradient must be compared in order to effect the strain gradient on the flow stress. By using the Von Mises flow rule and Tabors correction, the length scale can be given by the relationship between the Burgers vector,  $b$ , flow stress in the absence of a gradient,  $\sigma_0$ , and the shear modulus for the material,  $\mu$ .

$$l = b \left( \frac{\mu}{\sigma_0} \right)^2 \quad (3)$$

This length can be approximately related to the mean spacing between statistically stored dislocations or the density of statistically stored dislocations using equation 4 below;

$$l = \frac{4 L_s^2}{3 b} = \frac{4}{3 b \rho_s} \quad (4)$$

where  $L_s$  is the mean spacing between statistically stored dislocations,  $b$  is the Burgers vector, and  $\rho_s$  is the density of statistically stored dislocations. This is useful as it is a property of the material and homogeneous strain in that material. Nix and Gao (1998) calculated the length scale for annealed Copper to be 12.0  $\mu\text{m}$  and cold worked Copper to be 5.84  $\mu\text{m}$ . These values clearly show the impact that strain (and hence excess dislocations) in the material will have on the length scale.

The material length scale can be predicted experimentally from hardness data by first solving for the density of statistically stored dislocations using the material shear modulus, burgers vector magnitude, and  $H_o$ .

$$H_0 = 3\sqrt{3}\alpha\mu b\sqrt{p_s} \quad (5)$$

$$\rho_s = \left( \frac{H_0}{3\sqrt{3}\alpha\mu b} \right)^2 \quad (6)$$

### 2.3.6 Nanoindentation Methods

Measurements of nanohardness can be achieved using a variety of indenter tips such as Berkovich, cube corner, spherical, and conical. All tip types can return hardness as a pressure given by the load on the tip and the projected area of that load, also known as Meyer's hardness.

$$H = \frac{\text{Force}}{\text{Projected Area}} \quad (7)$$

The indentation machine will produce data containing the indentation depth versus applied load. The area is calculated based of a function for the tip shape and the depth of the indentation. The reduced modulus,  $E_r$ , for the material can also be found by taking the slope of the load versus displacement curve upon unloading the indent. The elastic modulus,  $E$ , for the sample can be found by using the Poisson's ratios of the sample and indenter as well as the modulus for the indenter (Oliver and Pharr 2004).

$$\frac{1}{E_r} = \left( \frac{1 - \nu^2}{E} \right)_{\text{sample}} + \left( \frac{1 - \nu^2}{E} \right)_{\text{indenter}} \quad (8)$$

### 2.3.7 Microhardness Methods

Microindentation functions in a similar way to nanoindentation, the size scale is simply different. Again, many different types of tips can be used, but the Vickers tip is popular for metallic materials and has a similar area function to the Berkovich tip (4 sided pyramid versus 3 sided pyramid). Different mechanisms of measuring and recording loads and areas can be used, but optical measurement will be discussed here as that is used in the experimental portion of this paper. The desired load is set on the machine before indenting. After indentation a pyramid-shaped imprint is left in the surface. The user then optically takes measurements from corner to corner of the imprint to find  $d_1$  and  $d_2$  lengths shown in Figure 31 below.

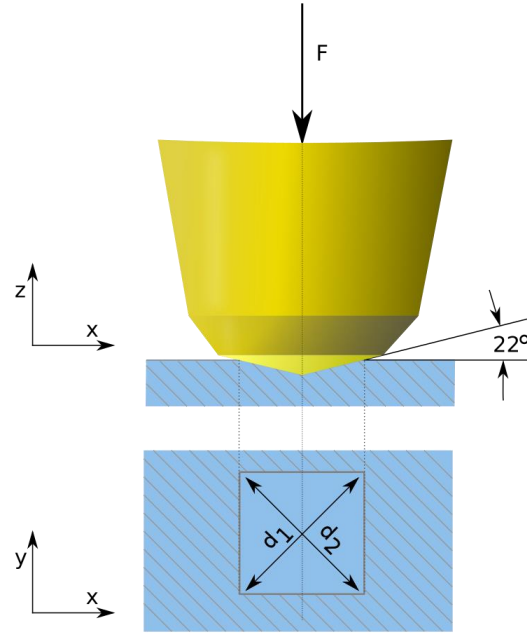


Figure 31: Diagram of Vickers indentation (User A1, 2018)

The average of  $d_1$  and  $d_2$ ,  $d_v$ , is used to find the surface area of the indentation,  $A_s$ , by dividing the square of the diagonals by a geometrically determined constant.

$$A_s = \frac{d_v^2}{1.8544} \quad (9)$$

Vickers Hardness (HV) is found by dividing loading force by indentation surface area in units of  $\text{kgf}/\text{mm}^2$  or  $\text{gf}/\mu\text{m}^2$  (ASTM E92-17, 2017).

$$HV = 1854.4 \frac{F_{(gf)}}{d_v^2(\mu\text{m})} \quad (10)$$

The Vickers hardness can be directly converted to SI units based on the surface area of the indenter. Alternatively, the hardness can be calculated based on the projected area,  $A_p$ , of the indent using equation 11 (Fischer-Cripps, 2007). The hardness based on projected area can be compared with other tip geometries and has a more physical meaning.

$$A_p = \frac{d_v^2}{2} \quad (11)$$

In order to find the depth of the indent,  $h$ , the average of the diagonals is divided by a geometrically derived factor of 7 (Yovanovich, 2006).

### 2.3.8 Corrections for Non-Ideal Geometries

Ideal contact areas mentioned above assume the surface of the indented material remains horizontal. For many actual indents, material is pushed out the sides of the indent to cause “pile-up”.

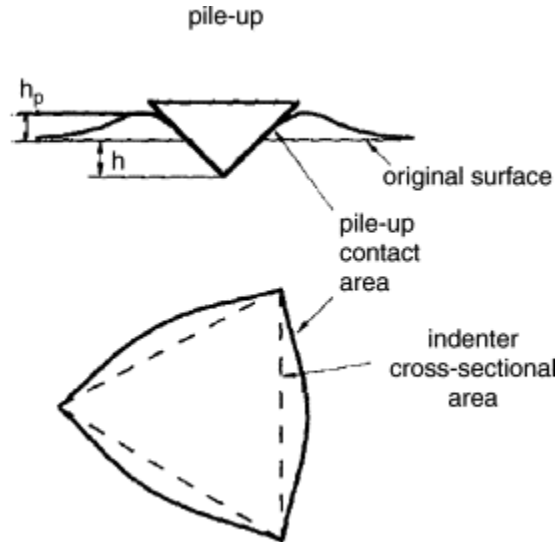


Figure 32: Diagram showing pile-up (McElhane et al. 1998)

The additional contact area due to pile-up can be accounted for by adding the height of the pile-up to contact height,  $h_c$ .

The tip area functions shown previously assume perfect indenter tip geometry. In reality, no tip is perfectly sharp and will have some associated roundness. Additionally, the tips wear over time and the radius of the tip will continue to increase.

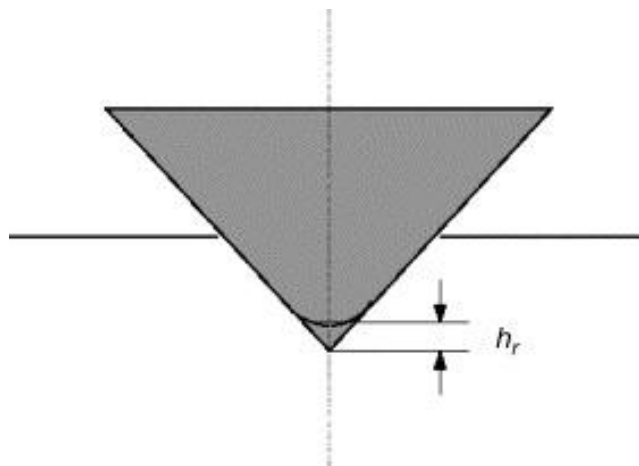


Figure 33: Indenter tip rounding diagram (Zong and Soboyejo, 2005)

Tip roundness can be accounted for in Berkovich and Vickers tips, by assuming the tip to take a combination of spherical and conical shapes as shown in equation 12 below.

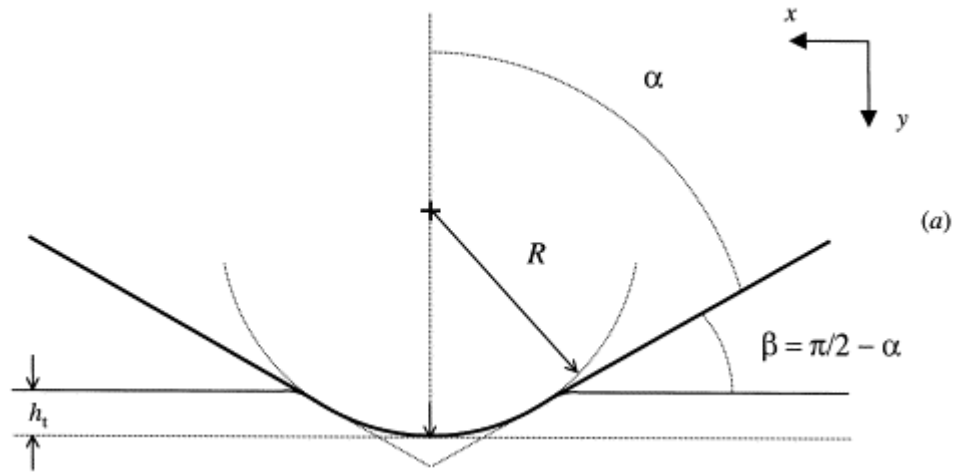


Figure 34: Transition from spherical to sharp indenter (Goldstone et al., 2000)

$$h_t = 2R(1 - \sin\alpha) \quad (12)$$

Other researchers account for the tip rounding effect by adding additional height (blunting distance) to the original  $h_c$  value as well as the height from pile-up (Zong and Soboyejo, 2005).

$$h_c = h + h_p + h_r \quad (13)$$

Most nanoindentation systems come with software allowing for calibration to more closely approximate the actual tip area. Typically these calibrations use polynomials with a series of area coefficients ( $C_0$ ,  $C_1$ , etc.) which are used to fit to an area. The coefficients are found by indenting a flat, consistent material such as fused quartz. These calibration materials have a known hardness and modulus, but do not have pile-up effects. This contact area function can account for imperfections in the contact area such as tip rounding, but does not account for pile-up.

$$A = C_0(h_{correct})^2 + C_1(h_{correct}) + C_2(h_{correct})^{\frac{1}{2}} + C_3(h_{correct})^{\frac{1}{4}} + \dots \quad (14)$$

### 2.3.9 Current Experimental Results for Aluminum and Titanium Alloys

Some limited work has been done on indentation size effect in 6061 aluminum and Ti-6Al-4V alloys, but more work is needed to capture the transition between the micro and nano regimes. Haghshenas et al. (2012) performed nanoindentation on 6061-O and 6061-T6 and reported a strong ISE. However, the focus of the study was on studying strain rate effect rather than plasticity effects.

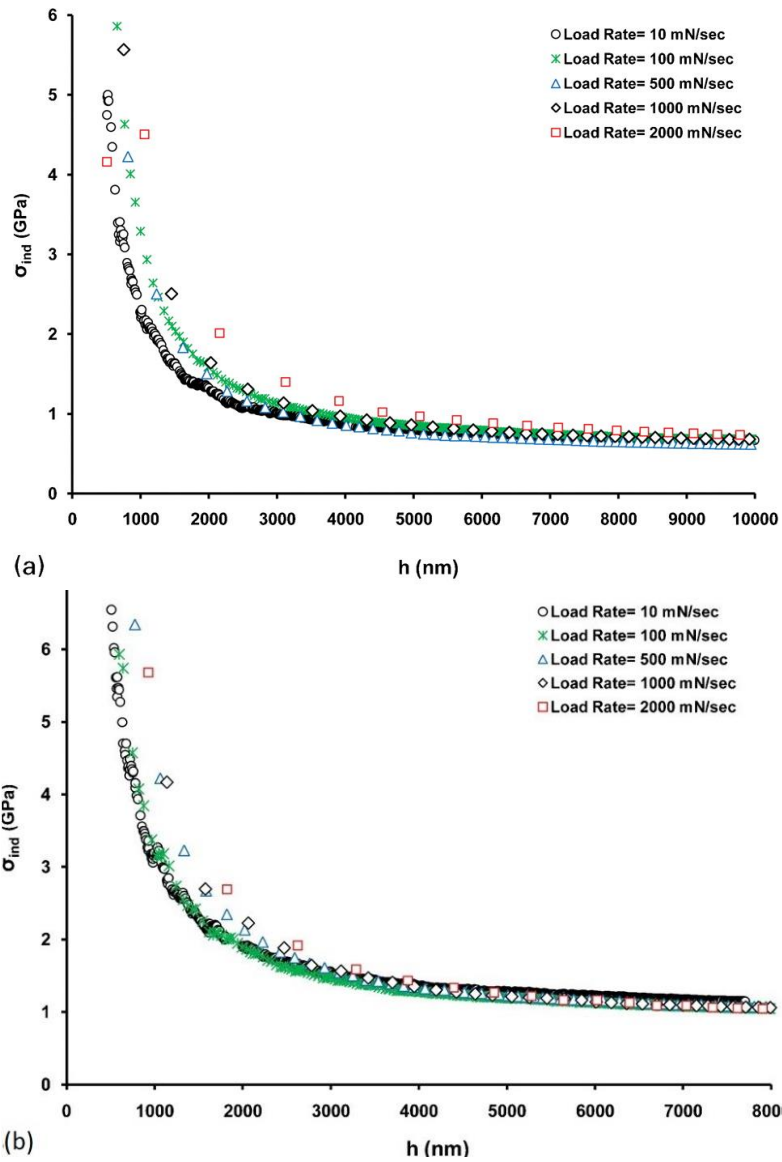


Figure 35: Average indentation stress,  $\sigma_{ind}$ , versus indentation depth,  $h$ , for 6061 aluminum alloy test material, indented at four loading rates, in 6061-O (a), and 6061-T6 (b) conditions (Haghshenas et al. 2012)

Ambriz et al. (2011) also studied the ISE using an instrumented Vickers indenter in 6061 for the base metal and welds. Their analysis differed from Nix and Gao methods, but the initial linearization methods were the same.

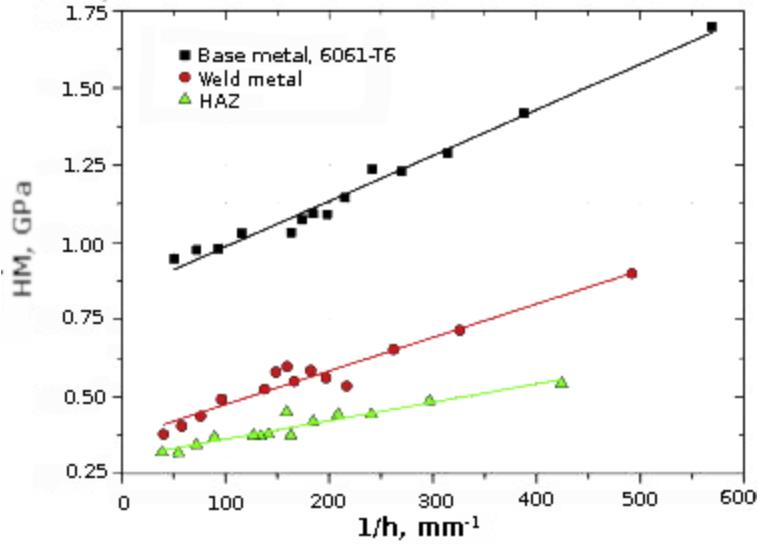


Figure 36: Linearized Meyer's harnesses from an instrumented Vickers hardness tester (Ambriz et al. 2011)

Cai et al. (2011) applied Nix and Gao methods to microhardness testing of Ti-6Al-4V using a Berkovich tip. Again, the ISE was demonstrated in this alloy, but the nanoscale regime was not covered in this work.

Table 6: Variation of statistically stored hardness,  $H_0$ , and characteristic length,  $h^*$  with quenching temperature (Cai et al. 2011)

Quenching temperature	$H_0$ (GPa)	$h^*$ ( $\mu\text{m}$ )
900 °C	3.8031	1.2036
925 °C	4.0149	1.7122
950 °C	3.9506	1.2905
970 °C	3.9108	0.8579

The hardness of cold sprayed 6061 aluminum alloy coatings has been measured, but the author is not aware of any ISE work on this material.

Table 7: Hardness and modulus comparison for wrought 6061-T6 aluminum and 6061-T6 cold spray powder deposits (Hall et al. 2008)

Sample ID	Depth (nm)	Avg.'d CSM results (100-200nm)		Results using Unloading Curve	
		E (GPa)	H (GPa)	E (GPa)	H (GPa)
6061 T6 Bulk Wrought	1000	87.5±3.6	1.464±0.132	85.7±2.0	1.411±0.028
6061 T6 Bulk Wrought	250	86.7±1.6	1.450±0.054	89.3±8.2	1.385±0.044
6061 coating as-received powder	1000	87.9±3.3	1.322±0.278	90.8±5.5	1.349±0.169
6061 coating as-received powder	250	86.7±3.4	1.363±0.458	92.4±10.1	1.347±0.325
6061 coating LN2 milled powder	1000	84.4±1.6	2.621±0.309	86.0±2.6	2.306±0.275
6061 coating LN2 milled powder	250	83.9±1.7	2.715±0.198	90.4±5.9	2.416±0.172

Contrarily, Munagala et al. (2018) completed an ISE study on cold sprayed Ti-6Al-4V and applied Nix and Gao methods in the nano regime. As can be clearly seen, the results are quite different from the results from Cai et al. (2011) in the micro regime.

Table 8: Nanohardness of Ti-6Al-4V cold spray coatings compared with bulk Ti-6Al-4V plate (Munagala et al. 2018)

Sample	$H_o$ , GPa	$h^*$ , nm
Ti6Al4V coatings deposited using SM powders	5.49 ± 0.05	13 ± 2
Ti6Al4V coatings deposited using IM powders	4.45 ± 0.01	39 ± 4
Bulk Ti6Al4V plate	4.17 ± 0.04	20 ± 4

Munagala's indentation of the cold spray deposits suffered from particle debonding in many of the indents, resulting in lower measured hardness.

## 2.4 Fracture

### 2.4.1 General Discussion

Fracture mechanics is the study of the effects of cracks in materials, while fracture toughness is a measure of the ability of a material to resist crack nucleation and growth. It can also be thought of as the amount of energy absorbed for a crack to move one unit of area (ASM

Handbook Volume 19, 1996). Linear-elastic fracture toughness (which can be reasonably applied to the materials of interest in this paper), is determined from the stress intensity factor,  $K$ , at which a thin crack starts to grow in a material. Cracks are three-dimensional imperfections that serve as stress risers. All materials are considered to contain existing cracks, and surface conditions, as well as microstructure, will affect the ability of cracks to form and grow (Soboyejo 2002). There are three modes of fracture shown in Figure 37. However, mode I is typically the source of failure in practice. Hence, we will focus on mode I in all of the discussion henceforth.

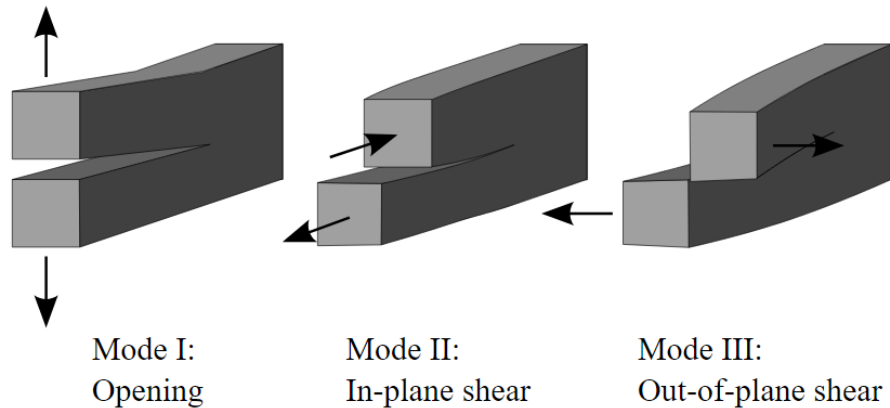


Figure 37: Fracture modes (User Twisp 2008)

The strain energy release rate,  $G$ , is significantly impacted by the ductility of the material. Ductility in a material increases the strain energy release rate, while brittleness decreases toughness. However, the elastic modulus of the material is also important, as the fracture toughness,  $K$ , can be related to  $G$  through the following equation (Zehnder 2012).

$$K = \sqrt{E'G} \tag{15}$$

Materials are also made tougher by various mechanics which redirect the crack, blunt the crack, or release energy and cause crack closure through phase transformations and twinning (Soboyejo 2002).

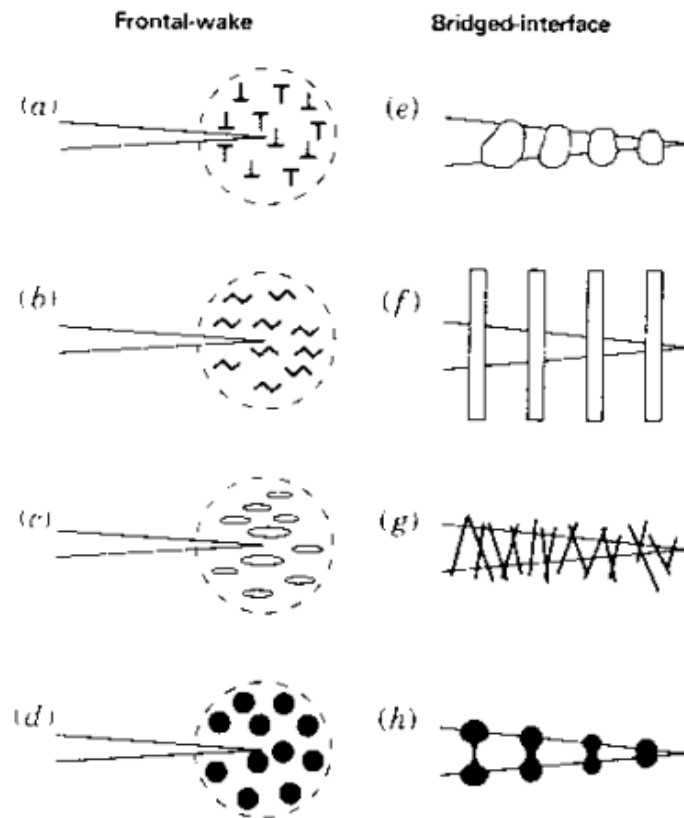


Figure 38: Crack-tip shielding mechanisms. Frontal zone: dislocation cloud (a); microcrack cloud (b); phase transformation (c); ductile second phase (d). Crack-wake bridging zone: grain bridging (e); continuous-fiber bridging(f); short-whisker bridging (g); ductile second phase bridging(h) (Lawn 1993)

Many tests have been developed in attempts to measure fracture toughness, each with their own advantages and disadvantages. The consistent factor among most fracture toughness tests for metallic materials is a notch to try to force crack propagation from a particular location (ASTM E1820). A crack is then grown from this notch using fatigue in order to get a true sharp crack (Soboyejo 2003).

#### 2.4.2 Wrought 6061 Aluminum Alloy

Fracture toughness of 6061 is lower than many other common structural alloys (see Table 9 below), despite the alloy being relatively ductile. Duplex dimple distributions are typically seen in aluminum alloys including 6061. However, aluminum alloys have lower Young's moduli than many other structural materials such as low carbon steels.

Table 9: Fracture toughness of common structural alloys from CT specimens (Henry et al. 1995)

Alloy	Mean value of fracture toughness, $J_c$ ( $J/m^2$ )	Standard deviation in fracture toughness, $J_c$ ( $J/m^2$ )	Mean value of critical stress intensity, $K_{Ic}$ ( $MPa\ m^{0.5}$ )	Standard deviation in critical stress intensity, $K_{Ic}$ ( $MPa\ m^{0.5}$ )
Aluminum alloy, 6061-O	0.125	0.009	93	3.4
Aluminum alloy, 7075-O	0.075	0.008	71.7	3.5
Copper nickel, Cu-Ni alloy, 70/30	0.282	0.029	176	9.1
Magnesium alloy, AZ31B	0.052	0.003	48.4	1.4
Low carbon steel, 1018	0.342	0.039	266	15
Alloy steel, 4130	0.218	0.021	212	10
Low alloy steel, HP9-4-20	0.245	0.023	218	11

Heat treatment processes which increase the yield strength tend to reduce the fracture toughness in most alloys such as in Figure 39.

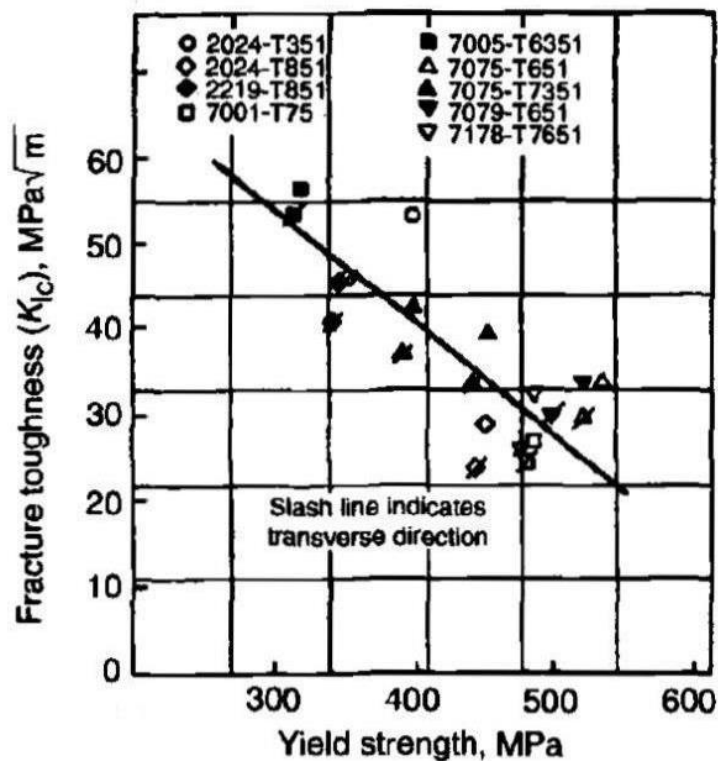


Figure 39: Relationship between yield strength and  $K_{Ic}$  for aluminum alloys (ASM Handbook Volume 19, 1996)

However, this negative correlation between yield strength (in a given alloy) and fracture toughness is not always the case as seen in Table 10 below.

Table 10: Impact of interrupted aging and secondary hardening on fracture toughness of aluminum alloys (Polmear et al. 2017)

Alloy and treatment	0.2% proof stress (MPa)	Tensile strength (MPa)	Elongation (%)	Fracture toughness, $K_{IC}$ (MPa m <sup>0.5</sup> )
2014-T6	414	488	5	26.9
2014-T6I6	436	526	10	36.2
6061-T6	267	318	13	36.8
6061-T6I6	299	340	13	58.4
6061-T6I4	302	341	16	43.2
7050-T6	546	621	14	37.6
7050-T6I6	574	639	14	41.1
7050-T6I4	527	626	16	52

The specimen type can also have an impact on the measured fracture toughness. Work by Davis et al. (1968) suggests that the exact crack propagation direction and differing frictional effects can cause variations in measured fracture toughness between specimen types.

Table 11: Comparison of mean values of  $J_c$  for various specimen geometries and alloys (Henry et al. 1995)

Alloy	Mean values of $J_c$ , J/mm <sup>2</sup>		
	Compact tension (CT) specimens	Center cracked (CC) specimens	Double edge cracked (DEC) specimens
6061-0	0.125	0.115	...
7075-0	0.075	0.078	0.065
70/30	0.282	0.285	...
AZ31B	0.052	0.054	0.048
1018	0.342	0.368	...
4130	0.218	0.248	0.216

Many constitutive particles such as Mg<sub>2</sub>Si negatively impact fracture toughness. Reducing the Fe and Si content improves the fracture toughness of 2xxx and 7xxx alloys seen in Figure 40 below (ASM Handbook Volume 19, 1996).

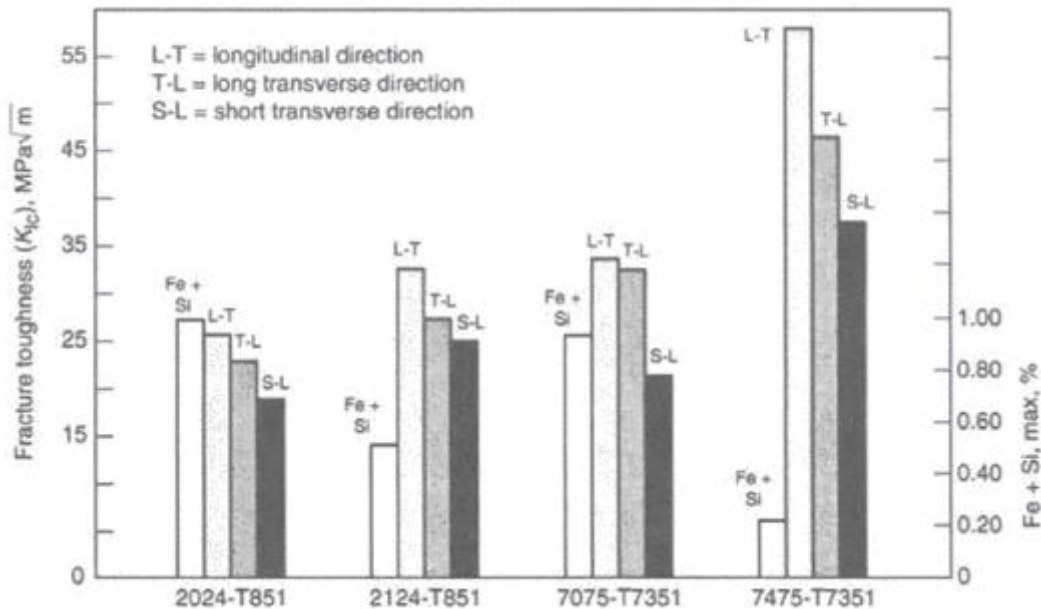


Figure 40: Impact of Fe and Si content on fracture toughness of aluminum alloys (Bucci 1979)

#### 2.4.3 Cold Sprayed 6061 Aluminum Alloy

The author is not aware of any studies determining the  $K_{IC}$  fracture toughness in cold sprayed 6061 aluminum alloys. A significant obstacle to obtaining  $K_{IC}$  for cold sprayed aluminum is the thickness recommended for aluminum alloys in ASTM B645-10 shown by the required ligament size ( $W-a$ ) in equation 16.

$$(W - a) \geq 5 \left( \frac{K_Q}{\sigma_y} \right)^2 \quad (16)$$

Meeting the ASTM specification for  $K_{IC}$  in aluminum alloys requires material thicknesses of greater than 80 mm, which is expensive when cold sprayed. One of the reasons for this criteria is to give enough space to ensure the crack tip field does not interact with the boundaries of the sample. As a result of this limitation, the results from samples with smaller ligament sizes cannot be used as  $K_{IC}$  values but rather as  $K_Q$  values with the understanding that the results may be partially dependent upon the sample size.

#### 2.4.4 Ti-6Al-4V Bulk Material

Ti64 alloys can have a wide range of fracture toughness depending upon the precise processing and microstructure. In particular, increasing the amount of transformed alpha rather than equiaxed alpha, significantly increases the fracture toughness as seen in Table 12 below. It is believed that this is because the transformed alpha provides a difficult path for crack propagation (ASM Handbook Volume 19, 1996).

Table 12: Titanium structural alloys dependence of fracture toughness on alpha phase morphology (ASM Handbook Volume 19, 1996)

Alloy	Alpha morphology	Yield Strength (MPa)	Fracture Toughness, $K_{Ic}$ (MPa $\sqrt{m}$ )
Ti-6Al-4V	Equiaxed	910	44-66
Ti-6Al-4V	Transformed	875	88-110
Ti-6Al-6V-2Sn	Equiaxed	1085	33-55
Ti-6Al-6V-2Sn	Transformed	980	55-77
Ti-6Al-2Sn-4Zr-6Mo	Equiaxed	1155	22-23
Ti-6Al-2Sn-4Zr-6Mo	Transformed	1120	33-55

Oxygen has the most significant effect on fracture toughness of the other elements in a Ti64 alloy. Ferguson and Berryman (1976), found a reduction of  $3.7 \text{ MPa}\sqrt{m}$  per 0.01% increase in oxygen content. Hydrogen has been shown to generally reduce the fracture toughness of Ti64 as seen in Table 13.

Table 13: Impact of hydrogen and oxygen content on Ti-6Al-4V mode I fracture toughness (ASM Handbook Volume 19, 1996)

Hydrogen content, ppm	$K_{Ic}$ at room temperature, $\text{MPa}\sqrt{m}$
At 0.16 wt.% oxygen	
8	145
36	118
53	104
122	100
At 0.05 wt.% oxygen	
9	133
36	125
50	96
125	101

As for most materials, the fracture toughness in Ti64 has significant dependence on processing texture and orientation seen in Table 14.

Table 14: Impact of processing texture on tensile properties and  $K_{Ic}$  (Harrigan et al. 1973)

Test direction	Tensile strength	Yield strength	Elongation	Reduction in area	Elastic modulus	$K_{Ic}$	$K_{Ic}$ specimen orientation
	MPa	MPa	%	%	GPa	$\text{MPa}\sqrt{m}$	
L	1027	952	11.5	18	107	75	L-T
T	1358	1200	11.3	13.5	134	91	L-T
S	938	924	6.5	26	104	49	S-T

#### 2.4.5 Cold Sprayed Ti-6Al-4V

Similarly, the author is unaware of any studies determining true  $K_{IC}$  fracture toughness for cold sprayed Ti64. However, fractography on bend samples has shown that cracks often propagate between the intersplat boundaries of the cold spray powder deposits (Tan et al. 2018).

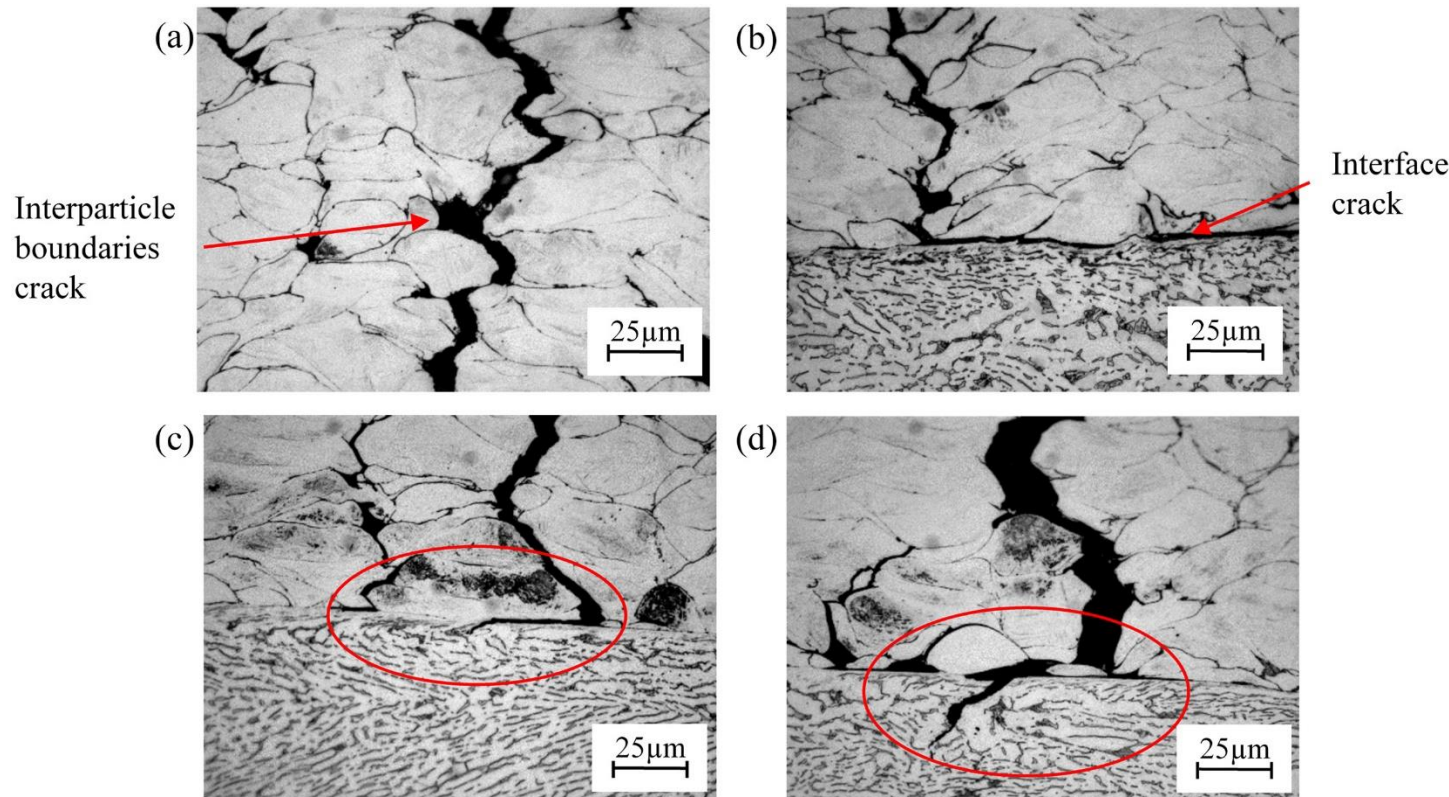


Figure 41: Fractography of a Ti-6Al-4V coating showing crack propagation along intersplat boundaries (Tan et al. 2018)

#### 2.5.6 Fracture of Cold Spray Coatings

For cold spray coatings fracture, the crack can continue straight from the coating to the substrate or can cause delamination between the coating and the substrate. A straight through crack can be modeled like a traditional fracture specimen. However, interfacial cracks require a different fracture mechanics treatment as described by Evan's et al. (1990). Interfacial crack systems can first be described using the Dundur's parameters (1969) using the elastic properties of both materials.

$$\alpha = \frac{\mu_1(1 - \nu_2) - \mu_2(1 - \nu_1)}{[\mu_1(1 - \nu_2) + \mu_2(1 - \nu_1)]} \quad (17)$$

$$\beta = \frac{\mu_1(1 - 2\nu_2) - \mu_2(1 - 2\nu_1)}{2[\mu_1(1 - \nu_2) + \mu_2(1 - \nu_1)]}$$

$\mu$  is the shear modulus and  $\nu$  is the Poisson's ratio in equation 17 above. Nonzero values of  $\beta$  cause oscillation in the crack tip stress and displacement fields making solutions difficult to find. A redemptive factor in many bimaterial systems is that  $\beta$  is small and can be assumed to be zero. The mode mixity for interfacial cracks can be represented using Figure 42.

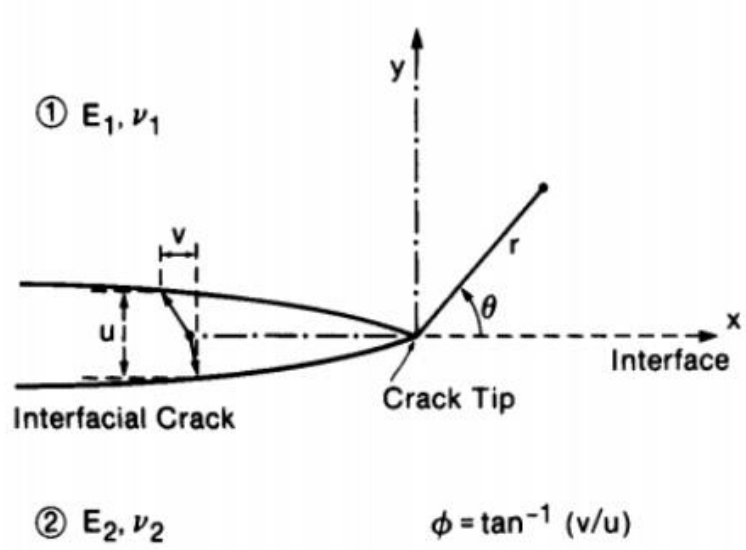


Figure 42: Mode mixity of an interfacial crack (Evan's et al. 1990)

For an interfacial crack, the strain energy release rate,  $G$ , can be modelled by equation 18 using  $u$  and  $v$  as surface displacements for the crack and  $\mu$  as the shear modulus and  $\nu$  as the Poisson's ratio. A parameter,  $\epsilon$ , related to the Dundurs' parameters is also used in the energy release rate definition.

$$\epsilon = \frac{1}{2\pi} \ln \frac{(1 - \beta)}{(1 + \beta)} \quad (18)$$

$$G = \frac{\pi(u^2 + v^2)(1 + 4\epsilon^2)}{8 \left[ \frac{(1-v_1)}{\mu_1} + \frac{(1-v_2)}{\mu_2} \right]} \quad (19)$$

The phase angle of loading,  $\psi$  is an important measure of the mode mixity of shear to opening of the interface crack surface. Assuming  $\beta=0$ , equation 20 below defines the mode mixity.

$$\psi = \tan^{-1}(v/u) \quad (20)$$

A four-point bending specimen shown in Figure 43 can be used to test the delamination fracture properties of the cold sprayed material.

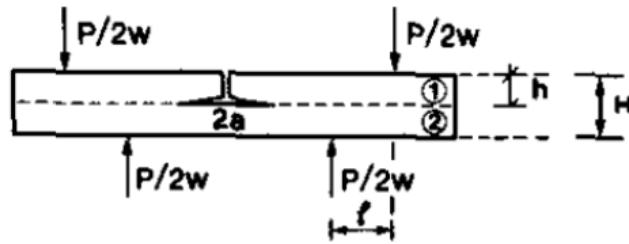


Figure 43: Four-point bending delamination specimen (Evan's et al. 1990)

The specimen has been described by Evan's et al. (1990) using the non-dimensional expression below.

$$\frac{GE_2b^2H^3}{P^2l^2(1-v_2^2)} = F \left( \frac{a}{l}, \alpha, \frac{h}{H} \right) \quad (21)$$

Where  $P$  is the load,  $l$  is the moment span,  $b$  is the specimen width,  $H$  is the total thickness,  $h$  is the thickness of the outer layer,  $a$  is the crack length, and  $F$  is a function.

## 2.5 Fatigue

### 2.5.1 General Discussion

Fatigue is the damage response of a material under cyclic loading. This damage occurs through the initiation and propagation of cracks within the material. The simplest method for measuring fatigue is known as the S-N curve, which plots the applied stress versus the number of cycles. S-N curves however, are impacted by surface topography and frequently will have fatigue lives ranging by order of magnitude for the same material (ASM Handbook Volume 19, 1996, Barsom and Rolf, 1999). This is a major limitation when trying to make any interpretations about the quantized microstructural effects on fatigue life. A fracture mechanics approach commonly

used for modeling fatigue crack growth is Paris' law (Paris et al. 1961), which defines the relationship between crack growth,  $da/dN$  and the change in stress intensity factor,  $\Delta K$ . This simple power law fit can use experimental measurements to determine constants  $C$  and  $m$  in the equation.

$$\frac{da}{dN} = C(\Delta K)^m \quad (22)$$

A material's fatigue response is affected by many factors including fracture toughness, surface topography, microstructure, environment, mean stress, and stress ratio ( $R$ ). Despite the many factors influencing fatigue, crack growth in ductile solids will typically result in an idealized curve similar to that shown in Figure 44.

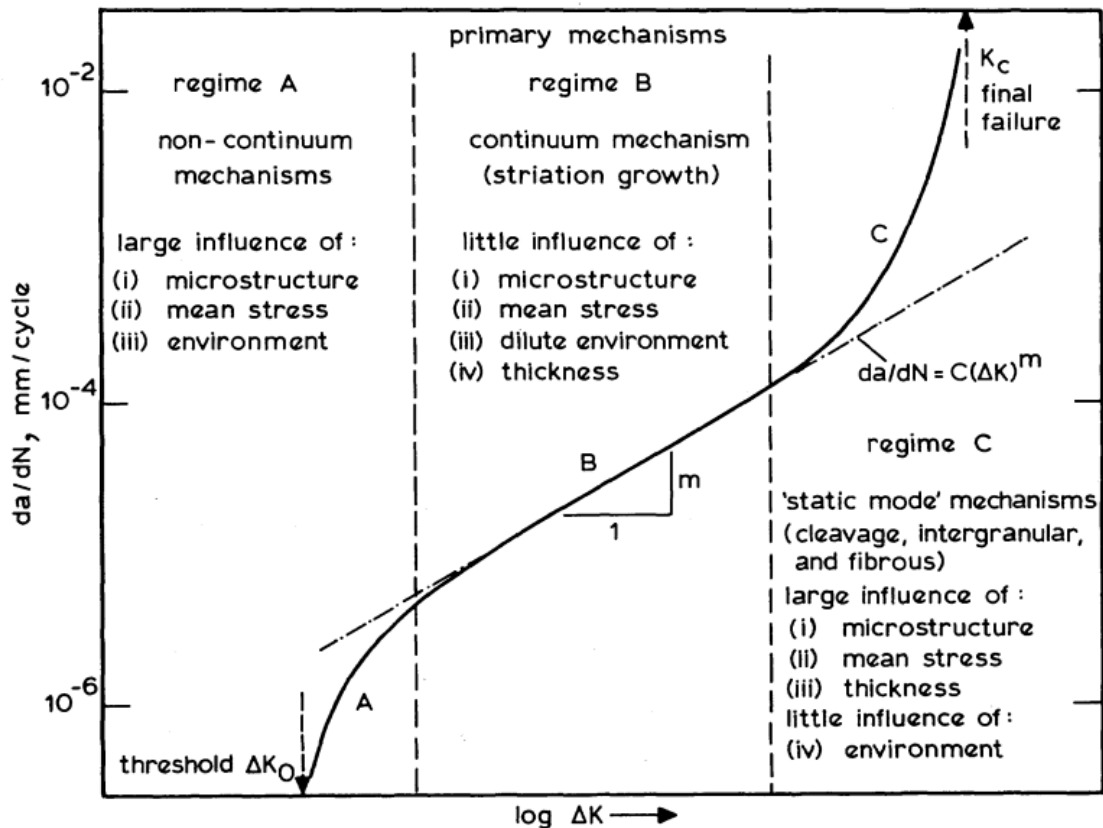


Figure 44: Idealized crack growth cycle with three primary regimes (Ritchie 1979)

Other researchers have proposed models which account for parameters in addition to  $\Delta K$ . A model by Soboyejo et al. (1998) incorporates the max stress intensity factor,  $K_{max}$ , stress ratio,  $R$ , temperature,  $T$ , and cyclic frequency,  $f$ . All  $\propto$  values are constants which can be solved for using multiple linear regression.

$$\frac{da}{dN} = \alpha_0 (\Delta K)^{\alpha_1} (R)^{\alpha_2} (K_{max})^{\alpha_3} (T)^{\alpha_4} (f)^{\alpha_5} \quad (23)$$

Cracks oft initiate in areas of high stress concentrations such as notches, inclusions, or energy differences within the microstructure. Dislocation slip causes the formation of intrusions and extrusions which evolve into microcracks in the material (Soboyejo, 2003). Various models of crack extension have been proposed, but one of the most widely recognized considers a cycle of crack blunting during opening and subsequent sharpening due to plastic flow.

Cracks can be divided into long cracks which can be approximated by LEFM and short cracks which occur at a lower stress intensity. Short cracks often grow differently from long cracks and may be measured using strain energy density,  $\Delta J$ , and crack tip opening displacement, CTOD (Soboyejo, 2003).

#### 2.5.2 Wrought 6061 Aluminum Alloy

Many modern aluminum alloys such as 6061 have relatively high strength and toughness values contributing to higher fatigue life. However, fatigue damage in aluminum alloys can still be a significant issue at practically all loads as many researchers do not believe they exhibit endurance limits (Askland, 2003). Directionality and microstructure are generally not major factors in aluminum alloy fatigue life (ASM Handbook Volume 19, 1996, Kaufman, 2008), but they can be important for crack growth. The more corrosion resistant the aluminum alloy the longer the fatigue life in more corrosive environments. However, porosity has been found to produce significant differences in fatigue life (Brockenbrough et al. 1993, Mayer et al. 2003).

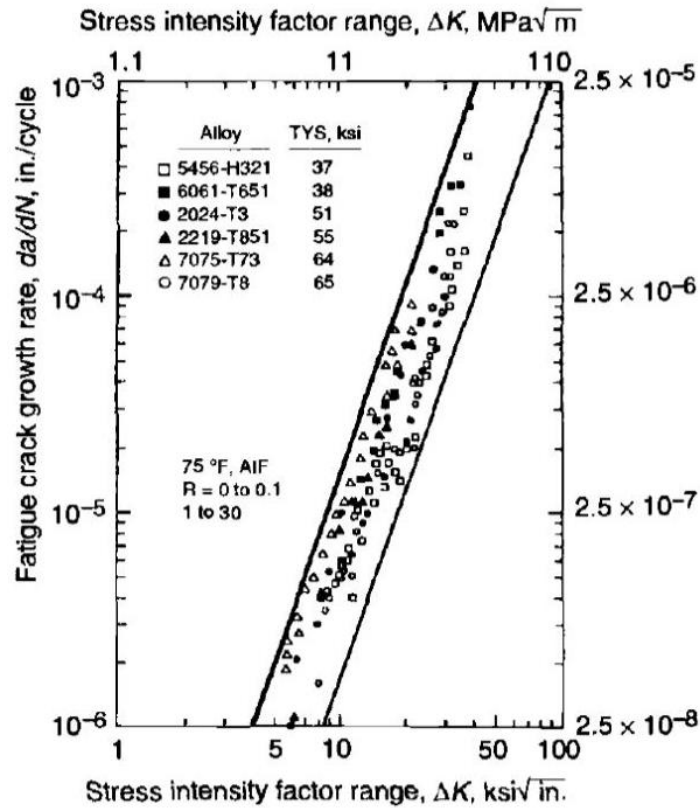


Figure 45: Fatigue crack growth rates for various aluminum alloys (DiMatteo, 1996)

### 2.5.3 Cold Sprayed 6061 Aluminum Alloy

The body of work on fatigue of cold sprayed materials is quite small at the moment. Given the variability that is common within fatigue results, it is dangerous to draw confident conclusions at the moment, but some trends can be noted.

Considering the reported impacts of porosity on wrought aluminum alloy fatigue characteristics, it is not surprising that interparticle boundaries were found to be critical to the fatigue response in cold sprayed 6061 (Gavros et al. 2018). Figure 46 shows that the long and short crack growth rates were faster for the cold sprayed 6061 material than for the rolled 6061 material.

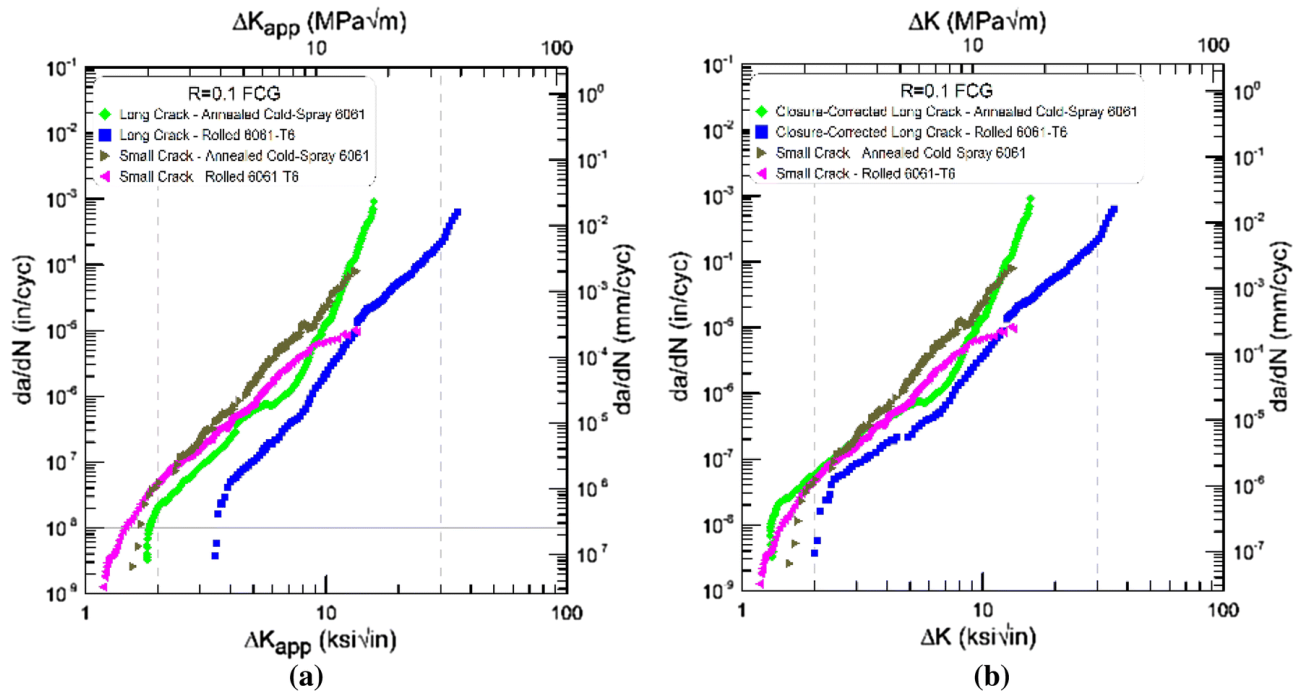


Figure 46: Applied (a) and closure-corrected (b) long and small fatigue crack growth data for annealed 6061 cold-spray and rolled 6061-T6 alloys (Gavros et al. 2018)

#### 2.5.4 Ti-6Al-4V Bulk Material

Titanium materials are generally less susceptible to fatigue damage than aluminum, requiring higher stress intensity factors ranges to exhibit the same crack growth rate. Historically some researchers even claimed that titanium alloys have a fatigue limit (endurance limit) in which they can survive an infinite number of cycles without growing cracks. More recent work has called the existence of fatigue limits into question (Bathias 2001), but the fact remains that for lower loads, titanium alloys experience much longer fatigue limits/ slower fatigue crack growth rates.

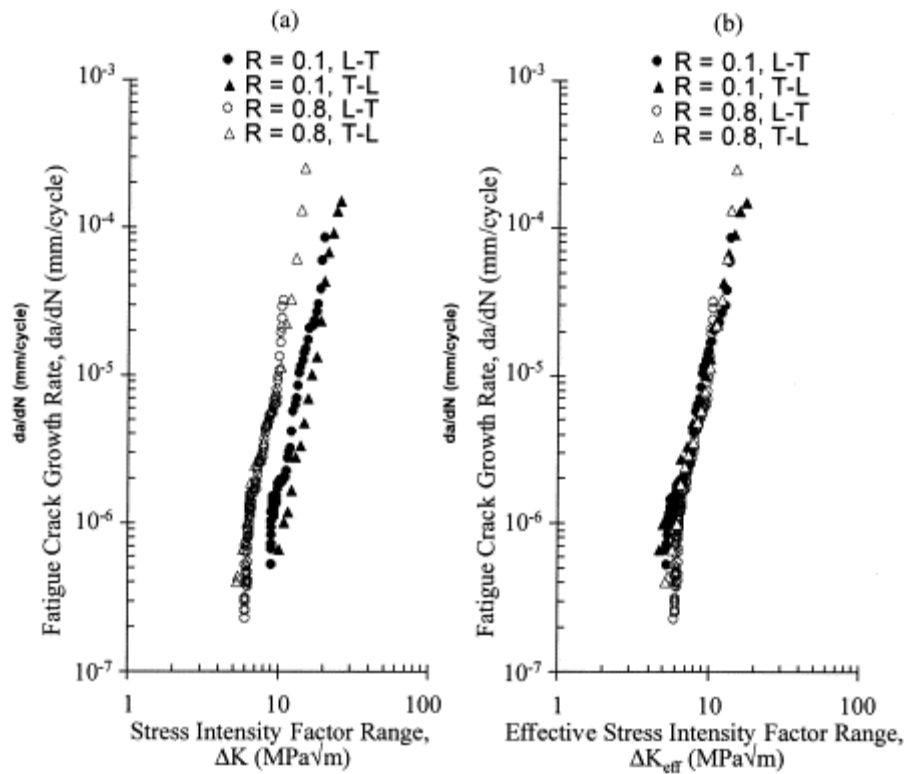


Figure 47: Fatigue crack growth rate versus stress and effective stress intensity factor ranges for Ti-6Al-4V (Sinha et al. 2000)

Corrosion fatigue generally has little impact on titanium alloys with mechanical loading being the main driver of crack growth (Henry et al. 1995). Microstructure and interstitial oxygen on the other hand have been found to have a significant impact on fatigue properties in titanium alloys.

#### 2.5.5 Cold Sprayed Ti-6Al-4V

Some work has been done on delamination of Ti64 coatings from Ti64 substrates, but the author is not aware of any studies of fatigue properties in bulk cold sprayed material. Sun et al. (2017) found that Ti-6Al-4V coatings on Ti-6Al-4V substrate had the strongest adhesion and most cycles before delamination with the smoothest substrate surface finishes. A couple of researchers have found that Ti64 coatings on Ti64 substrates cause a small to moderate decrease in fatigue life (Price et al. 2006, Cizek et al. 2013). This is contrary to some work done in other materials and the assumption of a beneficial shot-peening effect by other researchers (Moridi et al. 2015, Ziemian et al. 2014).

## [2.6 Data Science Approach to Materials Science](#)

### [2.6.1 Introduction to Data Science Methods](#)

#### [2.6.1.1 Scaling Data for Appropriate Distances](#)

Mathematical learning techniques use data to “train” a model in order to make predictions. However, before reviewing different models and techniques, it is important to first discuss data preparation. Most models make predictions about data based upon distances between data points. Distances are a measurement of how far apart data are from each other. These distances can be as simple as the Euclidian distance (based upon Pythagorean’s theorem), but can vary depending upon the data set and models being used.

$$d(x, y) = \sqrt{\sum_{i=1}^n (y_i - x_i)^2} \quad (24)$$

For example, one might wish to define distance in a higher dimension which allows easy separation of the data. A kernel distance is just one of many other potential distances. However, no matter which distance is used, care must be taken to ensure distances are meaningful. If data have different units, they should be scaled so they can be compared reasonably. There are several methods of scaling data, but z-score normalization is one of the best due to its ability to remove units while accounting for standard deviation in the data.

$$z = \frac{(x - \mu)}{\sigma} \quad (25)$$

Categorical data such as colors in the example below can use one-hot encoding schemes to change the data to numerical values. It is important to try to preserve distances when transforming categorical data. For example, the seasons; Spring, Summer, Fall, Winter may be encoded as (0,1), (1,0), (0,-1), and (-1,0) (Paffenroth, 2019).

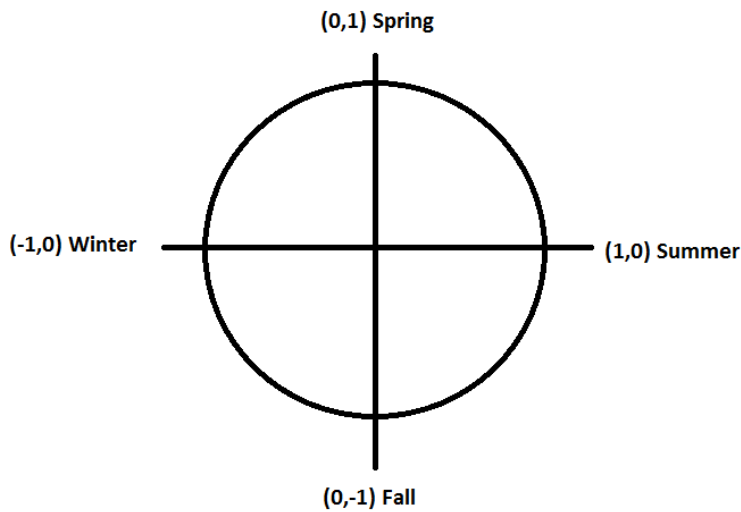


Figure 48: Encoding the seasons using the unit circle

### 2.6.1.2 Data Form

Once the data has been properly scaled, it is important to think about the form of the data and the assumptions which can be made about the data. This provides direction about appropriate models to try. Data can be divided into predictors and responses, where predictors are inputs into a model and responses are outputs from the model. Supervised models make predictions about the likely response based off of known predictors and responses in so-called “training data”. Unsupervised models on the other hand can predict responses based solely on the relationships between predictors.

Table 15: Example dataset showing unscaled predictors and responses

Predictor 1	Predictor 2	Predictor 3	Predictor 4	Response 1
#of rooms	Color of house	Size of home	# of cats in the neighborhood	Home Price
3	Purple	100 m <sup>2</sup>	3	\$500,000
5	White	200 m <sup>2</sup>	15	\$1,000,000

### 2.6.1.3 Bias-Variance Tradeoff

One of the most important concepts in statistical learning is the bias-variance tradeoff, which is an important concept for supervised models. Supervised models are subject to overfitting wherein the model closely fits the data points, but would not accurately predict new data. It is dangerous to make the assumption that a model which has low error on the data you have

given it, will perform well on new data. The blue line in Figure 49 below is an example of a model which is overfitting. As is apparent, the model hits all of the data points exactly, but does not capture the true trend of the data well. It is very likely that new data introduced to the model would not fit well with the model. In this example, a linear regression model (black line) was also used to fit the data.

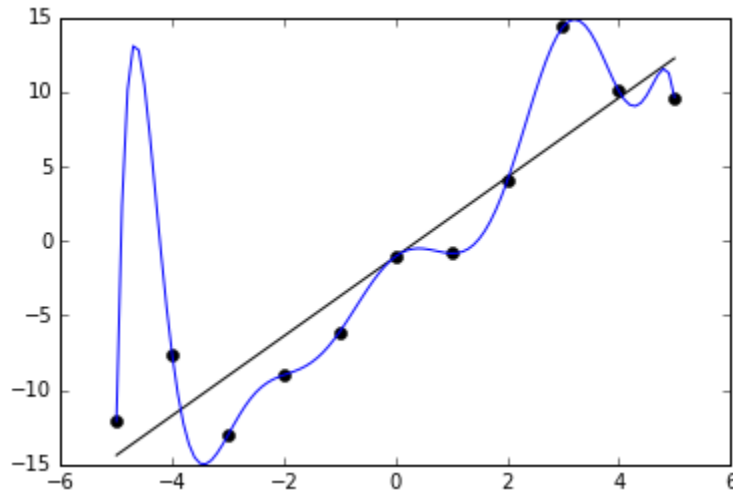


Figure 49: Example of overfitting on roughly linear data (Ghiles)

The linear regression model used here does not hit the data points exactly, therefore having higher error on those points, but likely does a better job of predicting new data points. Bias is defined as the error in the model, while variance is the amount the model response would change given new or different data (Gareth et al. 2013). The black line in Figure 49 has high bias relative to the blue line, while the blue line has higher variance.

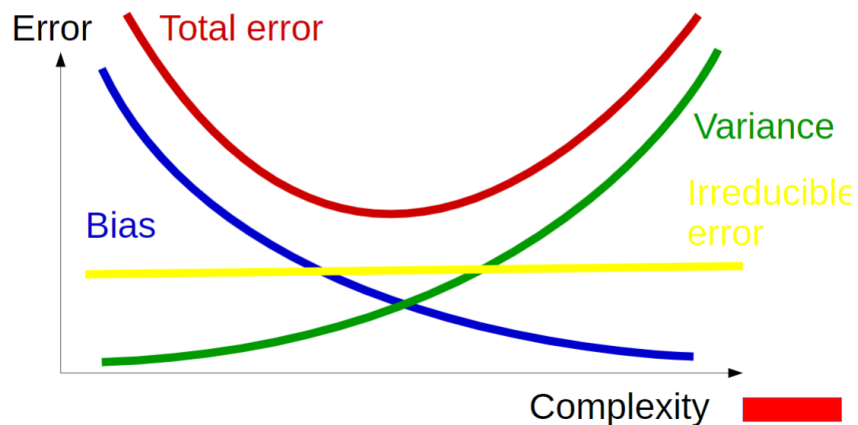


Figure 50: Bias-variance tradeoff (Paffenroth, 2019)

The ideal model reduces the total error, by finding a compromise between the bias and variance curves shown in the schematic above. However, as mentioned previously, it is

important to ensure the model is not overfitting. A common way to prevent model overfitting is to separate a dataset into “training” and “testing” data. The training data is the data which the model is originally applied to and learns on. Testing data is reserved for making predictions given new data and comparing the predictions to the actual response values in the data. Good models have a low testing error. A low training error does not necessarily mean the model will have a low testing error as the model may be overfitting. Thus far, error has been mentioned numerous times, but has not been defined. The most common measurement of error is the mean square error (MSE), which produces lower values the closer predicted responses are to actual responses (Gareth et al. 2013).

$$MSE = \frac{1}{n} \sum_{i=1}^n (y_i - \hat{y}_i)^2 \quad (26)$$

#### *2.8.1.4 Data Snooping*

Data snooping is when a researcher/ model employed by the researcher is able to “look” at the testing data during training of the model. If the model is able to interact with the testing data in some way, then it has the potential to over fit to the testing data without the researcher’s awareness. This is especially dangerous because the researcher may have confidence in the model due to a low testing error, when in reality the model has over fit to the testing data and therefore fails upon interaction with new data. The effects of data snooping can be relatively benign such as a marketing algorithm which misallocates funds, or dangerous such as the algorithm which misidentifies stall in an aircraft. To guard against data snooping and overfitting, data should first be separated so that a portion is a data is in a “safe” which cannot be tested with the model until the model is in its final iteration. Bootstrapping can be used on the data outside of the safe to introduce randomness into the data for different iterations of the models. Introducing randomness into data helps prevent models from overfitting (Paffenroth, 2019).

#### *2.8.1.5 Choosing a Model*

Given the many types of models which can be used for making predictions, choosing a model can seem like a daunting task. However, some simple approaches can be used in order to streamline the process. First, as mentioned earlier, different models have different assumptions and can work well with different datasets. Therefore, there is no sense is trying a model on a dataset which does not meet the assumptions of that model. For example, linear regression assumes an approximately linear relationship between predictors and responses. Plotting the data often gives intuition into whether the data is approximately linear such as in Figure 49 or non-linear such as in Figure 51.

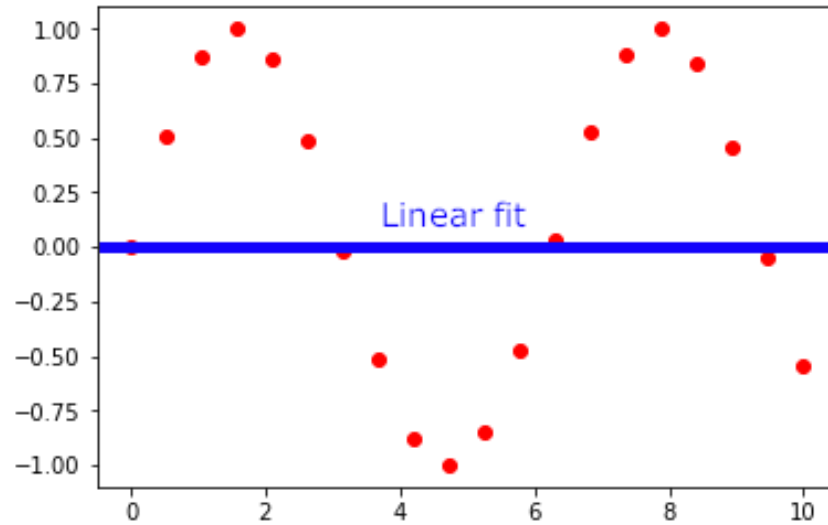


Figure 51: Data points from sine wave with a linear fit

In many cases, the data cannot be meaningfully plotted in two dimensions in order to gain intuition about models to try. Therefore, cross-validation becomes a valuable tool. Cross validation is the process of checking the error (or other associated metric of accuracy) of a chosen model on both testing and training data. Models and model parameters can be cross-validated on bootstrapped datasets to see which reduce error rates or reveal relevant features.

Another important distinction to be made when selecting a model is whether the problem is a classification or regression problem. Regression problems try to use a model to predict a numerical output given a set of inputs. Classification problems on the other hand typically involve a qualitative process of putting data points into categories such as positive and negative or dead and alive. Many models such a linear regression often work better for regression problems, while logistic regression may function as a classification model. However, there can be overlap between the two types of problems, and many models have versions which can work for regression or classification.

There are many classes of models which essentially work by minimizing the distances from a class of functions. For example, linear regression creates a function of a line to make predictions. Alternatively one can image modeling the data with a polynomial function. In either case the training process picks coefficients in the function (such as equation 27below) which minimize some error or loss term.

$$\hat{y} = \hat{\beta}_0 + \hat{\beta}_1 \quad (27)$$

Other major methods for both classification and regression are KNN (K nearest neighbors) and trees. When using KNN for classification, the model makes a classification for a point based

upon the identity of the nearest neighboring points. The benefit of KNN is that it makes no assumptions about the data, so it can be used for almost any datasets. However, the drawback is that KNN requires an exponentially increasing amount of data as the dimensionality of the data increases (Paffenroth 2019). Trees is another method which works well for both regression and classification problems. Regression trees work by making horizontal linear approximations of the data. The number of approximations is equal to the number of “leaves” or decisions in the tree. Trees (and their extensions known as “forests”) are able to handle higher dimensional problems without frequent overfitting and are therefore useful for a large set of problems.

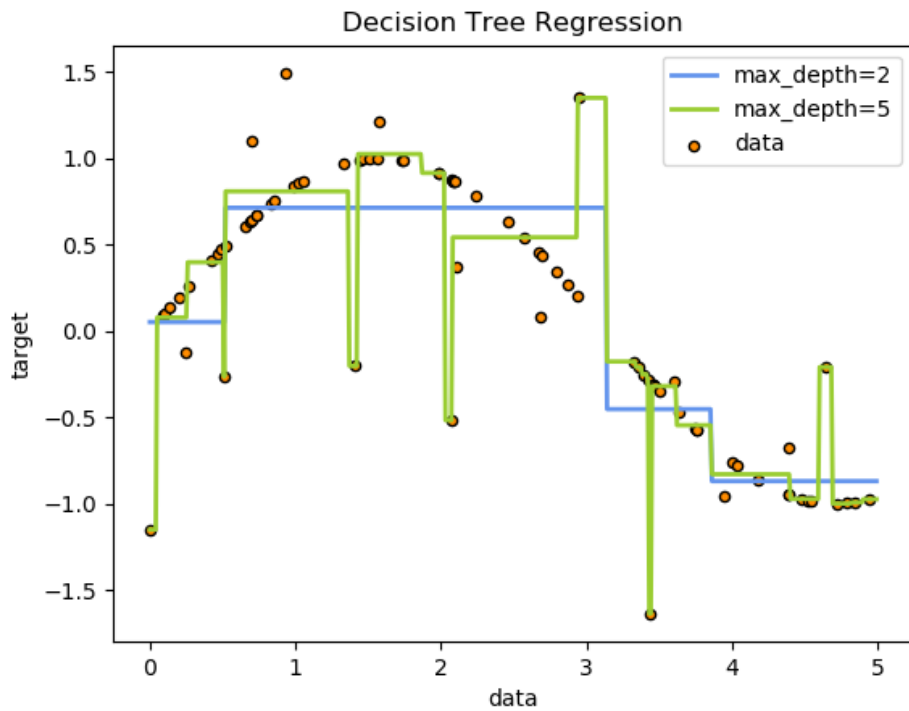


Figure 52: Noisy Sine Wave Decision Tree Regression (Decision Tree Regression)

#### [2.6.1.6 Bias-Variance Tradeoff](#)

Many real world problems have data that exist in high dimensions. Given the propensity of many models to over fit in high dimensions, care must be taken to create a good model. Part of the solution may be to pick a model class such as trees rather than linear regression when dealing with high dimensional problems, but there are other solutions which can open up the problem to additional types of models. One powerful tool for dealing with higher dimensions is principle component analysis (PCA). Principle component analysis is a method of reducing dimensionality and reducing chances of overfitting. PCA also makes data easier to visualize through its dimension reduction. This method creates a low-dimensional representation of a

data set which contains as much as possible of the variation. Dimensions are removed if they have lower variation (therefore containing less interesting information) than other dimensions.

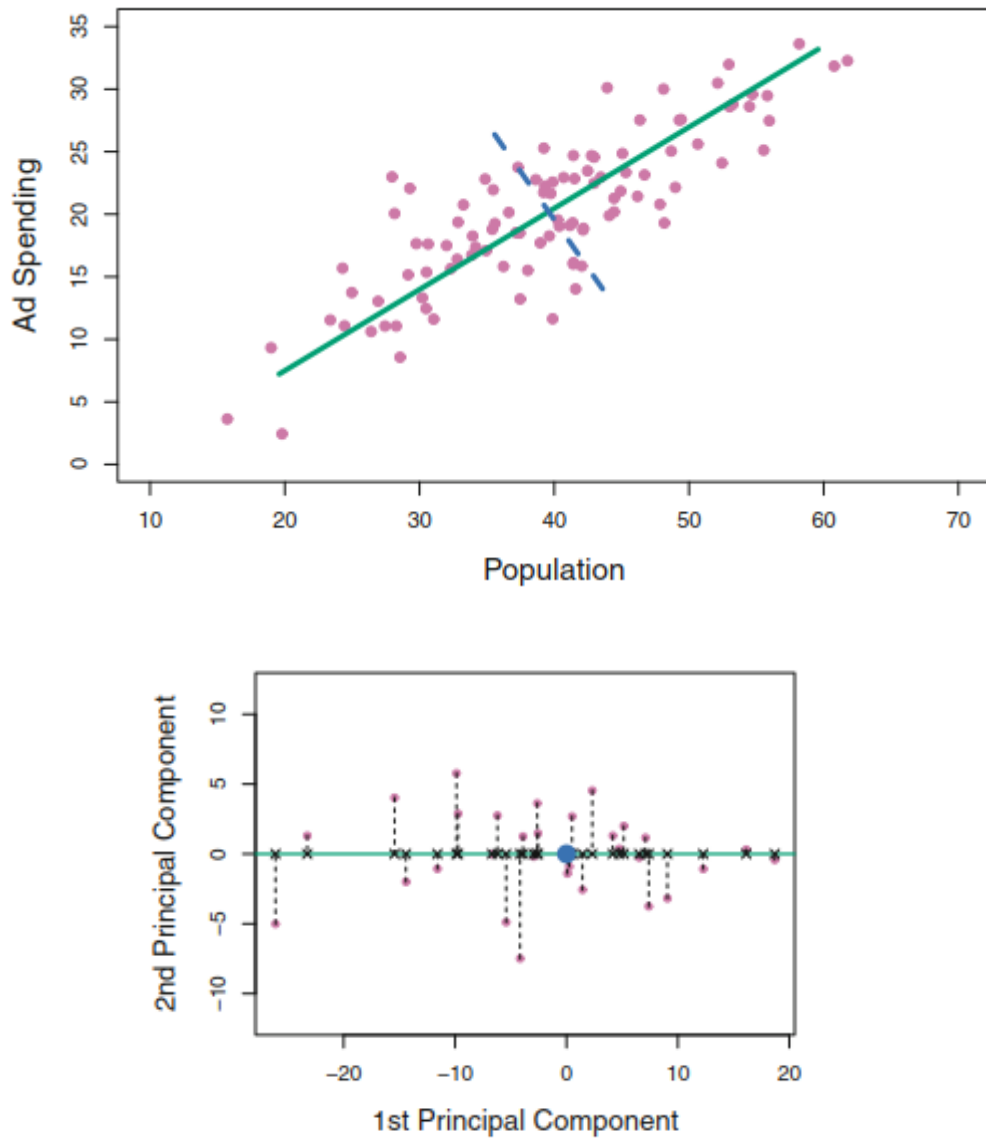


Figure 53: Transformation of data using PCA (Gareth et al. 2013)

PCA creates a new normalized linear equation in the PCA space which is some combination of the features from the previous space as seen in equation 28. The second principal component is defined to be perpendicular to the first.

$$Z_1 = \phi_{11}X_1 + \phi_{21}X_2 + \dots + \phi_{p1}X_p \quad (28)$$

Ultimately, PCA can be thought of as projecting points from a higher dimensional space to a lower dimensional space or projecting onto a flat plane within the original high dimensional space.

Another tool which can reduce data sparsity in high dimensions is lasso regression. Lasso regression is a form of linear regression which uses shrinkage to force data towards some central point using coefficients  $\beta$ .

$$\frac{\min}{\beta} \left[ \sum_{i=1}^n (y_i - \beta_0 - \beta_1 x_1)^2 \right] \quad (29)$$
$$s. t. |\beta_0| + |\beta_1| \leq s$$

An advantage of lasso is that it can reduce  $\beta$  values to zero, meaning that it gets rid of unimportant features (Gareth et al. 2013). This highlights important predictors in the data and reduces data sparsity.

#### [2.6.1.7 Deep Learning](#)

Recently a subset of machine learning, known as deep learning, has emerged as a popular option for providing predictions. Deep learning models use the concept of neural networks to iteratively update the model and its parameters to make increasingly accurate predictions. Neural networks work by using the chain rule in reverse (back propagation) to apply gradients to a function, setting weights in order to minimize a loss. There are many different variations and specific implementations of neural networks which vary in size and solution methodologies, but the general concept is the same. Figure 54 below depicts a simple feed forward neural network where the inputs proceed forward to the outputs without recursion. Each node (colored circle) in the network represents a number, while each arrow represents functions applied in the network. The input layer has nodes for each of the parameters or predictors in the model, while the output layer has nodes containing weighted predictions. Hidden layers are an abstract combination of outputs from the functions connected to them.

### A simple neural network

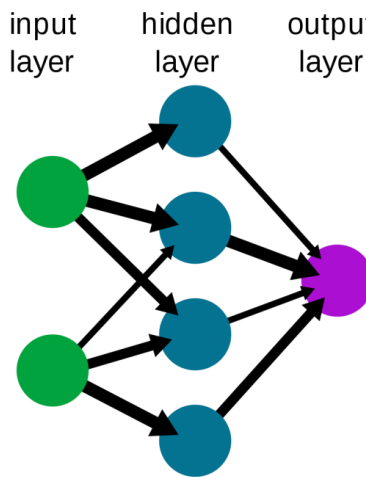


Figure 54: Simple feed forward neural network (Wiso, 2019)

Neural networks can add complexity (and potentially accuracy) by increasing the number or nodes, adding hidden layers, changing the types of function applied, or adding recursion. Many neural networks minimize their functions (arrows in the neural network diagram) using gradient descent. Gradient descent can be conceptually thought of as taking steps down a hill to eventually find the local minimum.

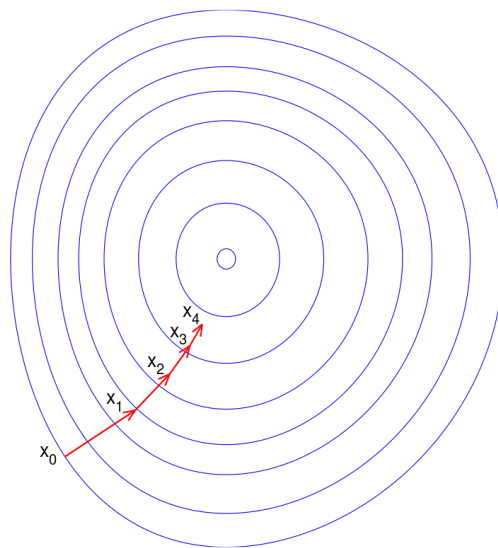


Figure 55: Gradient descent diagram (Olegalexandrov)

Assuming a differentiable function, gradient descent moves toward the local minimum by subtracting the gradient,  $\nabla F(a_n)$ , from the point  $a_n$ . The gradient is multiplied by something called a “learning rate” ( $\gamma$ ), which is essentially the step size in Figure 55 above.

$$a_{n+1} = a_n - \gamma \nabla F(a_n) \quad (30)$$

The larger the learning rate, the faster the network may converge on a local minima. However, if the step size is too large, the network may miss the local minima all together. Another potential issue with gradient descent is that the algorithm may get stuck in local minima and miss more optimal solutions. More advanced versions of gradient descent, such as those including momentum can help avoid getting stuck in non-optimal solutions (Bushaev, 2017). Other methods such as Nesterov accelerated gradient help to accelerate convergence (Nesterov, 2004). However, avoiding local minimums and finding the global minimum on training data can cause overfitting. In many real world problems, selecting the best model is a process of trial and error with cross validation.

Neural networks are similar to trees in that they can perform well on high dimensional datasets. In order to reduce the computational power required, large datasets are often separated into subsets known as “batches”. The network is said to have completed an epoch once it finishes all batches in the dataset it. In many cases, the neural network will perform better if it runs multiple epochs.

#### [2.6.2 Applications of Data Science in Materials Science.](#)

Recently, data science has begun to have a larger impact in the field of materials science as the amount of data produced continues to increase along with more effective methods of using that data (Bock et al. 2019). Machine learning is now being applied to the fabrication of new materials, by predicting material properties given some set of process inputs and then optimizing for the desired properties (Picklum and Beetz 2019). Other applications include image analysis such as for grain boundaries (Homer et al. 2019) or tomographic properties (Altschuh et al. 2017). Machine learning techniques have also been employed for prediction of material properties such as hardness (Oh and Ki 2019) or for simulations of mechanical properties (Reimann et al. 2019)

## Chapter 3: Microstructure and Mechanical Properties of Extruded 6061 Aluminum and Cold-sprayed 6061 Aluminum Alloys

### 3.1 Microstructure of Aluminum – Magnesium - Silicon Alloy 6061

#### 3.1.1 6061 Aluminum Alloy Plate

The wrought 6061 aluminum alloy chosen as a reference material for this work meets ASTM Specification B209M – 14 and consisted of 12.7 mm thick extruded plate. Some work was also done on annealed 6061 plate of unknown original dimensions. Samples were sectioned with a water-cooled SiC blade, ground with water cooling, and polished to a final finish with 0.05  $\mu\text{m}$   $\text{AlO}_2$  or colloidal silica depending upon the particular sample.

Table 16: Composition of 6061 aluminum alloy plate used in this work as reported by the manufacturer

Chemical Composition 6061-T6 Aluminum Alloy Plate									
Main Alloying Elements									Others (each 0.05)
Al	Mg	Si	Fe	Cu	Cr	Mn	Zn	Ti	Total
97.77	0.88	0.66	0.27	0.21	0.07	0.06	0.06	0.03	0.15

The results of the microstructural work on wrought 6061 largely matched established literature on the subject. However, as with many materials, the exact method of manufacture influences sizes and shapes of features within that material. Figure 56 below matches those in established literature (Hatch, 1984), showing undissolved and precipitated  $\text{Mg}_2\text{Si}$  (dark patches), as well as insoluble  $\text{Fe}_2\text{Si}_2\text{Al}_9$ , or  $(\text{Fe}, \text{Mn}, \text{Cr})_3\text{SiAl}_{12}$ .

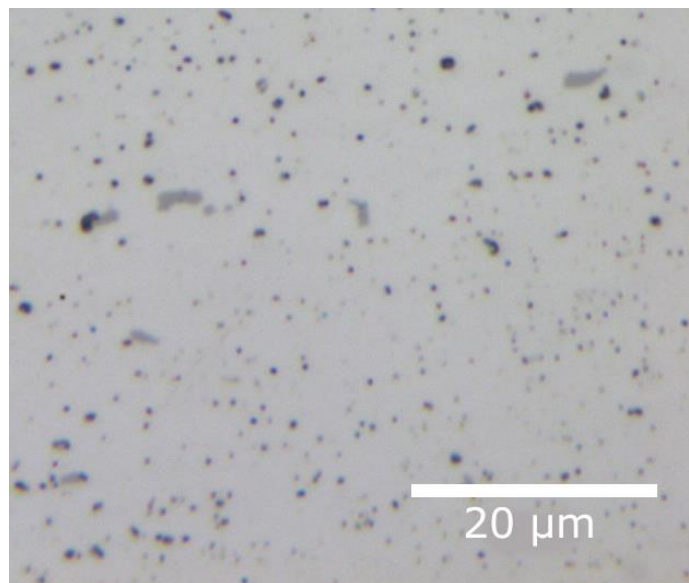
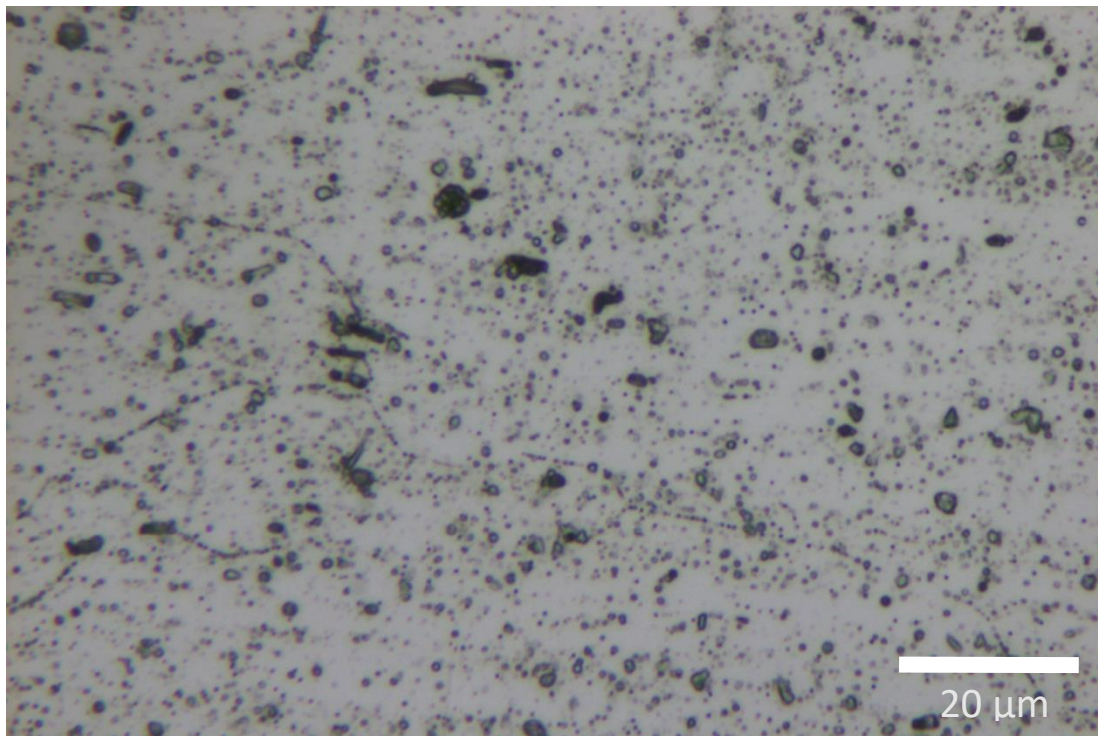


Figure 56: Inverted reflective light microscope color image of 6061-O aluminum (S13) polished with colloidal silica. The image reveals both  $\text{Mg}_2\text{Si}$  and  $\text{Fe}_3\text{SiAl}_{12}$ .

Unetched images of the 6061 plate in T6 condition looked largely identical to the annealed 6061 image above. In Figure 57 below, the light gray background is primarily comprised of FCC Aluminum, while the dark patches are primarily undissolved or precipitated  $Mg_2Si$ . The insoluble  $Fe_3SiAl_{12}$  or  $(Fe, Mn, Cr)_3SiAl_{12}$  has been preferentially etched away leaving pits in the surface. Some evidence of grain boundaries can be seen, but clear grain boundaries are difficult to see due to  $Mg_2Si$  precipitation during the artificial aging process (Hatch 1984).



*Figure 57: Inverted reflective light microscope color image of 6061-T6 aluminum (S11) etched for 55s using Keller's Reagent. This sample is a cross-section of the extrusion direction in extruded plate.*

Figure 58 below show grains typically measuring from approximately  $7\ \mu m$  to around  $60\ \mu m$ , though it is possible to find grains above or below that range. Grains measured in other cross sections of the aluminum plate were more difficult to distinguish, but could be as large as a few hundred  $\mu m$ .

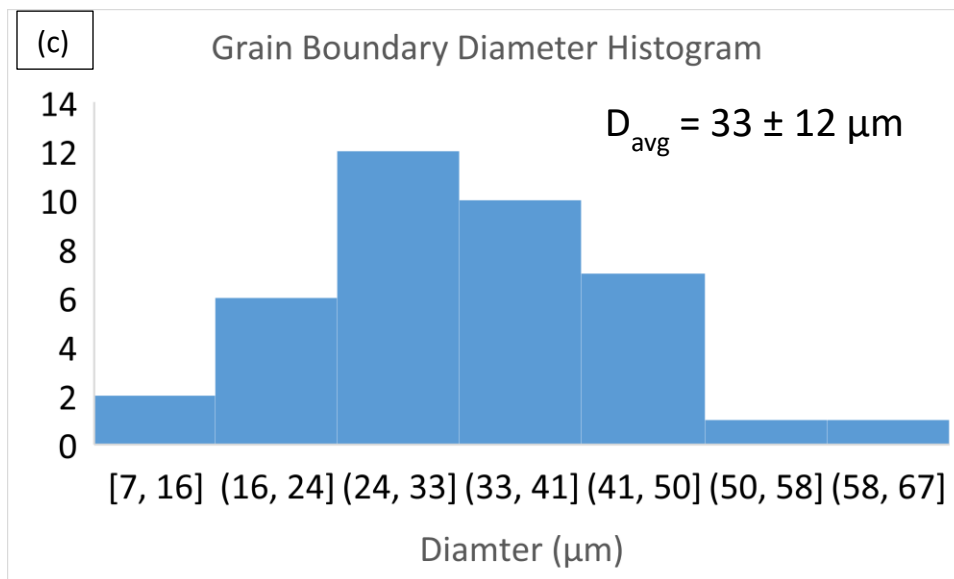
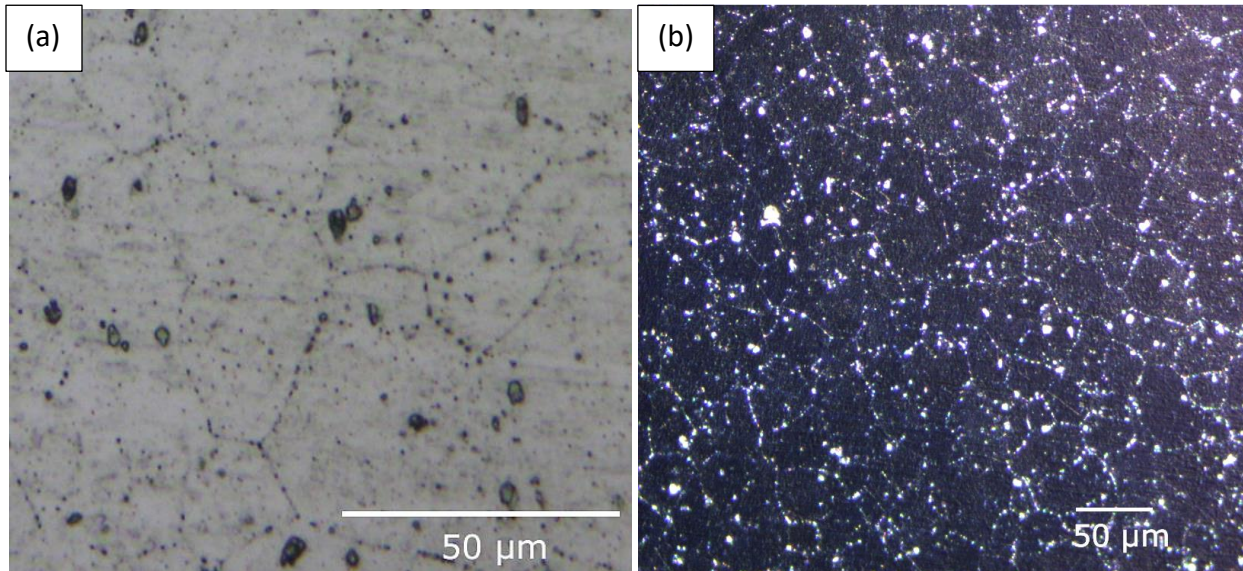


Figure 58: 6061-T6 aluminum (S8) top of plate section- etched with Keller's Reagent for 55s using a visual light microscope (a), with a polarizing filter (b). Below the images is a histogram of the grain diameters seen (c)

EDS spectrums were read at various points (shown in Figure 60 below) on the substrate surface to verify suspicions on the compositions of different surface features. It is important to note that the interaction volume for EDS (from characteristic X-rays) is much larger than that for the secondary electrons that make up a SEM topographic image. Using Monte Carlo simulations for electron behavior in aluminum, the width of the interaction zone for characteristic x-rays is likely around 2-3  $\mu\text{m}$ . The end takeaway is that the results for a small point may actually be averaged with the material surrounding that point.

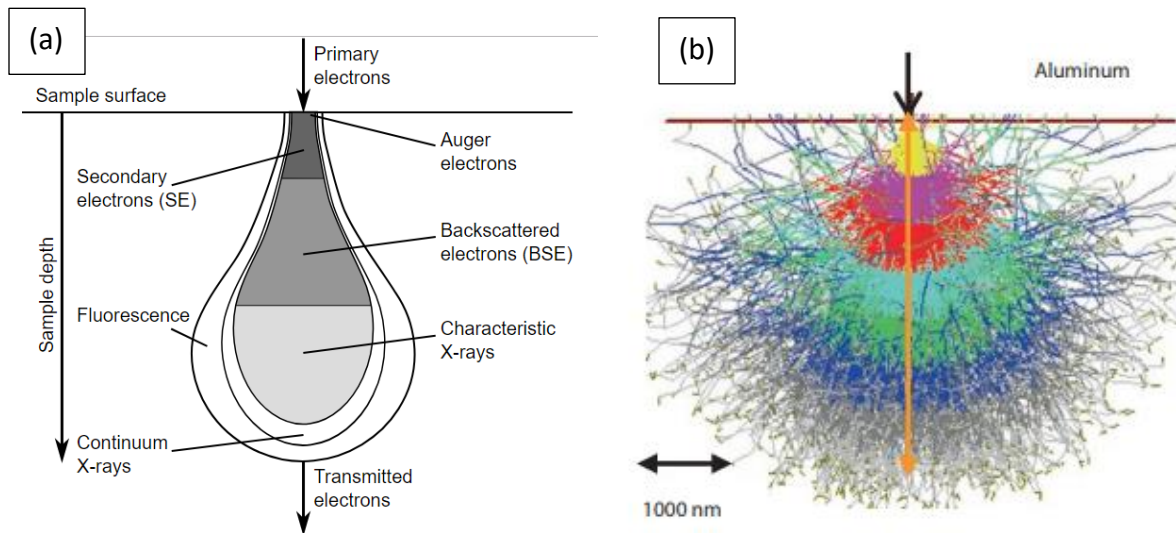


Figure 59: Electron interaction volume for different datatypes (a) (Hansdereber 2015) and a Monte Carlo simulation of electron interactions in aluminum at a 20 kV acceleration voltage (b) (Goldstein 2017)

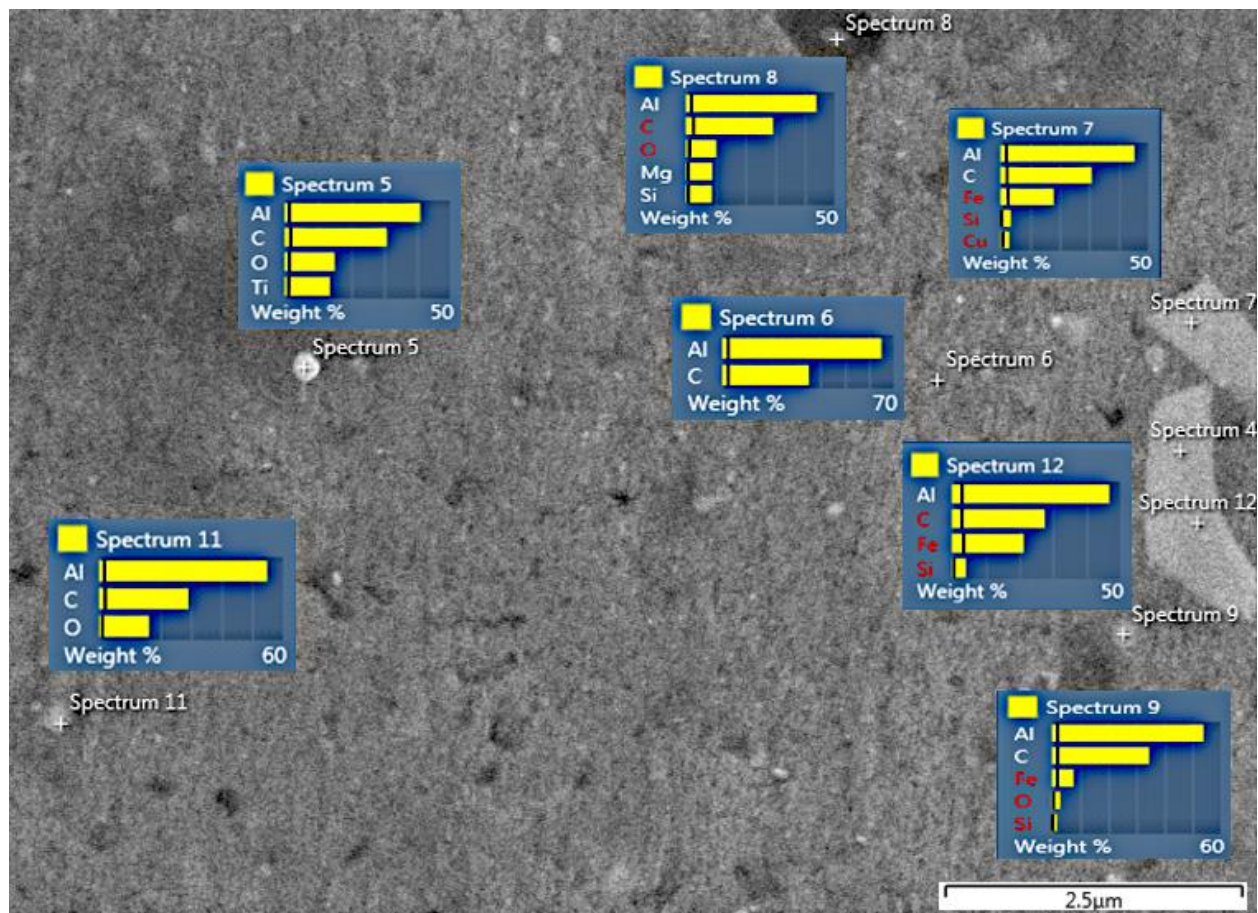


Figure 60: SEM image with EDS inserts on 6061-O aluminum (S2) polished with AlO<sub>2</sub> and unetched.

One of the interesting takeaways from Figure 60 is the detection of other materials known to be contained in the alloy, but preferentially etched away in the other results. Here,  $Mg_2Si$  precipitates were detected as well as inclusions with  $Fe_3SiAl_{12}$  and a phase containing titanium. Figure 61 below has been etched and provides clearer definition of the features in the alloy, but much of the secondary phases in the material have been removed in the etching process.

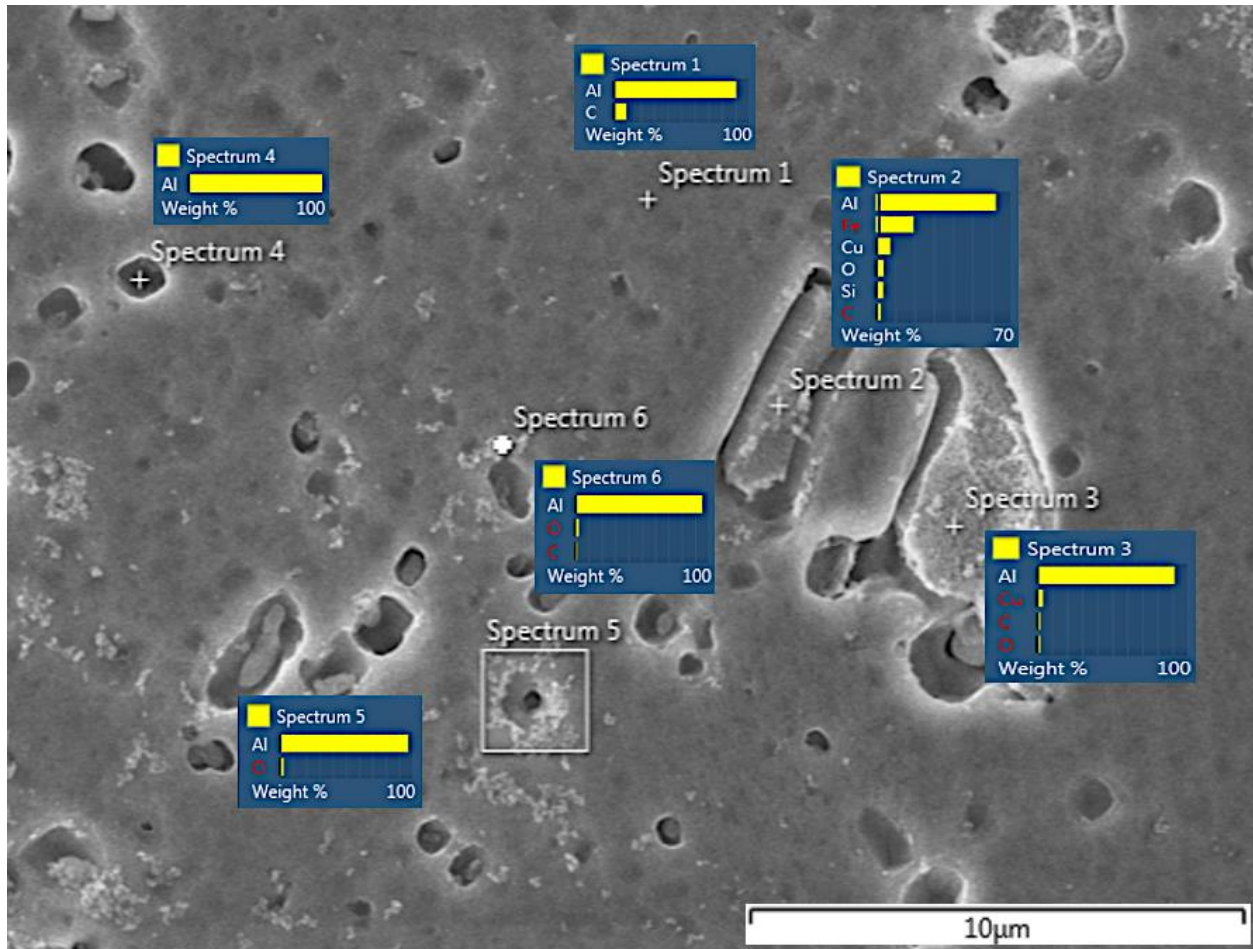


Figure 61: SEM topographic image with EDS inserts identifying existing elements at specific points. This sample was polished with  $AlO_2$  and etched with Keller's reagent.  $AlO_2$  polishing agent appears to have gotten stuck on the surface at some locations such as Spectrum 5.

Spectrum 1 is at a point with fcc aluminum structure which is why the EDS primarily detects aluminum. The detected carbon could be trace carbon in the aluminum, carbon contamination from the environment or a false reading from the EDS software. Spectrum 2 on the other hand was taken at a point in an inclusion which contains expected alloying elements such as copper, iron, and silicon. Oxygen detection may indicate oxide build-up at that point or trapped  $AlO_2$  polishing agent. Spectrum 6 measures primarily aluminum and oxygen suggesting the presence of built up oxides.

### 3.1.2 6061 Aluminum Alloy Powder

The 6061 aluminum alloy cold spray powder has a similar chemical composition to that of bulk wrought 6061. However, the atomization process used to make the powders produces different external and microstructures from the bulk material. The powder particles themselves are roughly spherical in shape and vary in size, but are generally some tens of micrometers with an average diameter of 29  $\mu\text{m}$  (standard deviation of 11  $\mu\text{m}$ ) for the particles measured in this study. ImageJ analysis of SEM images of the powder was used with a contrast thresholding technique to find the area of the particles in the image. Particles below 6  $\mu\text{m}$  in diameter were excluded from the analysis. The particles were assumed to be roughly circular and therefore the diameter could be determined from the areas in the ImageJ analysis.

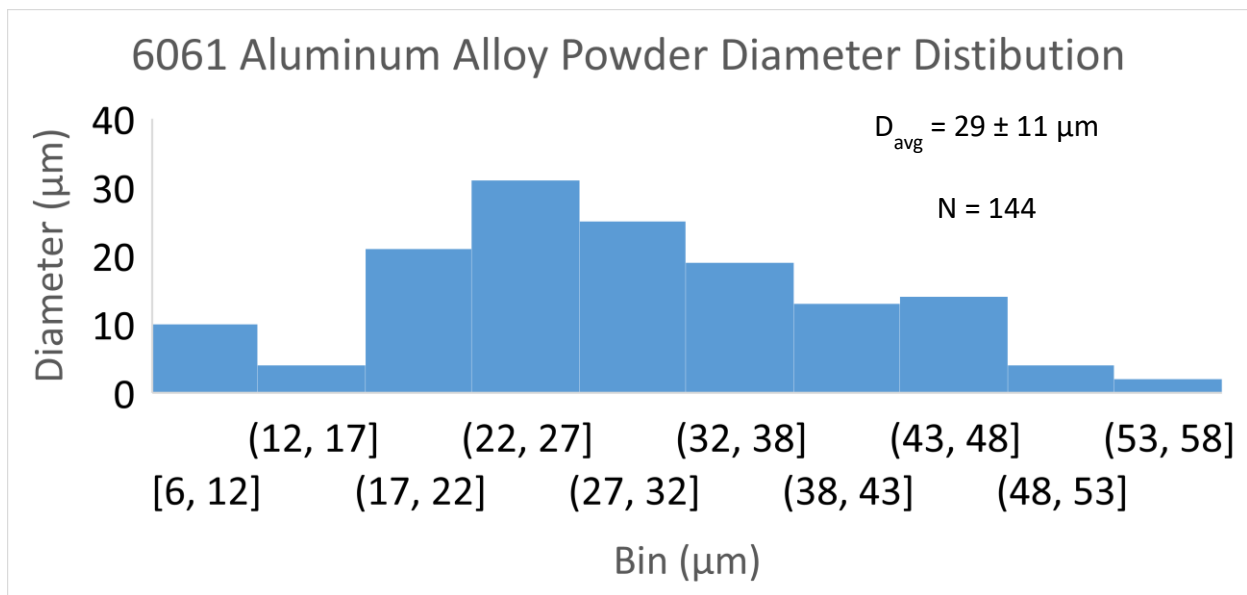
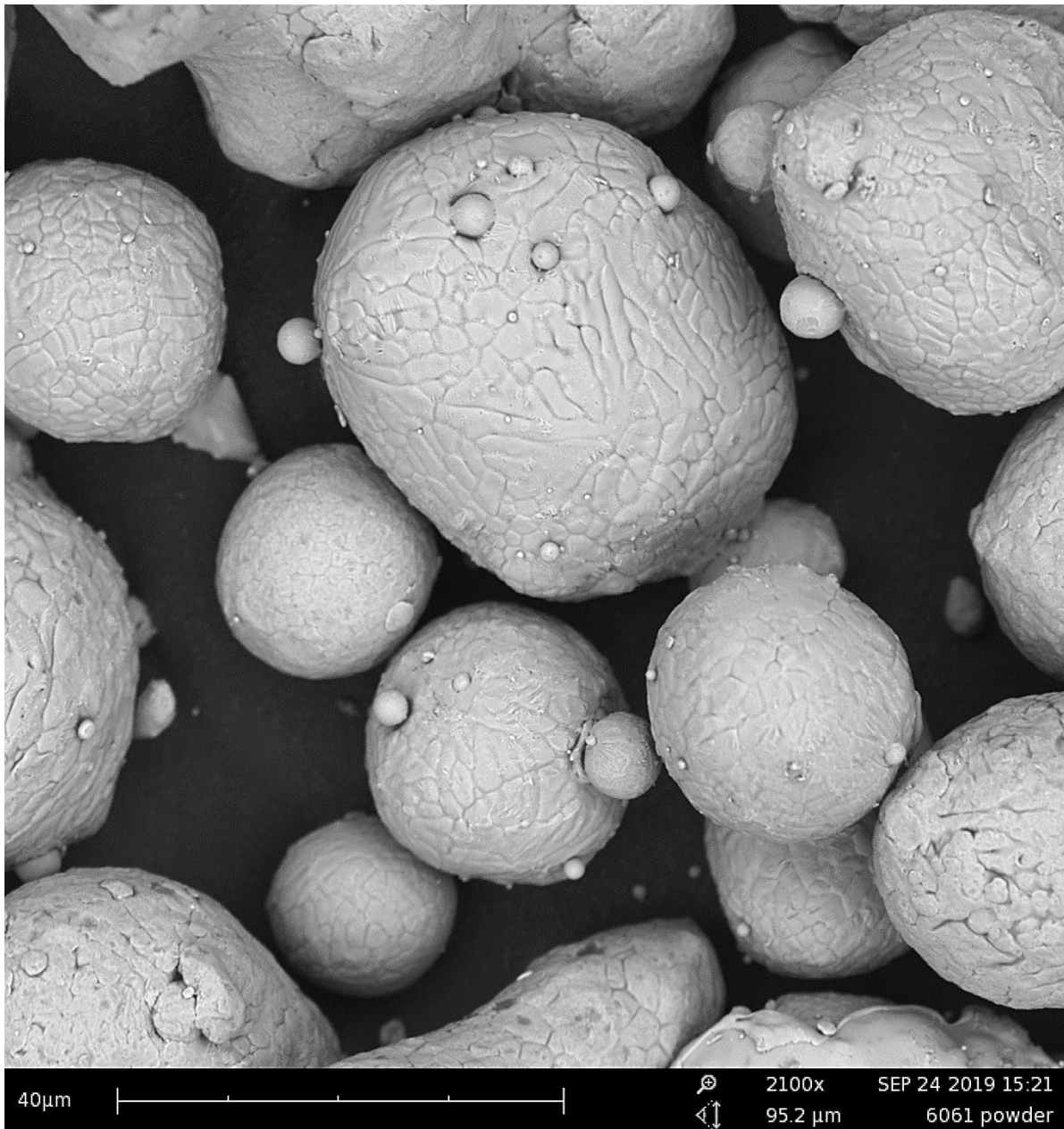


Figure 62: Particle size distribution of gas-atomized 6061 powders

External surfaces of the powder are rough with a cellular structure.



*Figure 63: Gas atomized 6061 aluminum alloy powder showing size and shape of powders as well as cellular structures on the surface of the powders*

As can be seen in the cross-section of the powders below, the precipitates are significantly smaller than in the bulk material and the average grain size is only around 5 µm. The grain sizes observed in the powders for our work were on the order of a few micrometers in comparison with the bulk grain size ranging from tens of micrometers to a few hundred micrometers. The grains appear to be primarily equiaxed and precipitates are clearly seen along the grain boundaries without etching the samples.

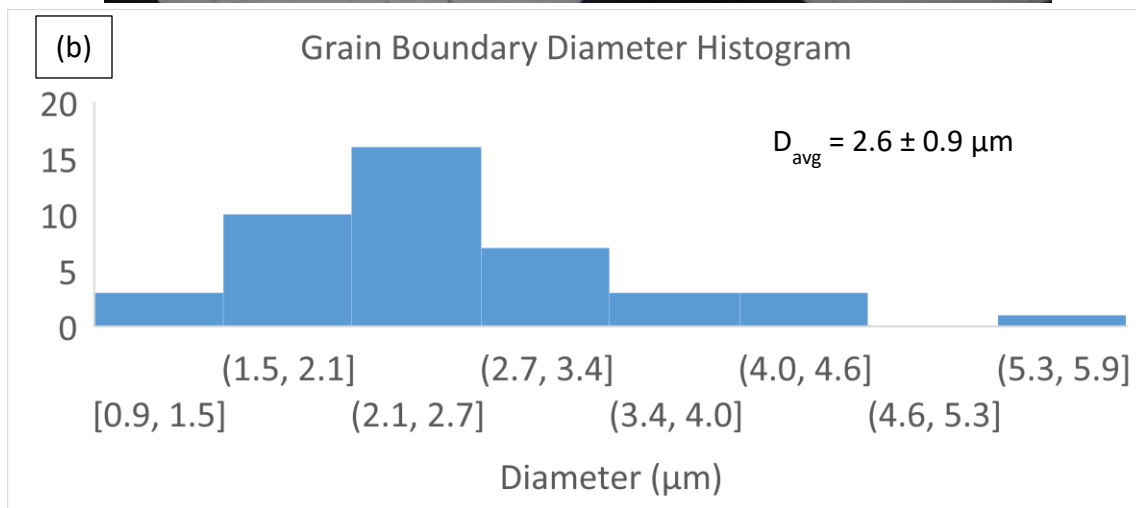
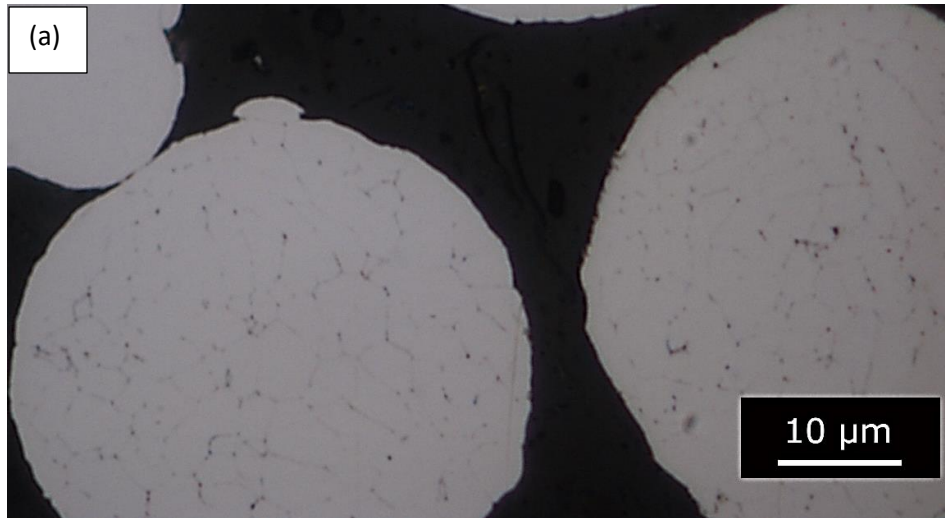


Figure 64: Inverted light microscope dark-field image of 6061 aluminum alloy powders (P1) mounted in a phenolic epoxy and polished with colloidal silica (a). Histogram of grain boundary diameters within the powder (b)

### 3.2 Stress-Strain Behavior of 6061 Aluminum Alloy

In order to test samples within the dimensional constraints of the cold spray deposit, smaller tensile bars were developed. The relative geometry of the tensile bars was kept similar to that defined in ASTM E8-16a, though minor modifications were made to the sizes in order to keep the bars from slipping in the test jaws (see Figure 65).

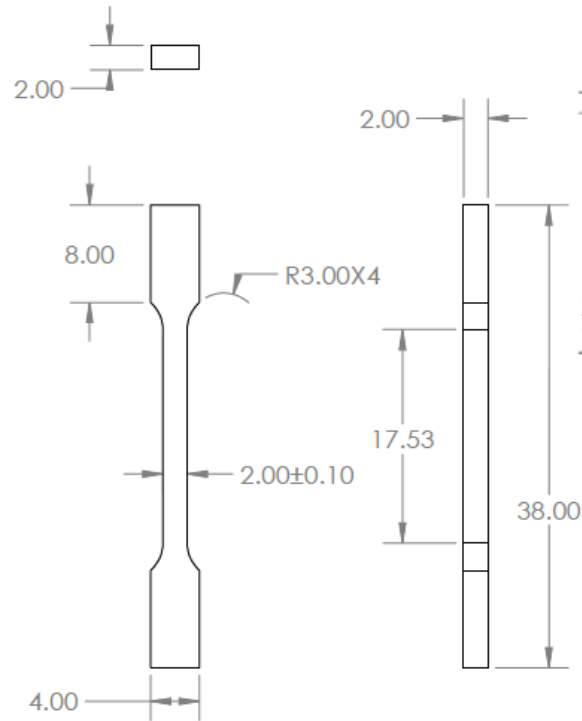


Figure 65: 6061 aluminum alloy tensile specimen dimensions in mm

A clip on strain gage was used in conjunction with an Instron 5kN load cell to measure load and strain. Stress was calculated based off the instantaneous cross-sectional area as estimated using the Poisson's ratio. A strain rate calculated based off of crosshead speed on the tensile tester of  $4 \times 10^{-4} \text{ s}^{-1}$  was used in the testing. As can be seen in Figure 66 below, 6061 exhibits power law strain hardening. The samples also experienced significant necking which made the measured ultimate tensile strength values different from reality.

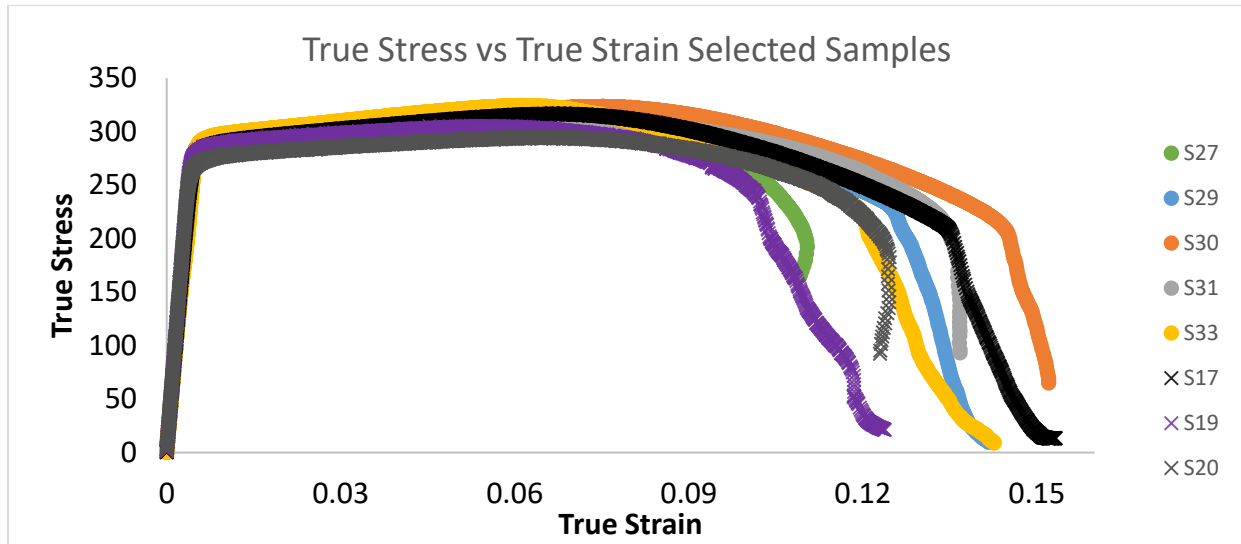


Figure 66: 6061-T6 aluminum wrought plate true stress versus true strain.

The Ramberg-Osgood relation (equation 32; which is a re-written form of the original by Ramberg and Osgood 1943) was used to provide a fit of the stress strain curves found during the tensile tests. The relationship is a simple addition a linear representation of the elastic portion of the stress-strain curve and a logarithmic representation of the plastic portion (equation 31). The strengthening coefficient,  $K$ , and the strain hardening coefficient,  $n$ , found in this representation (shown by Gadamchetty et al. 2016) can be used as an input into simulations to provide a relatively accurate representation of stress-strain behavior.

$$\varepsilon_t = \varepsilon_e + \varepsilon_p \quad (31)$$

$$\varepsilon_t = \frac{\sigma}{E} + \left(\frac{\sigma}{K}\right)^{\frac{1}{n}} \quad (32)$$

The Ramberg-Osgood strain hardening and strengthening coefficients were found by using the Hollomon strain hardening equation (Hollomon 1945) and a log-log plot of stress and strain as in Figure 67.

$$\sigma = K\varepsilon_p^n \quad (33)$$

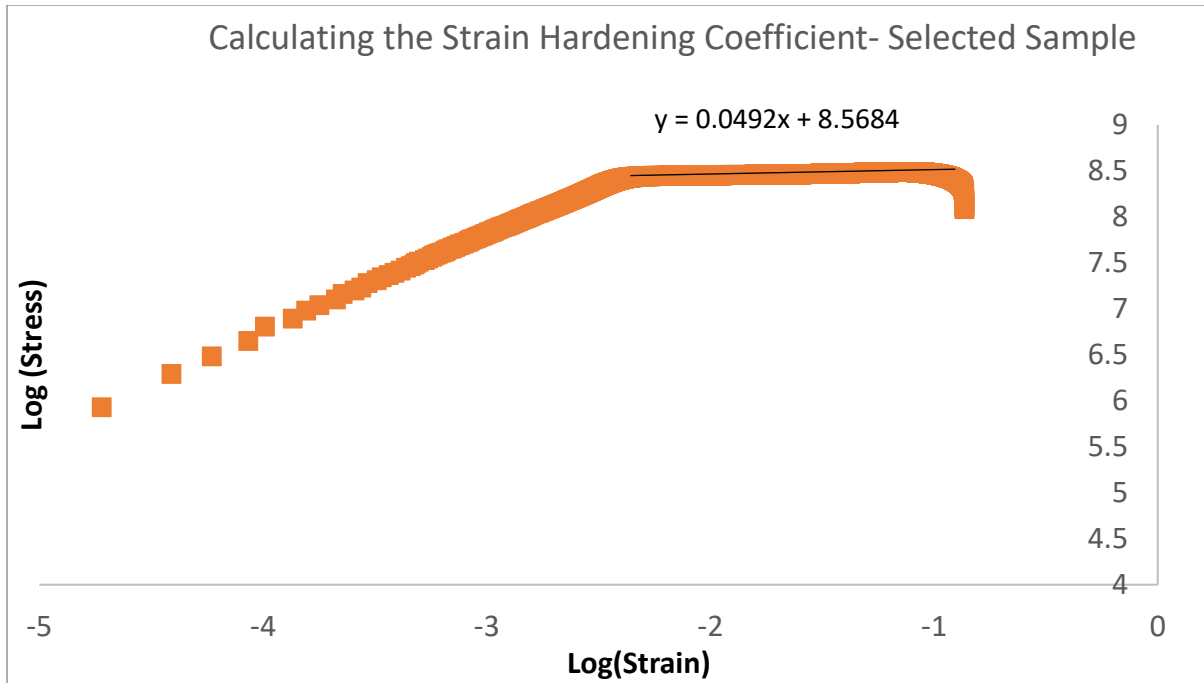


Figure 67: Methodology for finding Ramberg-Osgood parameters using a linear fit of the log-log stress strain curve within the plastic zone

The Hollomon parameters were also found using the logarithmic form of resultant data between the 0.2% strain yield point and the ultimate tensile strength. However, this representation incorporated some non-logarithmic aspects of the true data and therefore produced a less accurate fit than the graphical method shown above.

$$n = \frac{\log\left(\frac{\sigma_{uts}}{\sigma_y}\right)}{\log\left(\frac{\epsilon_{uts}}{\epsilon_y}\right)} \quad (34)$$

Differences were seen in the mechanical properties of the lateral and longitudinal samples. Figure 68 below demonstrates the differences in idealized Ramberg-Osgood curves for each direction. Each curve is built from the average values found experimentally in each direction. The Ramberg-Osgood representation also gives the theoretical ultimate tensile strength given different maximum strains. It can be seen that the Ramberg-Osgood representation of the stress-strain data is fairly accurate to the true measured data. However, the true sample experienced necking around 7% strain, which resulted in non-physical measured drop in stress. In reality, if the reduced cross-sectional area of the tensile bar due to necking is accurately accounted for, the stress would continue to increase until failure. This plot would in turn be more similar to that predicted by the Ramberg-Osgood relationship. An attempt was made to

account for the actual cross-section during the necking phase using caliper measurements, but the necking profile was nonuniform and accurate results could not be reliably obtained.

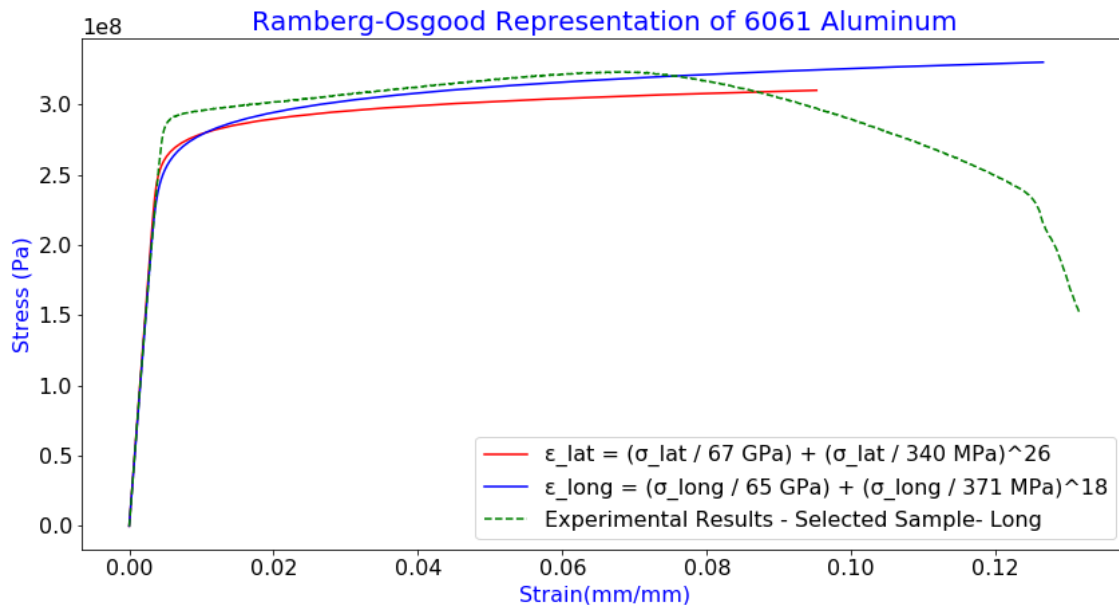


Figure 68: Ramberg-Osgood representations of lateral and longitudinal samples compared with the raw true stress-strain curve from a longitudinal sample of 6061-T6 aluminum alloy<sup>2</sup>

Finally, Table 17 and Table 18 below provide a summary of the mechanical properties found as well as a comparison with material certifications provided by the manufacturer and values found in the literature. The longitudinal samples (in the extrusion direction) typically had better mechanical properties in comparison with the lateral samples (perpendicular to the extrusion direction). Different representations of the Ramberg-Osgood equation have been developed and the method is heavily dependent upon the choice of the start and stop of the plasticity curve. The R-squared value of the predicted strain and the true strain up until the point of maximum measured stress ranged from 0.71 to 0.95 depending on the chosen Ramberg-Osgood model. Figure 68 is showing the representation from the model with an R-squared value of 0.71. As the Ramberg-Osgood equation depends on high order exponentials, the model predictions can rapidly diverge from the true strain values if the fit is not exact. The Holloman strain hardening coefficients from the experimental data contained the coefficient cited in literature within one standard deviation.

<sup>2</sup> A short python program was written to plot and compare the different formulations of the Ramberg-Osgood equation. This has been posted to my github account "snesnehne" and is available for public use

Table 17: 6061-T6 mechanical reference parameters from the material manufacturer, CES Edupack (a), and the ASM Handbook, volume 8 (b)

6061-T6 Aluminum Reference Parameters					
	Manufacturer Certification		Literature (a)		Units
	min	max	min	max	
Yield Strength (0.2% Offset)	291	294	240	280	MPa
Ultimate Tensile Strength	312	317	290	338	MPa
% Elongation	12.1%	12.5%	10%	14.4%	
Ramberg-Osgood Parameters				Typical (b)	
Strain Hardening Coefficient (n)				0.05	
Strengthening Coefficient (K)				410	

Table 18: Summary of 6061-T6 aluminum mechanical properties found during tensile testing

6061-T6 Aluminum Tensile Test Results					
	Lateral		Longitudinal		Units
	Avg	Std	Avg	Std	
Yield Strength (0.2% Offset)	280	6.43	289	4.83	MPa
Ultimate Tensile Strength	306	10.72	317	6.86	MPa
% Elongation	12%	2%	13%	1%	
Ramberg-Osgood Parameters					
Strain Hardening Coefficient (n)	0.039	0.01	0.060	0.02	
Strengthening Coefficient (K)	340	17	371	22	MPa
Ramberg-Osgood Parameter (1/n)	26	5.59	18	5.36	

The 6061-T6 tensile samples were characterized by ductile necking which can be seen in the significant cross-sectional reduction in Figure 69 (a) and the ductile dimples seen in Figure 69 (b).

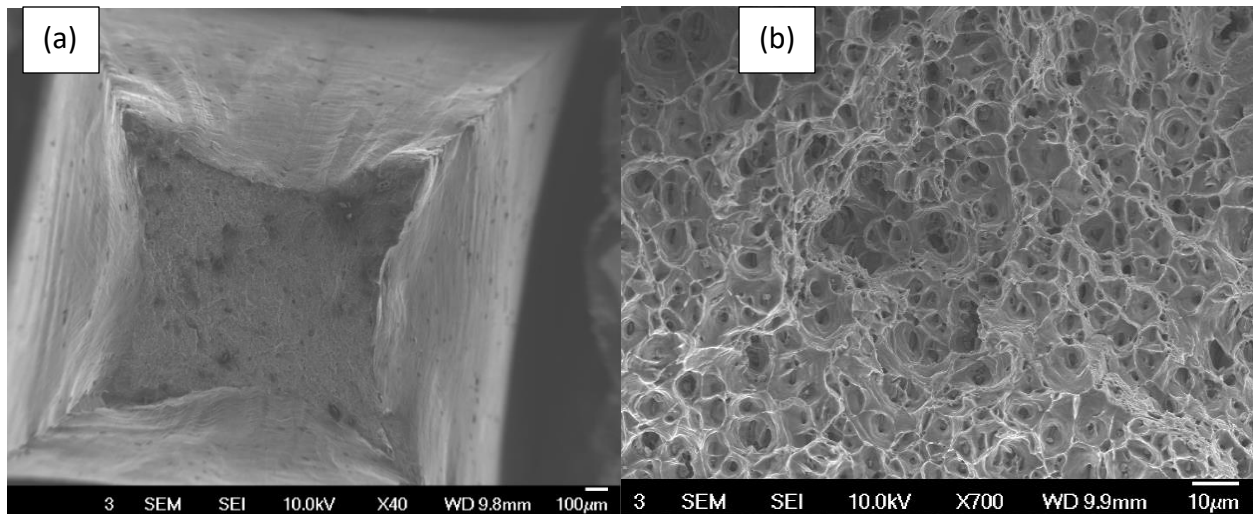


Figure 69: SEM images of a tensile specimen (S17) cross-section after testing show a reduction in cross-sectional area (a) and ductile dimples (b), characteristic of necking

### [3.3 Indentation Size Effect in 6061 Aluminum Alloys](#)

#### [3.3.1 Vickers Microhardness](#)

All substrate samples were prepared by sectioning the material using a water-cooled cutting disk. The samples were then pressed into hot mount epoxy resin, before being ground and polished to a mirror finish using 0.05  $\mu\text{m}$  AlO<sub>2</sub> or colloidal silica particles suspended in water. Sample 6, which was used for the 6061-T6 data was solid aluminum plate and not mounted in epoxy to reduce compliance effects. A Clark CM-400AT microhardness tester with a diamond tip in the Vickers geometry was used with loads from 10 gf (98 mN) to 1000 gf (9806 mN). Vickers hardness values (HV) were converted to SI values based upon the projected area of the indenter and the load in N. Projected area was used rather than the surface area (as used for the standard Vickers hardness) so that the hardness values could be accurately compared with values from other tip geometries. Some uncertainty in the hardness values is born from the optical measurement system. Different users will also make different hardness measurements based upon their decision on the precise border of the indents. In this case however, the user was the same for all indents. An important consideration is that residual stresses from the act of polishing may contribute to differences in hardness measured at different depths, although care was taken during the polishing process to prevent this. Other variation in the measurements stems from anisotropy within the material at these measurement scales.

The 6061-O substrate showed a strong dependence of hardness on depth, before becoming asymptotic.

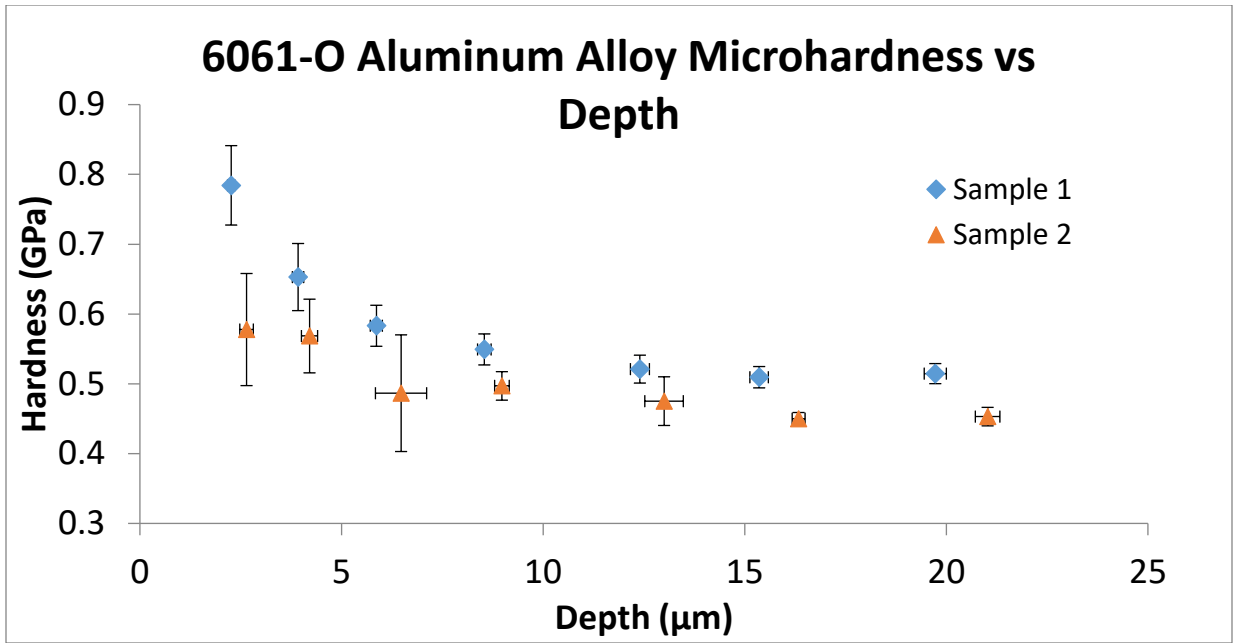


Figure 70: Hardness versus depth in two samples of annealed 6061 aluminum alloy

The 6061 sample in the T6 condition had significantly more variability in the measured hardness values and a less pronounced indentation size effect.

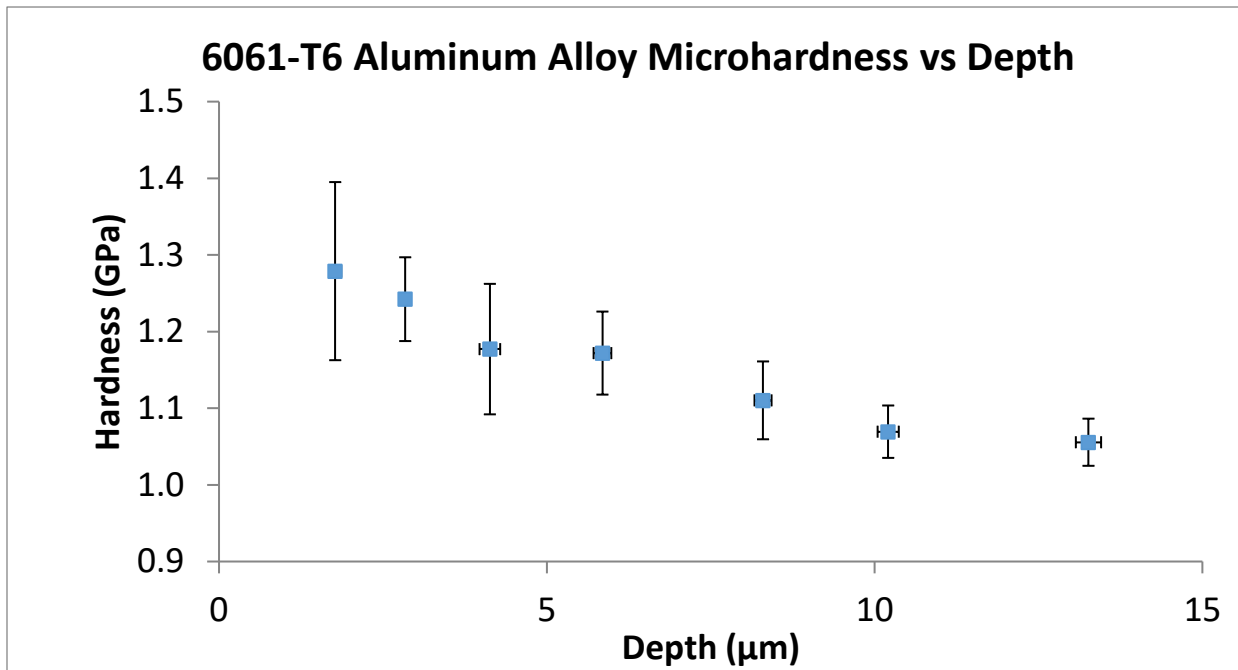


Figure 71: Hardness versus depth in 6061-T6 aluminum plate of indents on the top face of the plate

The hardness values for a particular load had higher scatter than those found by other researchers for pure aluminum. The scatter increases as the load decreases and an individual

hardness value is often impacted by material inconsistencies such as second phases, voids, and inclusions. Larger loads sample a larger area which averages out the local effects with cause greater variation for the lower loads.

By plotting the square of the hardness values against the inverse of the indentation depth a linear relationship a line of best fit can be drawn and used to find the intercept. The square root of the hardness intercept is equal to the hardness due to statistically stored dislocations, which for the 6061-O aluminum results in an  $H_0$  of 0.44 GPa. The methodology for the 6061-T6 sample and titanium samples is identical to that used for 6061-O aluminum so the results are simply listed in a table at the end of each section.

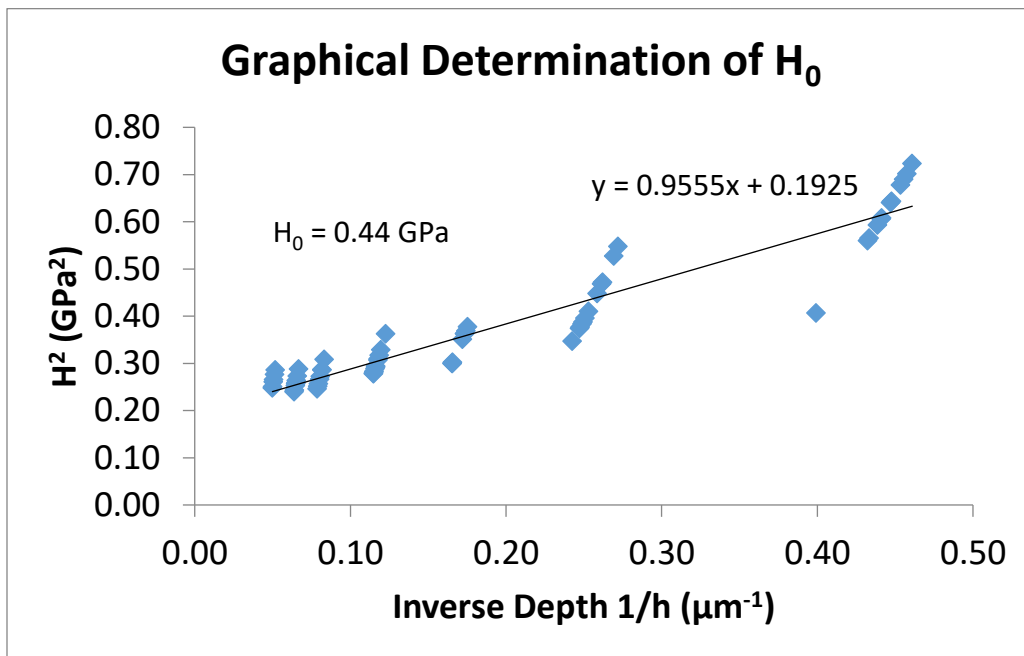


Figure 72: Plot of  $H^2$  to  $1/h$  used to find the value of  $H_0$  for 6061-O aluminum

Similarly the characteristic length of depth dependence of hardness,  $h^*$ , was found from the slope of Figure 73 below to be 4.96  $\mu\text{m}$ .

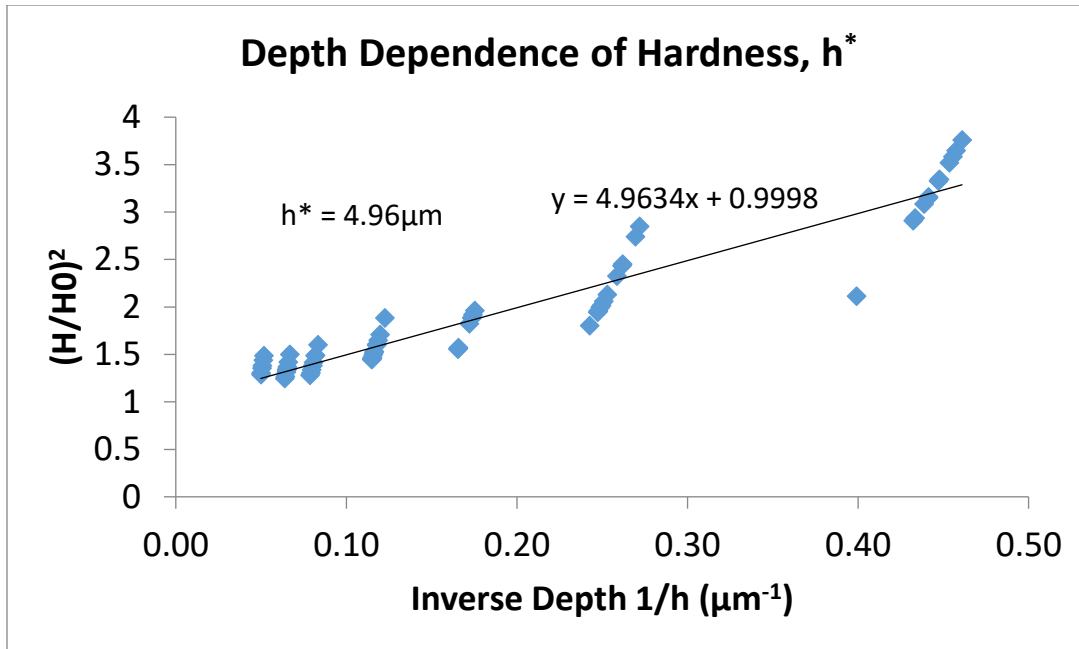


Figure 73: Linearized plot of hardness and indentation depth for 6061-O aluminum alloy

The density of statistically stored dislocations can be calculated using the expected shear modulus and burgers vector for the material along with the  $H_0$  value found from the experimental data above.

$$\rho_s = \left( \frac{H_0}{3\sqrt{3}\alpha\mu b} \right)^2 \quad (35)$$

The density of statistically stored dislocations ( $5.1 \cdot 10^{14} \text{ m}^{-1}$  for the annealed condition and  $3.3 \cdot 10^{15} \text{ m}^{-1}$  for the T6 condition) was then used to predict the material length scales seen below. Annealed sections of 6061 aluminum alloy showed a higher ISE as evidenced by the larger  $h^*$  values, while the strain gradient plasticity length scale in the T6 samples was significantly lower. This is logical given the higher number of statistically stored dislocations in the T6 plate. Similar differences have been reported for annealed copper compared with cold worked copper, in work done by Ma and Clark in 1995.

Table 19: Summary of material parameters found by applying Nix and Gao's methods to Vickers microindentation of 6061 aluminum alloys

Material	Measured from Projected Area Microhardness Data		
	$H_0$ (GPa)	$h^*$ ( $\mu\text{m}$ )	$l$ ( $\mu\text{m}$ )
6061-O Al Sample 1	0.44	4.96	9.05
6061-O Al Sample 2	0.41	3.20	10.43
6061-T6 Al Extrusion Direction	1.11	0.65	1.40

### 3.3.2 Simulation of Low Load Nanoindentation with an Imperfect Berkovich Tip

FEA simulation in Abaqus software was used to get a better understanding of the stresses and approximate sizes of stress fields for a Berkovich indenter into a 6061-T6 aluminum alloy. Another purpose of the model was to predict pileup during the indent. Elastic and plastic material properties were incorporated into the model. In this simulation, materials properties values for the 6061 aluminum were taken to be the middle of the range from the values in CES Edupack. Stress strain data from (Weaver et al.) was used to incorporate plasticity into the model. The diamond Berkovich tip was modeled as a rigid body with a 100 nm tip radius (corresponding to a dull, used tip with even wear). The indent was displacement controlled at a linear rate to a depth of 200 nm, which is within the depth range we observed in our physical experiments.

Convergence of the simulation was a significant challenge during the development process due to excessive local deformation. The simulation shown here was able to successfully solve using implicit dynamic analysis with the nonlinear geometry solution activated on Lagrangian finite elements. In future work, Euleran elements may be used to account for larger local deformation at greater indent depths. Hexagonal elements were solved using linear, reduced integration with 8 nodes per element.

The 6061-T6 substrate was assumed to be homogenous and isotropic. In reality the local microstructure of the aluminum can have a significant effect on the properties observed for a particular indent. The model also assumes continuum mechanics, which do not provide a perfect fit with the true behavior at this small scale.

However, the model can still provide some interesting insights. For example, the FEA simulation provides evidence that it may be reasonable to model the indent as a combination of ideal Berkovich geometry and spherical geometry for the section with a rounded tip. The transition of the stress field from the rounded tip to the pyramidal geometry can clearly be seen in Figure 75 below.

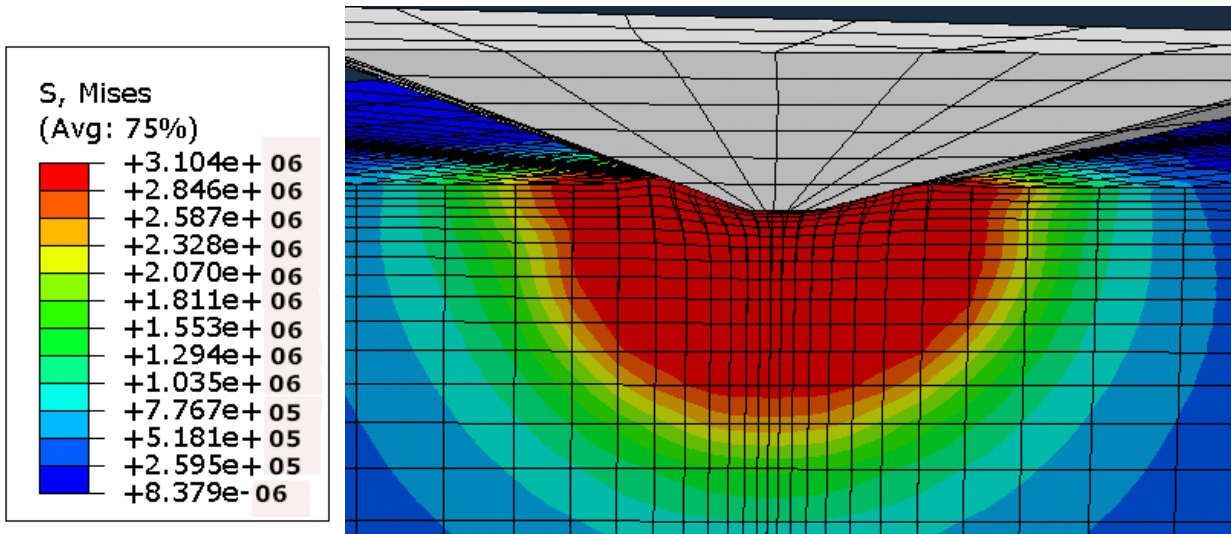


Figure 74: Cut-away of 3D Von Mises stress plot showing multiple stress profiles<sup>3</sup>

Pileup can also be seen around the indenter tip when plotting the displacement in the z direction. By plotting the z displacement along a path across the indent we can make a measurement of pileup similar to that done for the AFM images in the experimental data. The simulation predicts significant pileup of around 60 nm at the highest points, which can be used to correct the harnesses found during experimental measurements.

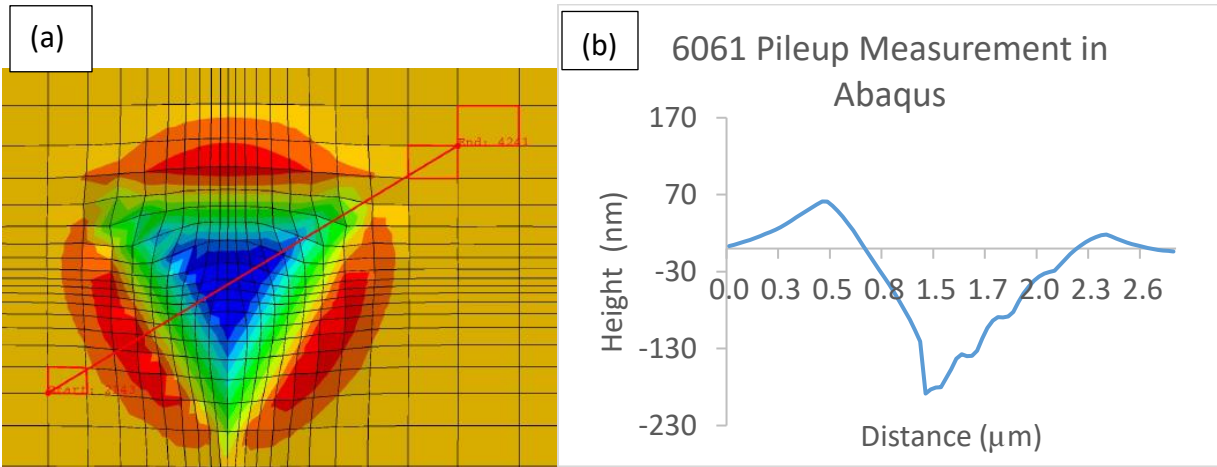


Figure 75: 3D plot of vertical displacement in vertical direction (a) and along path marked on plot (b)

Given that the depth of the indent is 200 nm and the yield stress of 6061-T6 aluminum alloy to be 298 MPa, the plastic zone is approximately 3000 nm. This actually is close to the spacing between indents recommended by Phani and Oliver (2019), so as not to have significant effects of indents on the measurements of neighboring indents. The relationship Phani and Oliver derived is that indent spacing,  $d$ , should be  $d/h \geq 10$  where  $h$  is the depth of the indent.

<sup>3</sup> Simulation name "Berk 24-6061-Exp\_s\_Str/Job-1-2-disp.odb"

However, the spacing suggested by the results of this 6061 simulation would suggest a spacing of  $d/h \geq 15$  to avoid any plastic zones overlapping between indents.

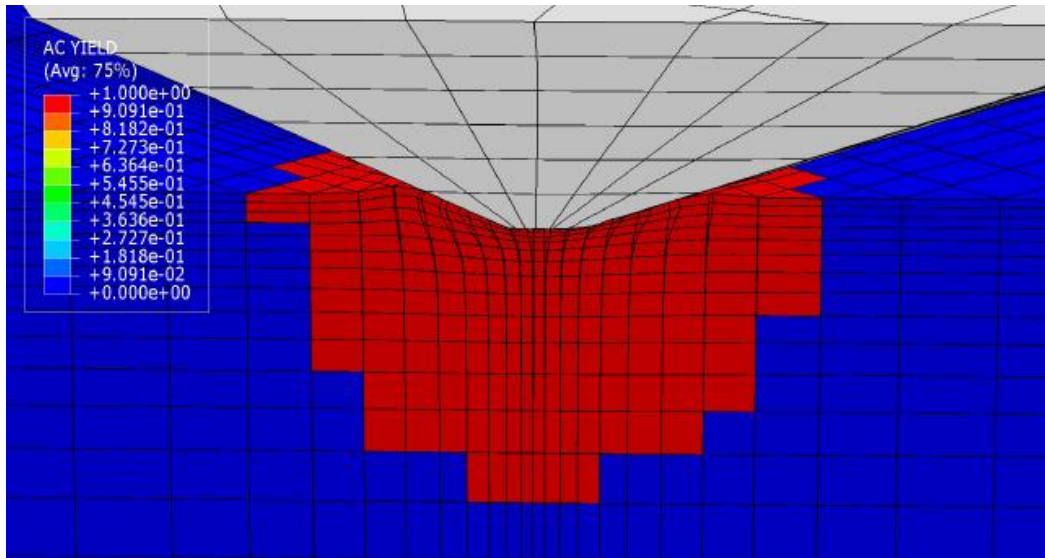
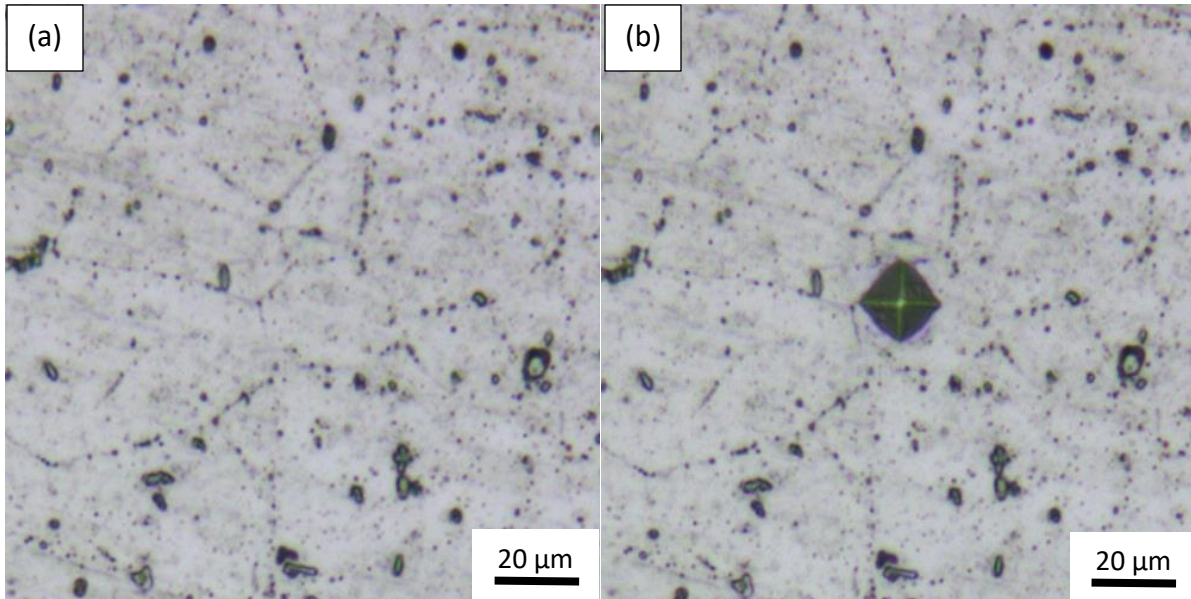


Figure 76: Zone of yielded material with criteria that 75% of the element exceed the yield strength

This model can be used for predictions of material response to loading with a realistic Berkovich tip. The model could easily be adapted for other metallic materials by changing the elastic and plastic material parameters in the model. Additionally, the model contacts can be used for other realistically worn indenter tips such as Vickers tips.

### [3.4 Prediction of Hardness Using Machine Learning and Microstructural Images](#)

The goal of this section of the work was to determine if machine learning could be used to predict variation in alloy hardness based upon features seen on the surface of a material. A successful algorithm would be able to accurately predict the hardness of the material at different locations simply using images of the material surface. In our work, etched 6061 aluminum alloy samples were imaged before and after indentation. Ideally a machine learning algorithm would incorporate features of the alloy seen in images such as grain boundaries to predict the hardness that is likely to be measured in that area. For example, an indent location within a smaller grain boundary or closer to the edge of a grain boundary may have a higher indentation due to dislocation pileup.



*Figure 77: Etched surface of 6061 aluminum samples before (a) and after indentation (b)*

The model used in this work was based upon an autoencoder with an encoder and decoder portion. Autoencoders are often useful for making predictions with high dimensionality data (such as images), but a low number of samples. In this case, the model was run on a set of 40 after-indent images as well as hardness values for each image. After-indent images are known to contain features which can predict the material hardness (i.e. the size of the indent in the image). Therefore, the after images were used as a base case to test the effectiveness of the model. If the model could not make accurate predictions based when it has information about the size of the indent, it is unlikely to be successful for the more challenging case without the size of the indent. A custom dataset was made in Pytorch from this data. The images were scaled and converted to tensors for used within Pytorch. The autoencoder model compresses using a series of linear and hyperbolic tangent functions before being decoded in the same manner. The final step uses a sigmoid function for compress the data between zero and one. Figure 78 below shows the tensor input into the model as well as the output tensor of the image from the model. The output images are a good way for humans to tell if the model is not only reducing prediction error, but also returning the important features in the image. As can be seen, the model is starting to return the indent itself, but is unsure of the position for the indent. The model at this point is not effective enough to accurately predict the hardness of that image. Given the small sample size (40), a larger dataset would likely improve the results.

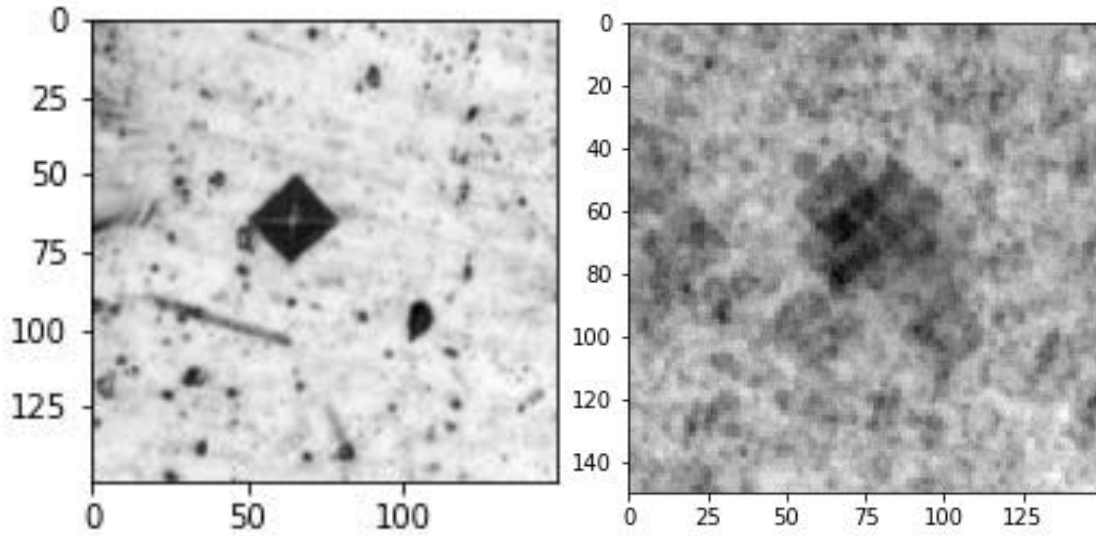


Figure 78: Plot of tensor image input (a) into autoencoder and output (b) of autoencoder

### 3.5 Simulation of Cold Spray 6061 Impact- Effect of Oxide Layer

Much work has been done on cold spray impacts of aluminum on an aluminum substrate. However, the author is not aware of existing FEA models which consider realistic oxide layers of around 5 nm along with a bilinear John-Cook plasticity model. Many models have considered a linear Johnson-Cook (JC) model, when a bilinear model (BJC) is more appropriate at the strain rates experienced during a cold spray impact (Lamiale et al. 2014). The linear JC model shown in equation 26 below is made bilinear by adding a second constant  $C_2$  term to make an approximation of the strain hardening in second higher strain rate domain.

$$\bar{\sigma} = \left[ A + B(\bar{\epsilon}^{pl})^n \right] \left[ 1 + C \ln \left( \frac{\dot{\bar{\epsilon}}^{pl}}{\dot{\bar{\epsilon}}_0} \right) \right] (1 - \hat{\theta}^m). \quad (36)$$

A member of our research group, Vahid Rahneshein (2019), was able to produce a linear JC model, and a custom BJC model without an oxide layer for commercially pure aluminum. My contribution was to add material parameters for 6061 developed by Dehkharghani and Muftu and Manes et al. (2011) in combination with temperature data from Rech et al. (2014) to produce more accurate JC and BJC models for 6061 aluminum alloy. Particle velocity was chosen to be slightly above the reported critical velocity by Schmidt et al. (2006) and then varied above and below to explore the impacts of velocity. A particle diameter of 30  $\mu\text{m}$  was used based off of the average particle size found during our image analysis.

Table 20: Parameters used in 6061 aluminum alloy cold spray particle impact simulation

Spray Properties		Material Properties		Bilinear Johnson-Cook Parameters (Dehkarghani and Muftu)						
Temp.	Particle Velocity	Young's Modulus	Poisson's Ratio	A	B	n	C <sub>1</sub>	C <sub>2</sub>	m	$\dot{\epsilon}_c$
600K	500-900 m/s	68.3 GPa	0.33	270 MPa	154 MPa	0.239	0.002	0.029	1.42	597

Brittle cracking damage criteria were used in the oxide layer of the models. The damage criteria causing element removal in the oxide layer can help to show remaining oxide layer trapped between the particle and substrate which reduces the adhesion strength.

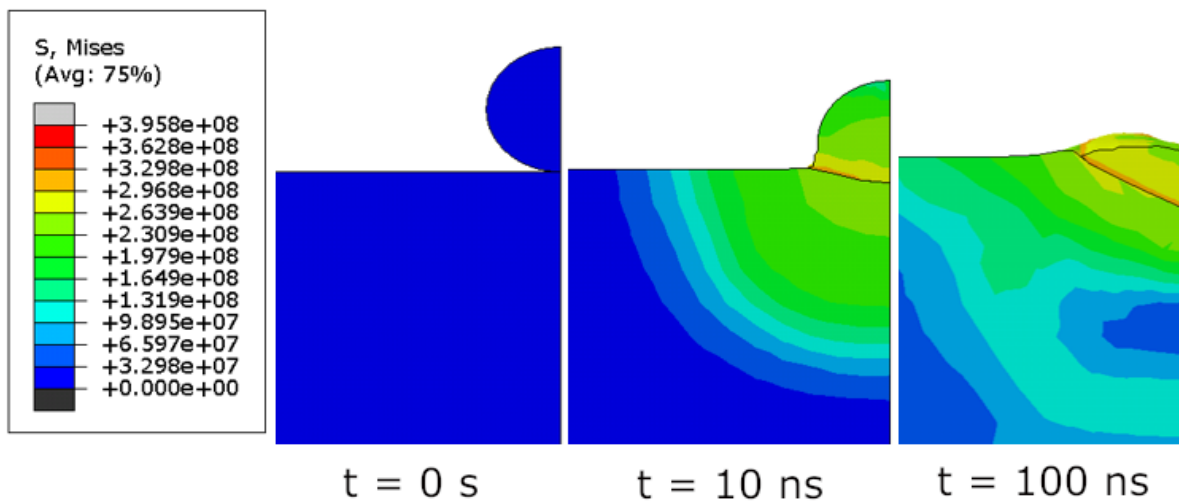


Figure 79: Stress evolution of 6061 aluminum alloy particle impact on 6061 aluminum alloy substrate using Johnson-Cook plasticity mode at velocity of 770 m/s<sup>4</sup>

A linear JC model was also run without the oxide layer for comparison between results. Unsurprisingly, the particle deformed more easily and experienced greater stress without the oxide layer. Contrarily with the inclusion of the oxide layer, the substrate experienced higher stress, while the oxide layer around the particle experienced stress orders of magnitude more than the ductile 6061 aluminum alloy.

<sup>4</sup> Simulation name "Job2-IMP@\_LJC\_NO\_OX\_400K\_SUB"

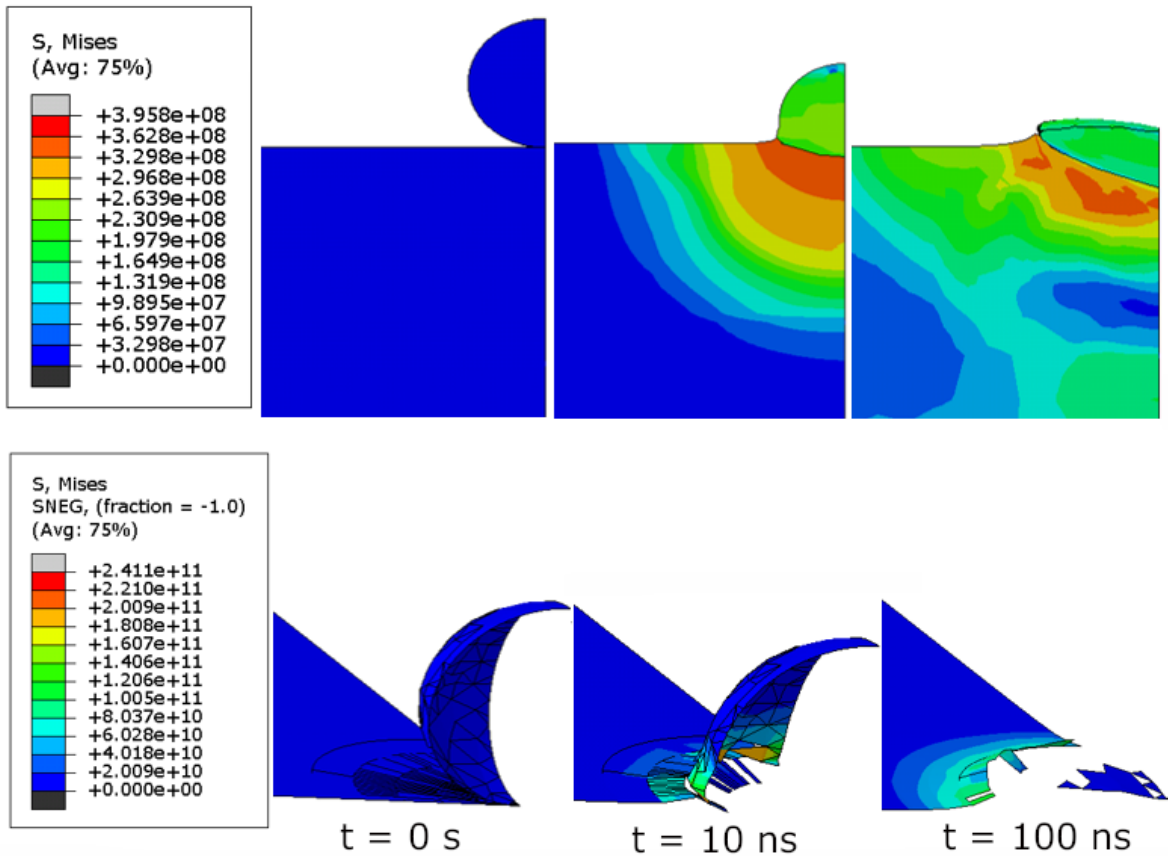


Figure 80: Stress evolution of 6061 aluminum alloy particle impact on 6061 substrate using Johnson-Cook plasticity with 5 nm aluminum oxide layers at 770 m/s<sup>5</sup>

The BJC models clearly show less deformation of the particle during impact as a result of the additional strain hardening at high strain rates. In the JC model a substrate temperature of 400 K was used, while the BJC model required a uniform temperature definition. However, despite a higher substrate temperature of 600 K in the BJC model, the additional strain hardening still reduced the substrate deformation. Note that the scales are different for the JC and BJC stress visualizations so the coloring is different for the same stress levels.

<sup>5</sup> Simulation name "Job-2-IMP1\_LJC\_OX\_400K\_SUB\_600K\_PART"

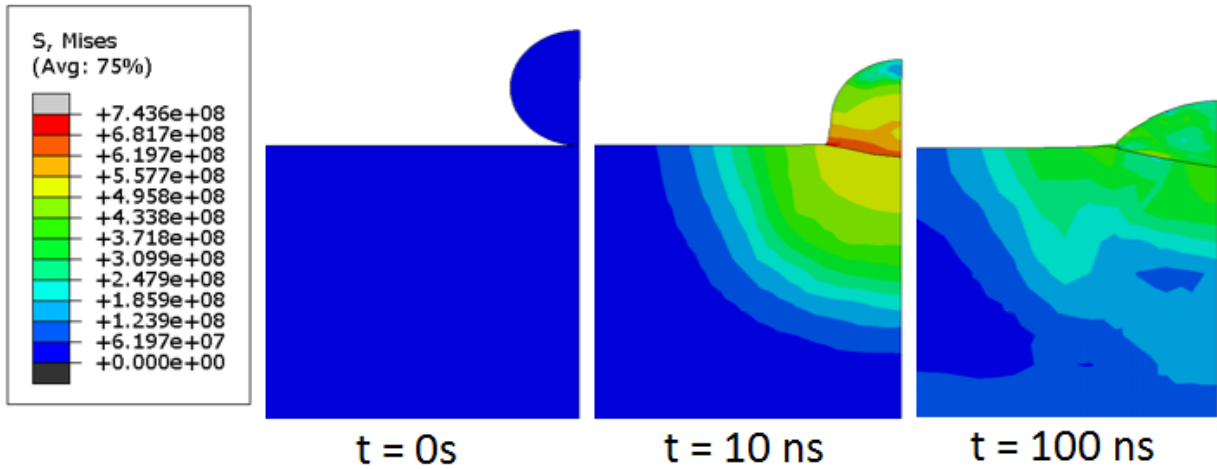


Figure 81: Stress evolution over time for 6061 aluminum alloy particle impact on 6061 substrate using bilinear Johnson-Cook plasticity mode at 770 m/s<sup>6</sup>

The inclusion of the oxide layer in the BJC model increased the substrate deformation but reduced the particle deformation. More of the oxide layer is left within the simulation, suggesting a velocity above 770 m/s may increase particle adhesion.

<sup>6</sup> Simulation name "bjc-6061-long-600K"

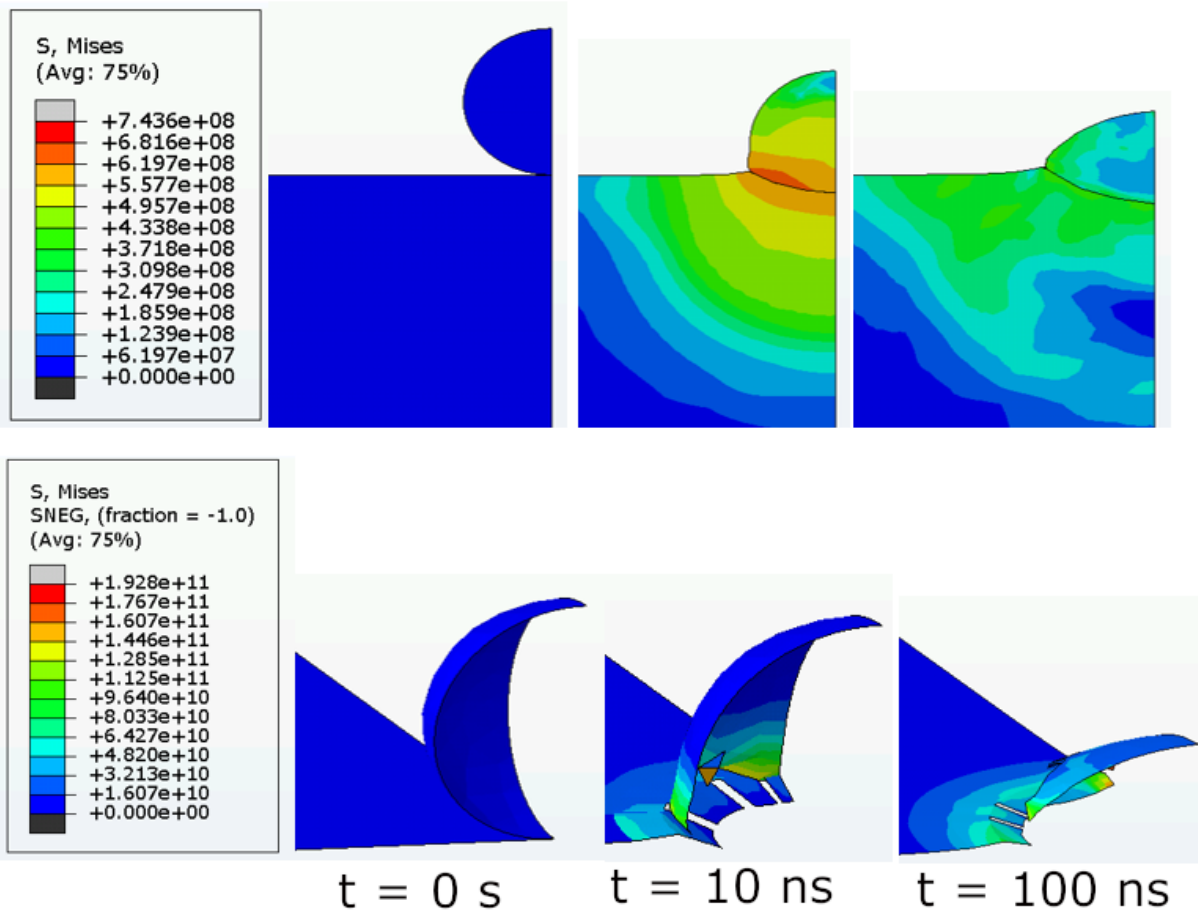


Figure 82: Stress evolution over time for 6061 aluminum alloy particle impact on 6061 substrate using bilinear Johnson-Cook plasticity model with 5 nm oxide layers at 770 m/s<sup>7</sup>

The bilinear JC simulation was also run above and below the critical velocities reported for 6061 aluminum alloy (500 m/s and 90 m/s) to study how and when the oxide layer fails. As expected there is significantly more oxide layer left in the simulation below the critical velocity of the material. However, the oxide layer left in the simulation for at 900 m/s is not significantly different from that at 770 m/s suggesting that model does not capture all aspects of the impact behavior.

<sup>7</sup> Simulation name "job1-imp1-bjc-ndc-600k-v2"

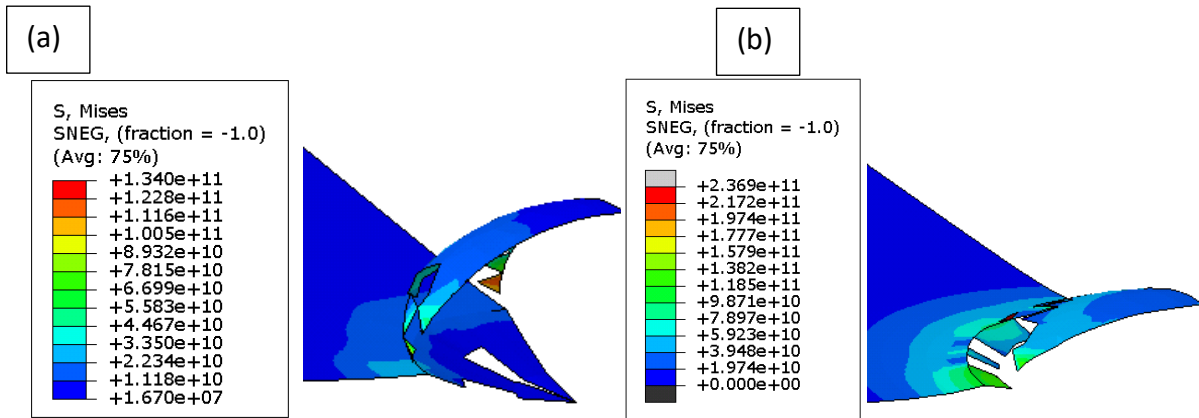


Figure 83: Aluminum oxide layer left after 100 ns in the bilinear Johnson-Cook simulation at 500 m/s (a)<sup>8</sup> and 900 m/s (b)<sup>9</sup>

### 3.6 Fatigue of 6061 Aluminum Alloy

Fatigue specimens were designed to fit bulk cold sprayed samples with thicknesses of 12.6 mm. The chosen sample was single edge bending (SEB) due to the compact design and simpler fixturing requirements. Figure 84 below, shows the general representation of the fixture layout used in testing. However, a crack opening displacement gage was not used in our setup due to size limitations.

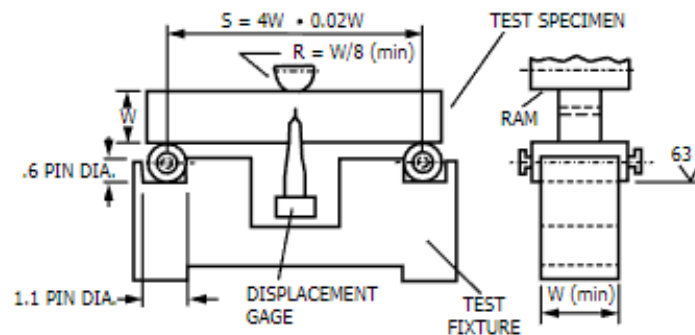


Figure 84: Three point bend representative fixture (ASTM E1820-18ae1)

The samples for this work were based on the ASTM E1820-18ae1 standard for a SEB specimen, with the CNC machined dimensions shown in Figure 85 below. A 0.25 mm slitting saw was used to make the initial notch meeting the specifications for a straight through narrow notch.

<sup>8</sup> Simulation name "Job\_1\_imp1\_bjc\_ndc\_600k\_500ms"

<sup>9</sup> Simulation name "job1\_imp1\_bjc\_ndc\_600k\_900ms"

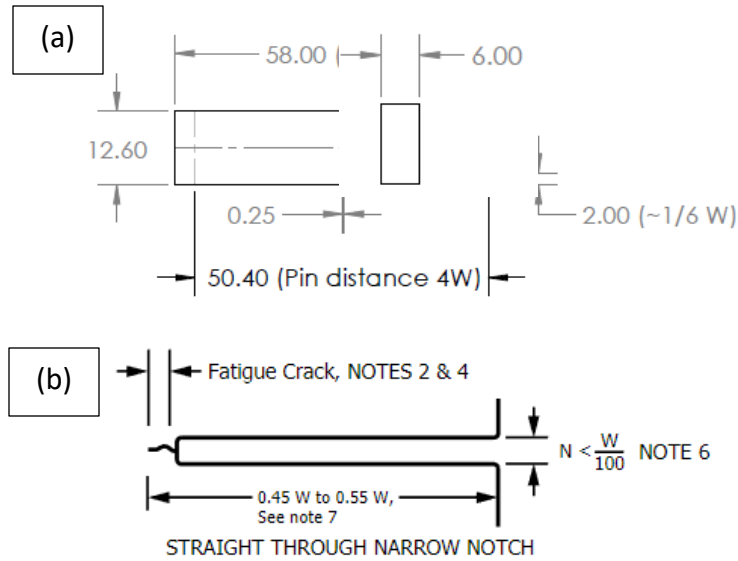


Figure 85: Fracture specimen used in bulk material work (dimensions in mm) (a). Strait through narrow notch criteria (b) (ASTM E1820-18ae1).

Fatigue pre-cracking is required to get a truly sharp crack. The formulations for the SEB geometry from ASTM E1820-18ae1 were used to find the load required to produce an acceptable crack. Linear elastic stress concentration,  $K_Q$ , can be determined from equation 37 below.

$$K_Q = \frac{P_Q S}{\sqrt{B B_N} W^{3/2}} \cdot f\left(\frac{a}{W}\right) \quad (37)$$

$P_Q$  is the load on the sample,  $S$  is the support span,  $B$  is the specimen thickness,  $B_N$  is the thickness at the notch,  $W$  is the specimen height, and  $a$  is the crack length. A function for a geometric constant (specific to the SEB specimen),  $f$ , is found in terms of the ratio of the crack length to the specimen height.

$$f\left(\frac{a}{W}\right) = 3\sqrt{\frac{a}{W}} * \frac{1.99 - \left(\frac{a}{W}\right) \left(1 - \frac{a}{W}\right) \left[2.15 - 3.93\frac{a}{W} + 2.7\left(\frac{a}{W}\right)^2\right]}{2\left(1 + 2\frac{a}{W}\right) \left(1 - \frac{a}{W}\right)^{\frac{3}{2}}} \quad (38)$$

For our specimen, the equation can be simplified to equation 39 below as the thickness is identical throughout the entire specimen.

$$K_Q = \frac{P_q S}{B W^{\frac{3}{2}}} * f\left(\frac{a}{W}\right) \quad (39)$$

The equation can then be rearranged to solve for the required load on the sample. Fatigue pre-cracks are typically created with a sinusoidal loading function where the maximum stress concentration,  $K_{max}$ , should not exceed 80% of  $K_{IC}$ , the stress ratio,  $R$  ( $K_{min}/K_{max}$ ), should be between -1 and 0.1, with a frequency up to 100 Hz according to ASTM E1820-18ae1 specifications. A good pre-crack will be sharp, straight, and outside of the any plastically deformed areas of the notch during machining. Given a mode one fracture toughness of around  $35 \text{ MPa}\sqrt{\text{m}}$  for 6061-T6 (Polmear et al. 2017), our chosen parameters of; stress concentration range of 8 MPa, a stress ratio of 0.1, and a frequency of 10 Hz put us well within the ASTM specifications. A servo-hydraulic testing machine was used to produce the required static and cyclic loads for the test.

$$P_Q = \frac{BK_q W^{\frac{3}{2}}}{Sf\left(\frac{a}{W}\right)} \quad (40)$$

Solving for load at minimum and maximum stress conditions results in the following loading curve<sup>10</sup>.

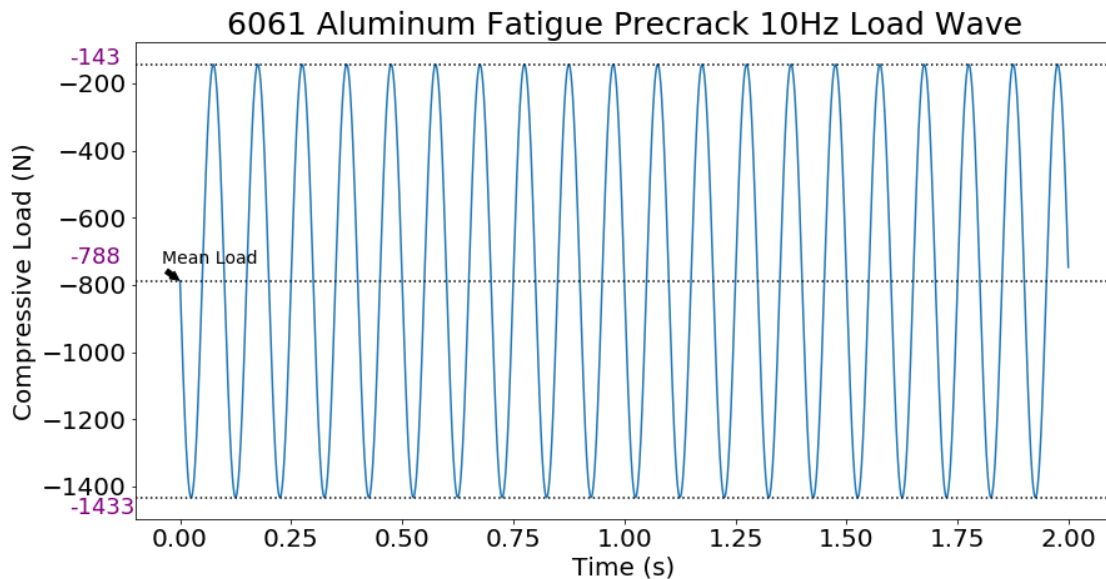


Figure 86: Fatigue loading conditions used for 6061 aluminum alloy SEB samples

About every 1000 cycles the fatigue load was paused and the sample was held under the mean load for measurement of the crack length. Acetate paper was used to produce a copy of the

<sup>10</sup> A short python program was written which can be used to find the required load given a target stress concentration or visa-versa for a single edged bend specimen. This has been posted to my github account "snesnehne" and is available for public use.

crack for observation and measurement with an optical microscope. A linear trend is visible in the log-log plot (Figure 87) of crack growth rate versus stress concentration similar to that seen in the literature for 6061 in the phase 2 stage of crack growth. However, as the crack path itself was sinuous, the measured crack growth rate has variation from the ideal.

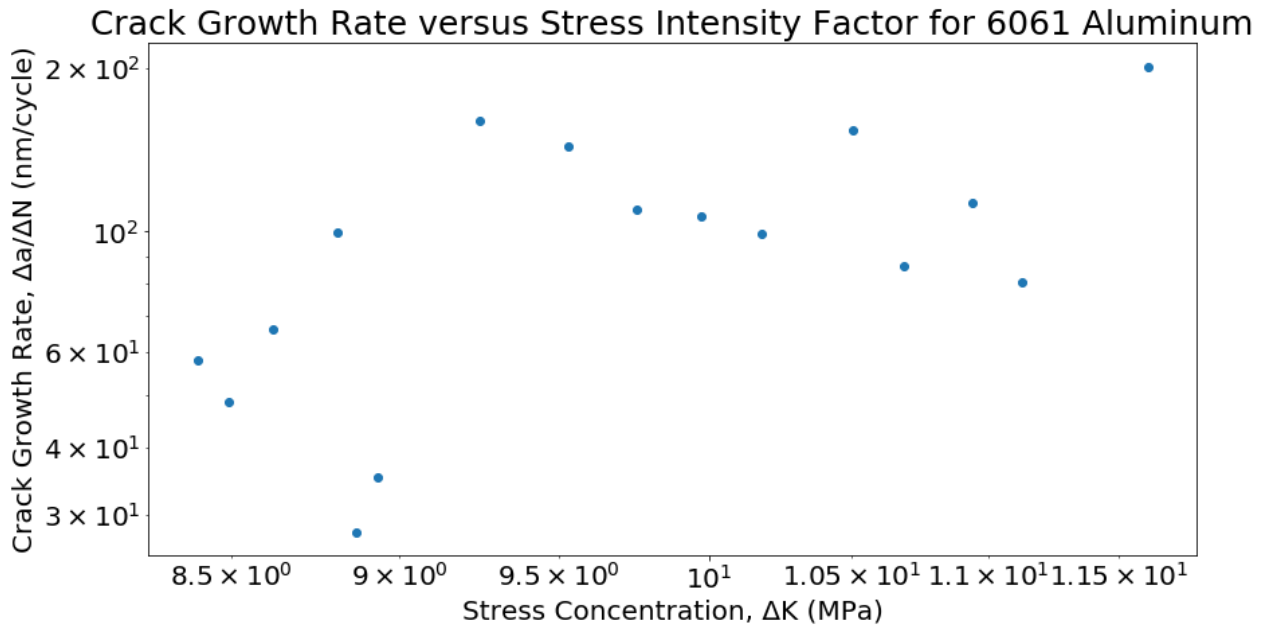


Figure 87: Crack growth at different stress concentrations for a 6061 aluminum alloy single edged bend specimen

### 3.7 Implications

Wrought 6061 aluminum alloy and gas-atomized 6061 powder have similar chemical compositions but significantly different microstructures largely due to the difference in cooling rate. Grain sizes in wrought aluminum are roughly an order of magnitude larger than those for the gas-atomized powder. Precipitates and inclusions tend to be smaller in the powder form as well. Tensile samples smaller than those specified in ASTM specifications were shown to provide accurate representations of 6061 aluminum’s stress-strain behavior. Fatigue crack growth rates were also similar to those in literature for wrought 6061, suggesting the sample type will work well for bulk cold sprayed 6061. Smaller sample designs were required in order to fit the size limitations of bulk cold sprayed material available to researchers. Similar to pure aluminum, 6061 aluminum alloys also displayed an indentation size effect despite increased variability due to secondary phases and inclusions in the material. Annealed 6061 (with lower residual stress and dislocations) showed a clearer ISE than the T6 condition with the highest precipitate influenced strength. Abaqus FEA simulation suggested that nano-indenters with a Berkovich indenter should be spaced at more than 15 times the depth of the indent to avoid

previous indents effecting the results of new indents. Additionally, the shape of the stress zone backed up claims that tip rounding in a Berkovich tip could be modeled as a spherical indenter. The Lagrangian elements in this simulation can be used for low depth indents, but Eulerian elements should be explored for simulation of deeper indents as a result of excessive element deformation impacting convergence in Lagrangian elements.

The machine learning prediction of hardness requires more data or potentially more advanced models such as GANs to provide accurate results. The author hopes that increases in data sharing in the field of materials science will make this possible, and that other researchers may see the potential applications of machine learning in materials science. Inclusion of an oxide layer in the FEA simulation predicts leftover oxides at the bottom of the particle impact. This is consistent with experimental results from researchers such as Balani et al. (2005) and is a likely source of weakness in the material interface. Further refinement of the model could be used to predict the spray parameters which would leave the least amount of oxide behind. The bilinear Johnson-Cook results exhibit less particle deformation than the linear model due to the increased strain hardening at high strain rates.

## Chapter 4: Microstructure and Mechanical Properties of Extruded CP Ti, Ti-6Al-4V and Cold-sprayed Ti-6Al-4V

### 4.1 Microstructure of Titanium Alloys

#### 4.1.1 Ti-6Al-4V Rod and Plate

A Ti-6Al-4V extruded rod with 12.7 mm diameter, meeting ASTM Specification B265 – 15 was used in this work. The exact composition of the Ti64 plate was not specified by the manufacturer, but meets ASTM specifications for Ti64 and would be very similar to the composition seen in Table 21, below.

Table 21: Composition of Ti-6Al-4V rod as reported by the manufacturer

Composition of Ti-6Al-4V (%)							
Ti	Al	V	C	Fe	N	O	Others
Remainder	6.09	4.1	0.031	0.18	0.005	0.11	<.10 each

Etching the surface with Kroll's reagent reveals the darker discontinuous  $\beta$  phase as well as the grain boundaries of  $\alpha$  phase.

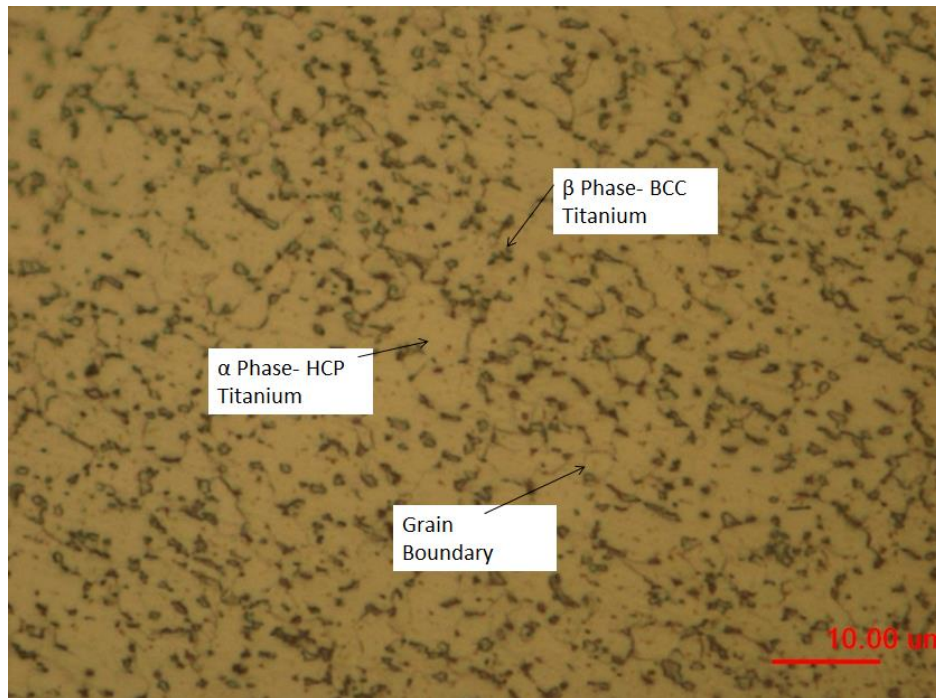
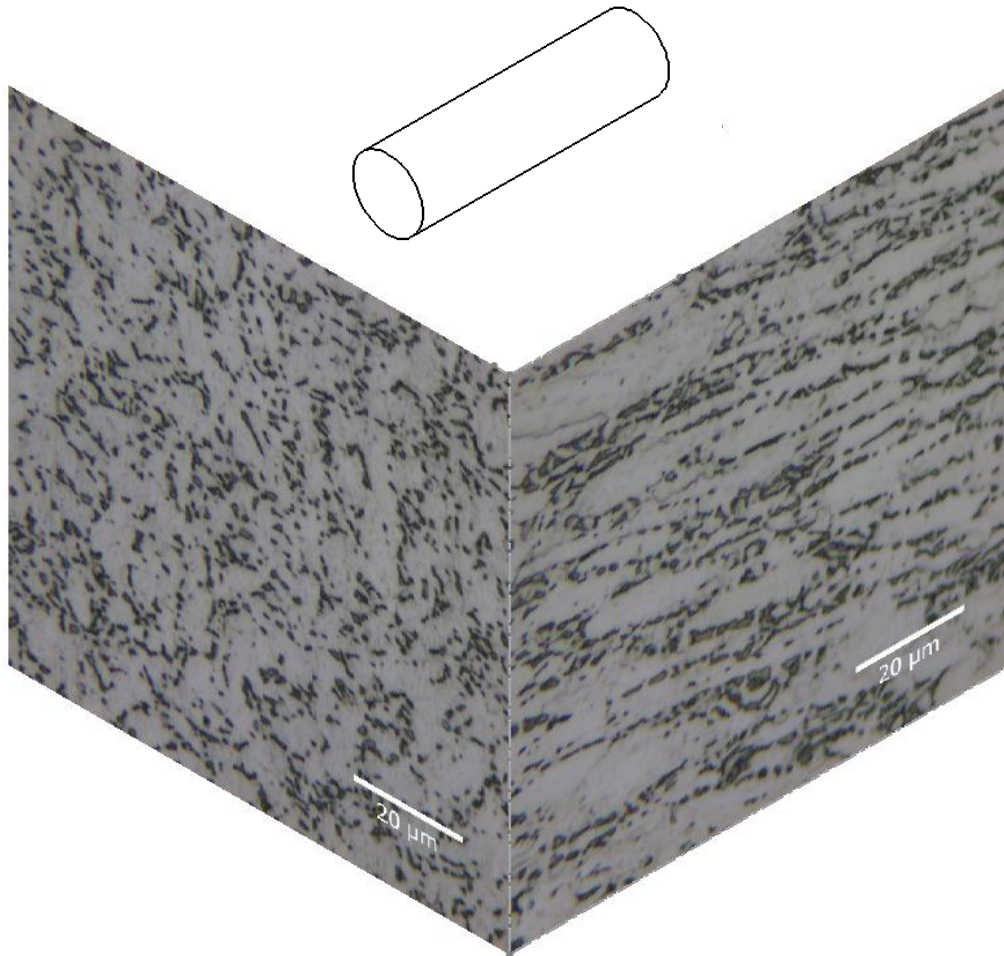


Figure 88: Ti-6Al-4V rod cross-section taken with a visual light microscope revealing lighter colored equiaxed grains of  $\alpha$  phase (HCP) and darker sections of discontinuous  $\beta$  phase (BCC). Etched with Kroll's reagent by swabbing with q-tip for 20s.

Figure 89 below shows the impact of directionality on the microstructure of these Ti-6Al-4V extruded rods. The grains are normally equiaxed, but become elongated in one direction as a result of stresses created during the extrusion process.



*Figure 89: Ti-6Al-4V taken with a visual light microscope showing equiaxed grains across the extrusion direction (longitudinal cross-section)(a), but elongated grains along the extrusion direction (lateral cross-section)(b). Etched with Kroll's reagent by swabbing with q-tip for 20s.*

Again, EDS was used to confirm material compositions in different parts of the microstructure. Figure 90 below validates locations of  $\alpha$  and  $\beta$  phase titanium. Spectrum 1 is at a location with  $\alpha$  phase and therefore titanium and aluminum (an  $\alpha$  stabilizer) are detected. Titanium and vanadium are detected at the location for Spectrum 2 because it is in  $\beta$  phase which is stabilized by the vanadium. The EDS software also lists barium as an element that is potentially detected (red coloring indicating uncertainty in the analysis), but the characteristic peaks of titanium and barium are close to each other. Therefore, it is not uncommon for EDS to mistakenly mischaracterized titanium as barium (Goldstein et al. 2017). As there is an insignificant amount of barium in Ti64, its detection can be effectively ruled out.

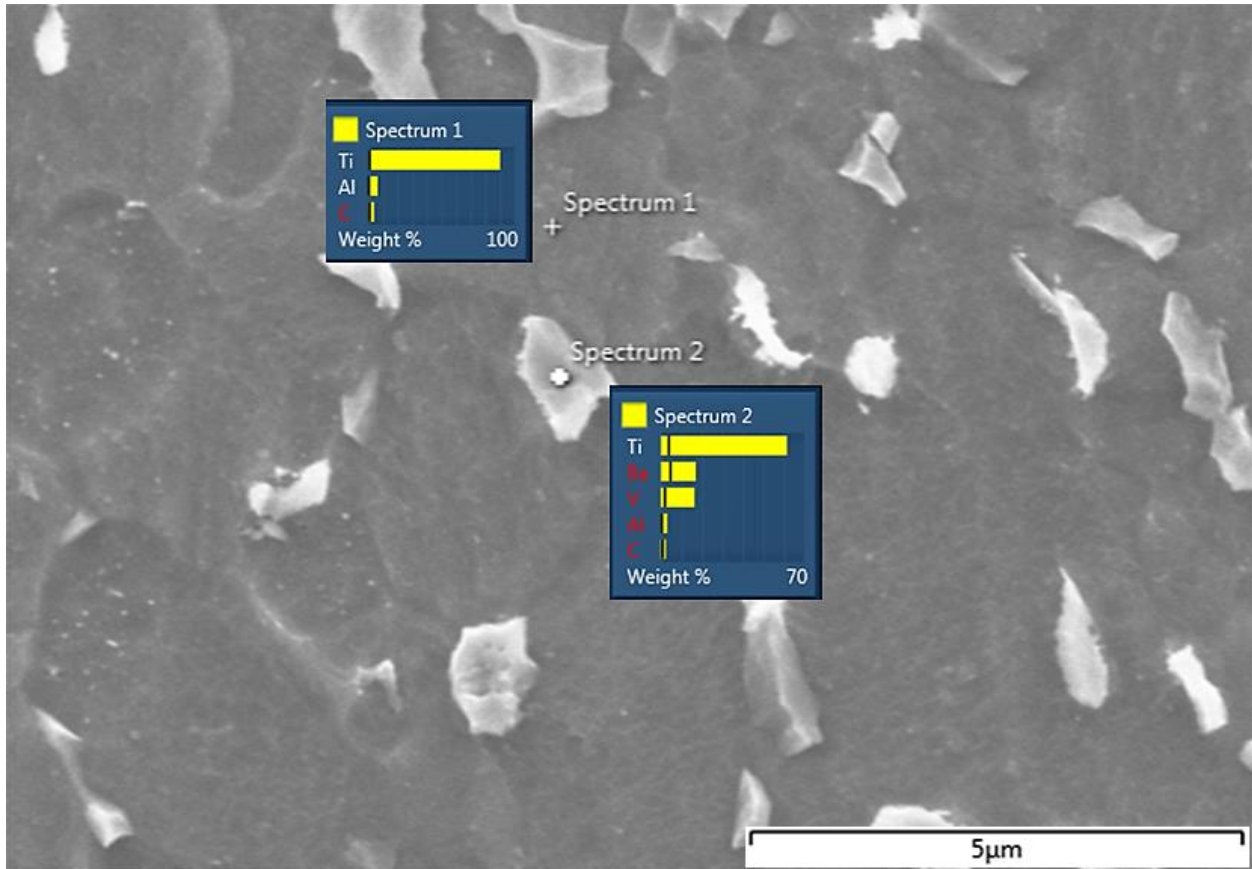
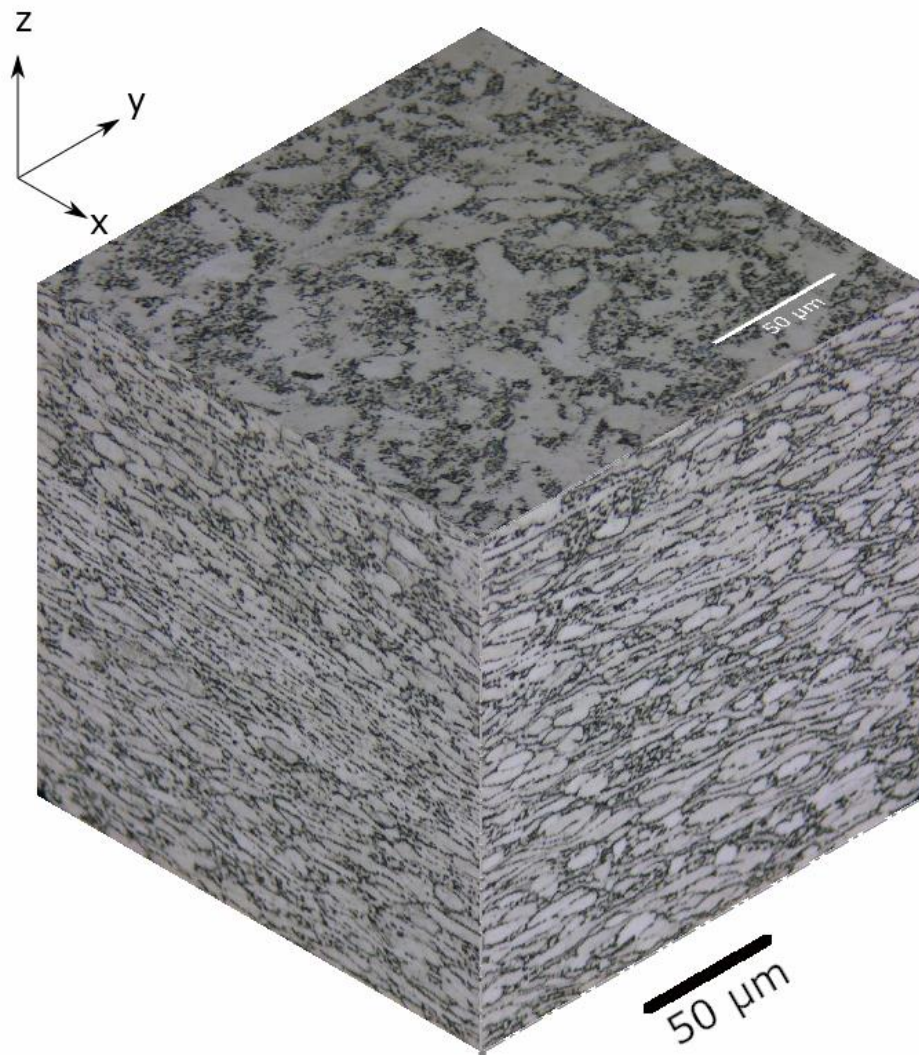


Figure 90: SEM topographic image with EDS data taken at two locations confirming  $\alpha$  and  $\beta$  phases in Ti-6Al-4V. Etched with Kroll's reagent by swabbing with a q-tip for 20s.

The effects of processing on the grain structure of titanium alloys are also clear in images taken of Ti-64 plate material. Figure 91 below shows the more equiaxed grains in the z direction, while the grains in the lateral and longitudinal directions have been deformed into oblong shapes from the extrusion process.



*Figure 91: Three dimensional composite visual light microscopy image showing the etched cross-sections of Ti-6Al-4V plate in each direction*

#### 4.1.2 Commercially Pure Titanium Powder

The commercially pure powder our group investigated was heavily skewed towards smaller particle diameters with an average diameter of 15  $\mu\text{m}$  and a standard deviation of 9  $\mu\text{m}$ .

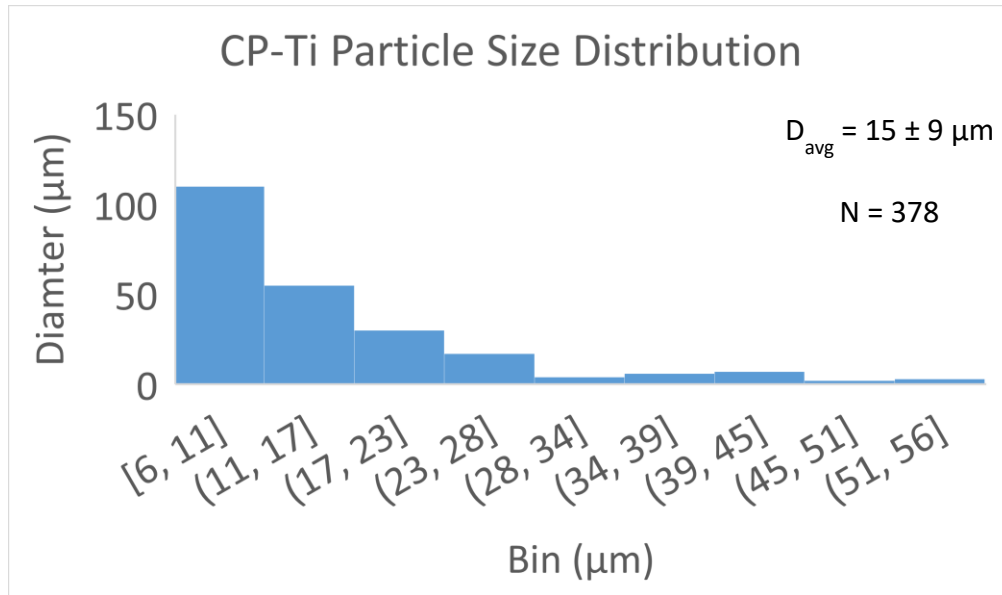


Figure 92: Particle size distribution of gas-atomized commercially pure titanium powders

Both of the titanium powders inspected had smoother surfaces and were more spherical than the aluminum powder. Rapid solidification of the liquid powder likely contributed to unequal cooling in the sphere which produced ridges or plate-like features on the surface.

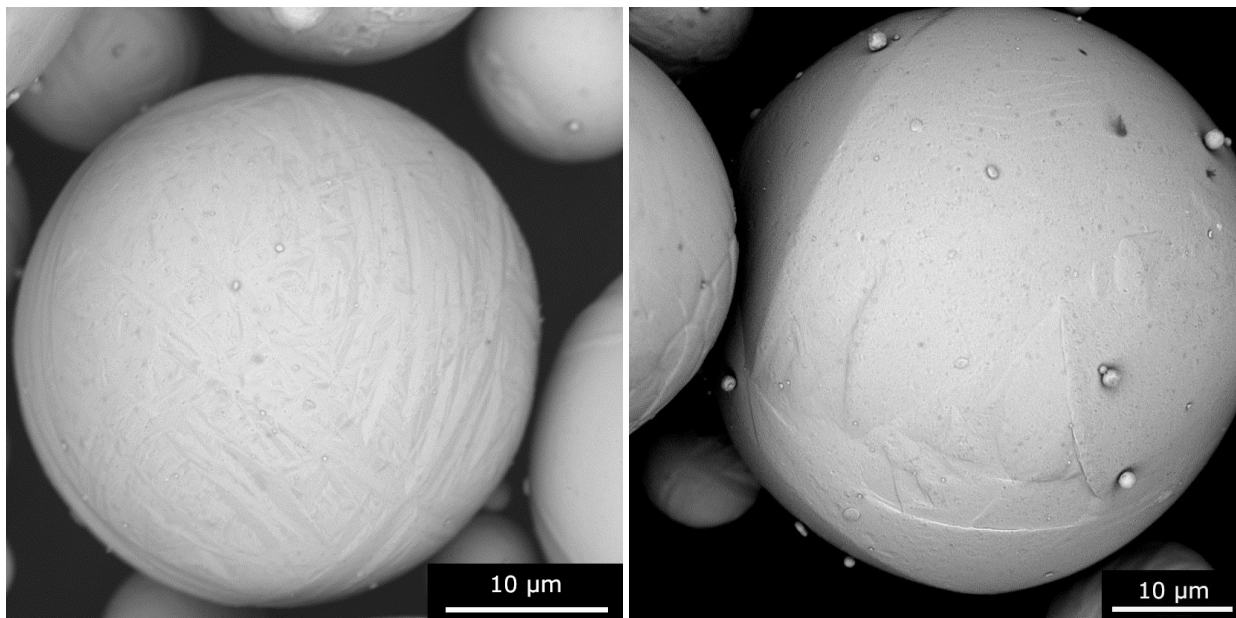
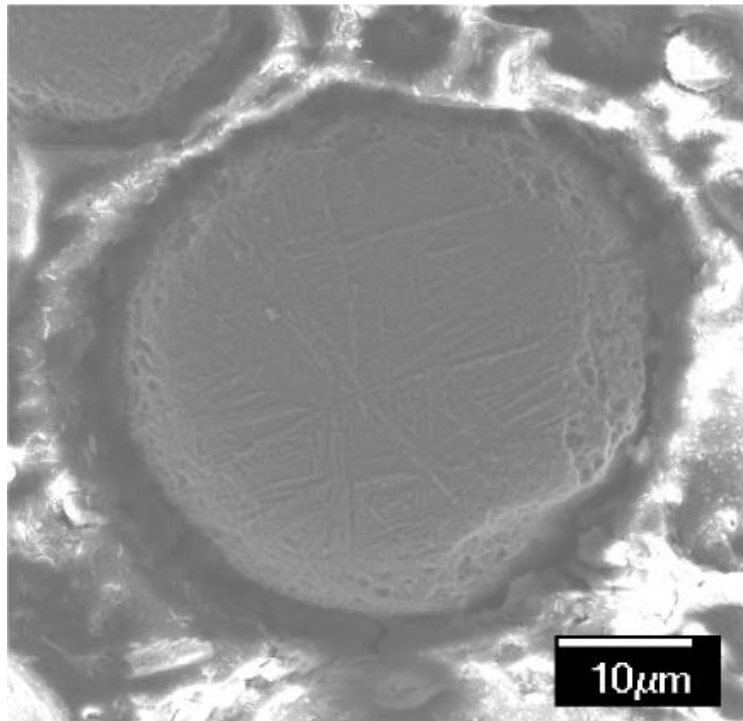


Figure 93: External topography of CP-Ti powder showing evidence of rapid solidification

Evidence of martensitic structures resulting from the rapid cooling of the particles was also seen in the internal structure of the powder. Etching of the powder cross-section revealed

acicular structures in the powder as well as variations in the external surface as evidenced by pits.



*Figure 94: Cross-section of CP-Ti powder etched with Kroll's reagent for 10s to show acicular microstructure. Powders were mounted in a phenolic epoxy and polished before etching.*

#### 4.1.3 Ti-6Al-4V Powder

Powder diameter variability for the Ti64 powder was lower than for the other powders studied. The average powder diameter was 25  $\mu\text{m}$  with a standard deviation of 5  $\mu\text{m}$ . The distribution was essentially Gaussian.

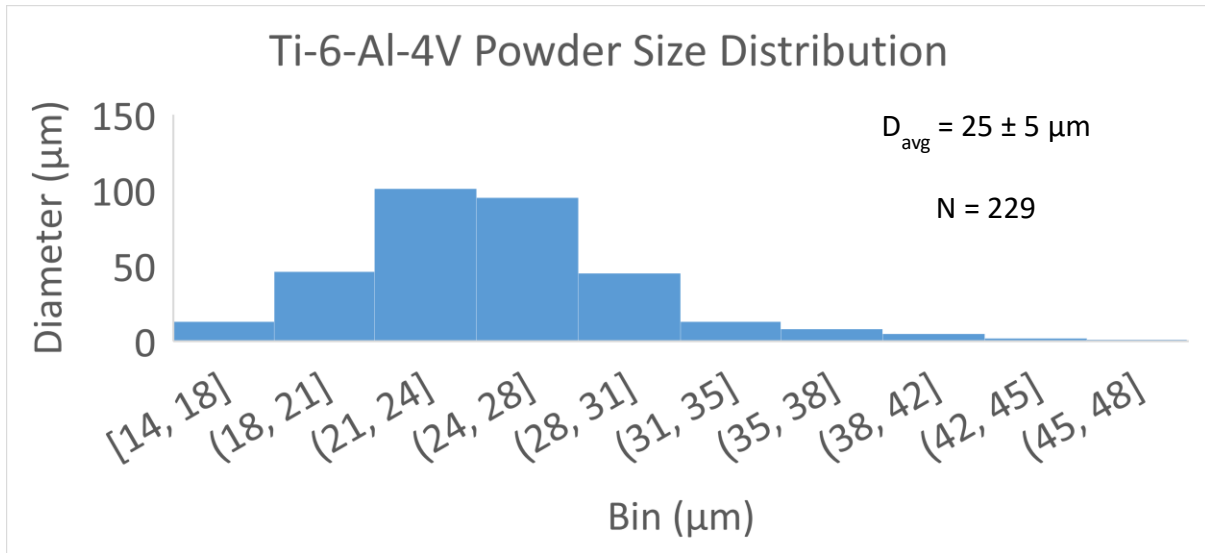


Figure 95: Particle size distribution of gas-atomized Ti-6Al-4V powders

As with the commercially pure titanium powders, the Ti64 powders were highly spherical. The particle surfaces were smoother than for the 6061 powder, but a cellular grain structure could also be observed on the exterior of some unetched powders. Other particle surfaces revealed a plate-like structure with large smooth patches and ravines between plates.

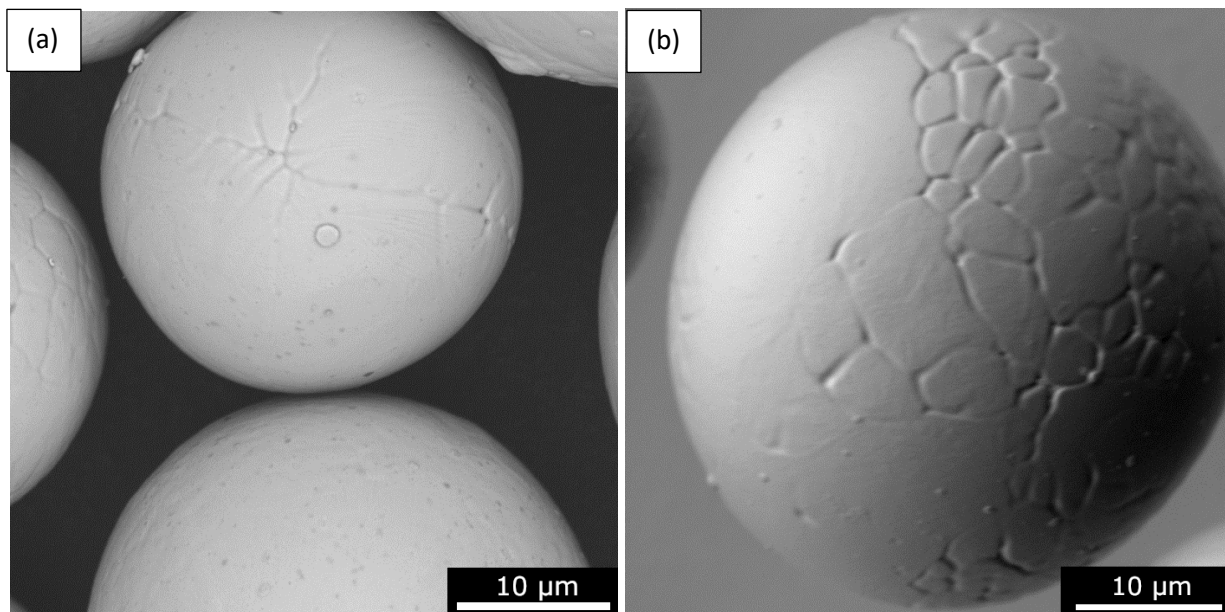
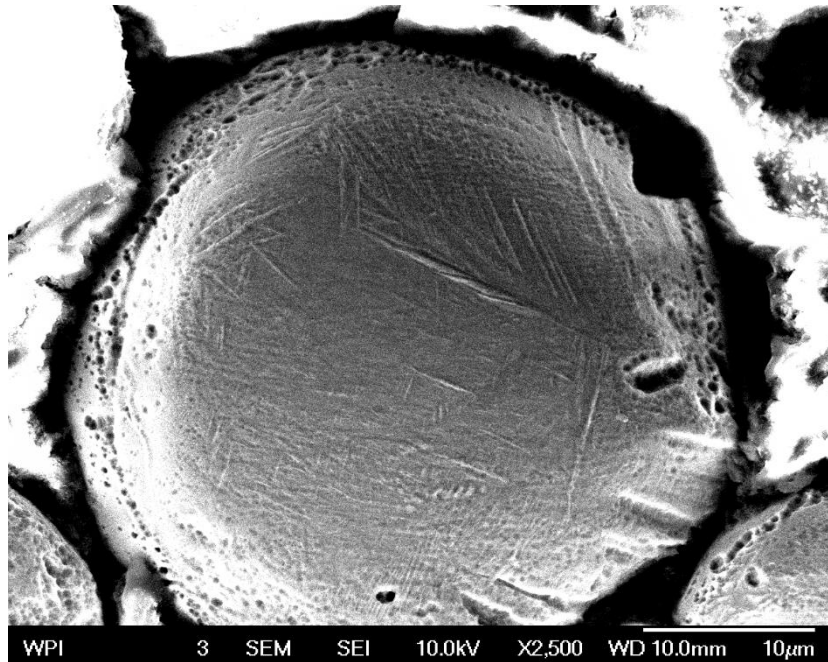


Figure 96: SEM topographic image of Ti-6Al-4V powders showing plate-like (a) and cellular grain structures (b)

The internal structure for the Ti64 powders looked similar to that for the CP titanium powders. An acicular structure was also revealed after etching the cross-section of the powder. This

result is not entirely surprising given how rapidly the particles in atomization processes cool (Neikov 2019).



*Figure 97: Cross-section of Ti-6Al-4V powder etched with Kroll's reagent for 10s to show acicular microstructure. Powders were mounted in a phenolic epoxy and polished before etching.*

#### [4.2 Stress-Strain Behavior of Titanium Alloys](#)

The experimental setup for Ti-6Al-4V tensile testing was identical to that for 6061 discussed above with the exception of slightly larger grip sizes. The grip sizes had to be modified in order to prevent slippage of the samples within the jaws of the servo-hydraulic testing machine. Directionality was more important in these samples than for the aluminum with the lateral (or transverse) samples having higher strengths and elongations. This is consistent with the data reported by the manufacturer seen in Table 22 below. When considering the microstructural images taken of the material, the results suggest that the more oblong grains seen in the longitudinal direction provide additional strengthening to the cross section in the lateral direction tensile tests.

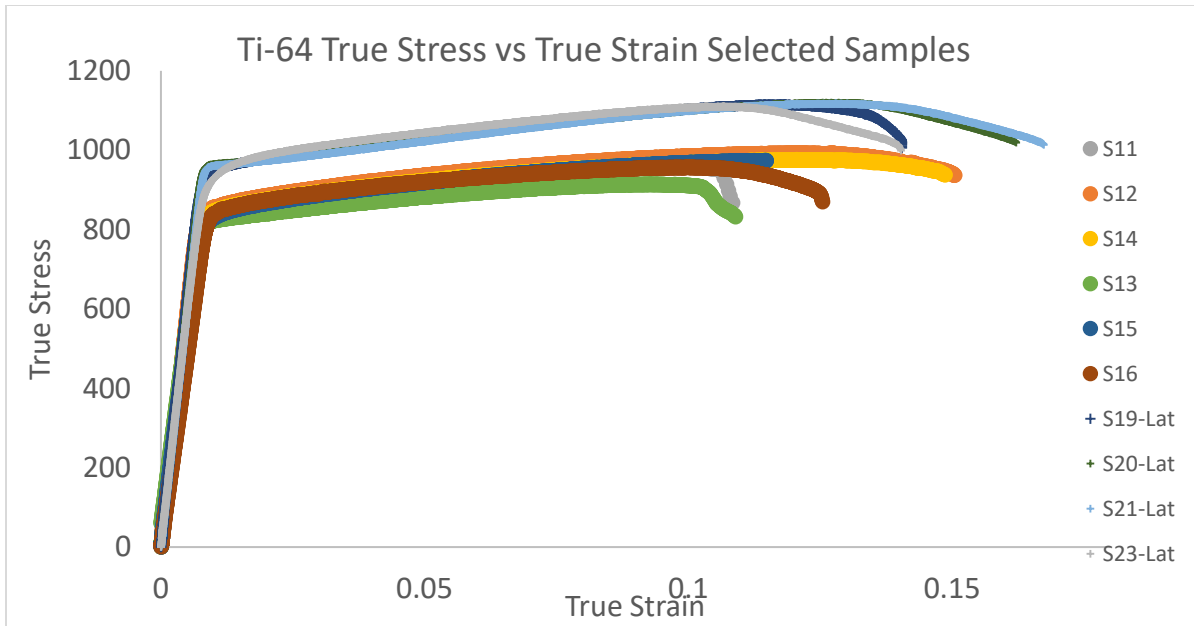


Figure 98: Stress strain curves of Ti-6Al-4V tensile samples in longitudinal and lateral directions

The strain hardening curves for Ti-6Al-4V were steeper than for 6061 resulting in higher strain hardening coefficients. Again the parameters for the Ramberg-Osgood equation were found and provided a reasonable approximation of the true stress-strain behavior as the samples exhibiting power-law strain hardening.

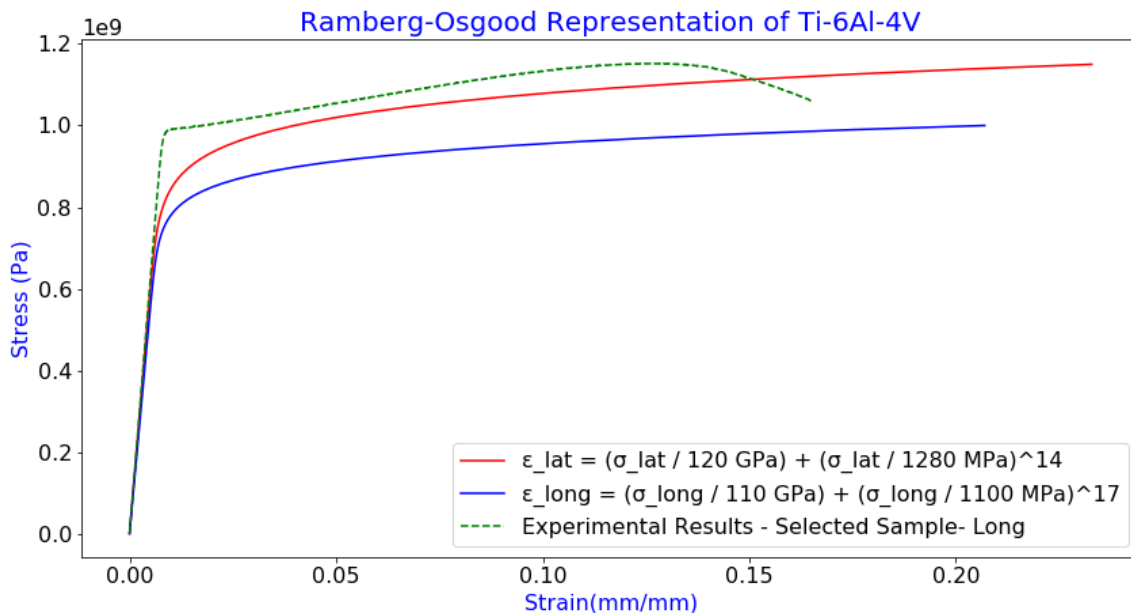


Figure 99: Ramberg-Osgood representations of lateral and longitudinal samples compared with the raw true stress-strain curve from a longitudinal sample of Ti-6Al-4V

The Ramberg-Osgood representation did not match as well for the Ti-6Al-4V, which is not entirely surprising given that the Ramberg-Osgood equation was originally built on aluminum alloy data (Ramberg and Osgood 1943). However, the Ramberg-Osgood relationship still provides a representation which is fairly true to the measured stress-strain until the onset of necking around 13% strain. The R-squared for one of the Ramberg-Osgood representations was 0.80, while the others obtained poor coefficient of determinations. Hollomon strain hardening coefficients were measured to be within the range reported in literature

Table 22: Ti-6Al-4V mechanical reference parameters from the material manufacturer, CES Edupack (a), and Gupta et al. (b)

Ti-6Al-4V Mechanical Reference Parameters					
	Manufacturer Certification		Literature (a)		Units
	Longitudinal	Transverse	min	max	
<b>Yield Strength (0.2% Offset)</b>	894.9	1010	786	910	MPa
<b>Ultimate Tensile Strength</b>	963.2	1086.6	862	1200	MPa
<b>% Elongation</b>	13.0%	14.0%	10%	14.0%	
<b>Ramberg-Osgood Parameters</b>			<b>Typical (b)</b>		
<b>Strain Hardening Coefficient (n)</b>			0.03-0.23		
<b>Strengthening Coefficient (K)</b>			1100-3000		MPa

Table 23: Summary of Ti-6Al-4V mechanical properties found during tensile testing

Ti-6Al-4V Tensile Test Results					
	Lateral		Longitudinal		Units
	Avg	Std	Avg	Std	
<b>Yield Strength (0.2% Offset)</b>	961	19.9	840	13.3	MPa
<b>Ultimate Tensile Strength</b>	1106	19.9	965	29.8	MPa
<b>Elastic Modulus, E</b>	122	3.5	110	6.9	GPa
<b>% Elongation</b>	15%	2%	13%	2%	
<b>Ramberg-Osgood Parameters</b>					
<b>Strain Hardening Coefficient (n)</b>	0.070	0.11	0.060	0.00	
<b>Strengthening Coefficient (K)</b>	1280	34.6	1110	35.3	MPa
<b>Ramberg Osgood Parameter (1/n)</b>	14.4	1.78	16.6	1.18	

The fracture surfaces of the Ti64 tensile specimens showed less necking, but still a relatively large degrees of ductility. Fracture tended to occur along different planes in comparison with the relatively homogenous fracture surface seen in 6061-T6 aluminum alloy. These fracture planes typically occurred at 45° from the loading axis which is where the highest shear strain is expected. Less extensive dimpling relative to aluminum can be seen in Figure 100 (b).

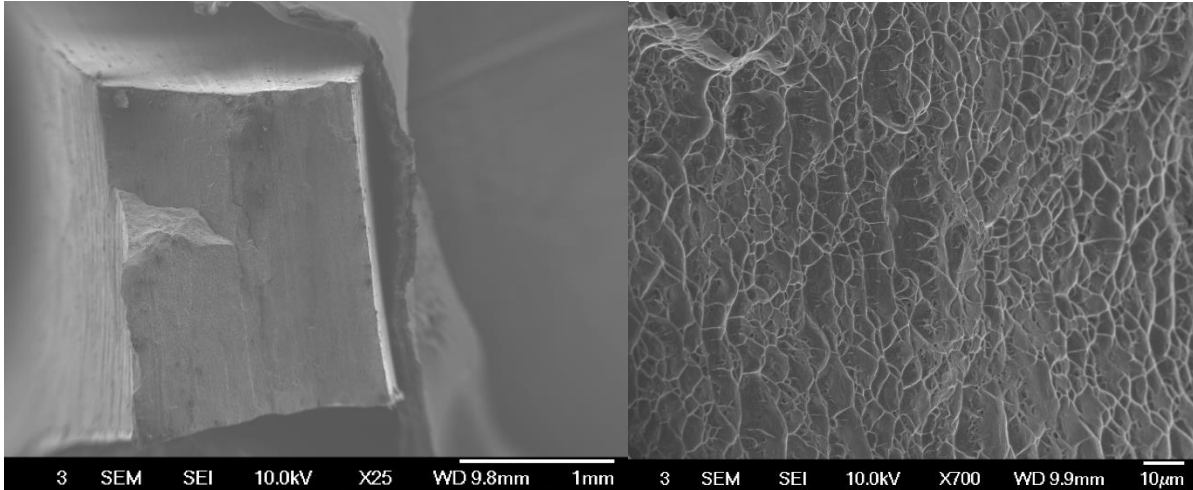


Figure 100: SEM images of Ti-6Al-4V fracture surfaces show a moderate amount of necking, as well as shear at a  $45^\circ$  angle to the loading axis (a). The sample is being supported by carbon tape which can be seen off the right and top sides of the sample. Additionally dimpling indicative of necking and ductility can be seen at higher magnifications (b).

### 4.3 Indentation Size Effect in CP Titanium and Ti-6Al-4V

#### 4.3.1 Vickers Microhardness

The processing techniques for the titanium samples were identical (with the exception of longer polishing times) to that discussed above for 6061. A strong ISE was observed for both the commercially pure titanium and the Ti64 alloy. The commercially pure titanium sample had generally lower standard deviation as the indent depth increased. This is expected due to increased homogeneity of the material at larger scales.

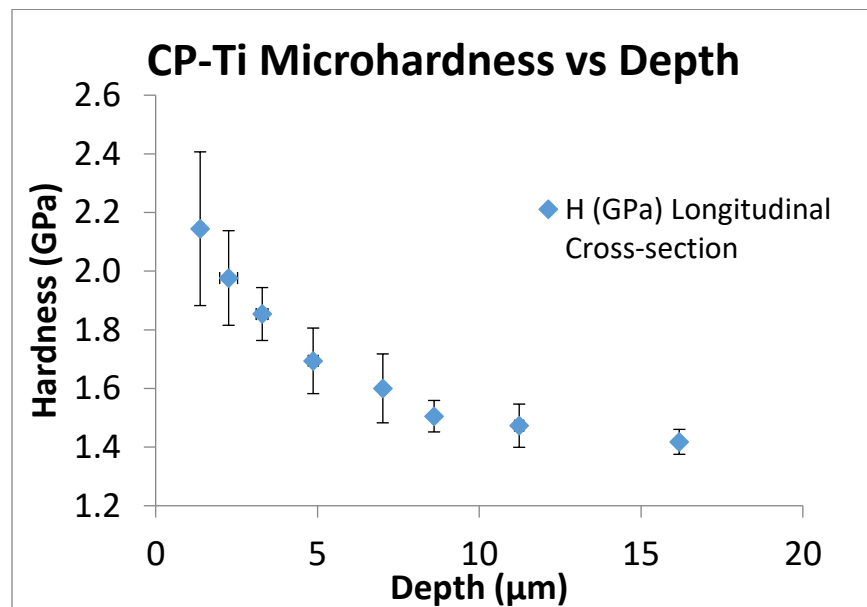


Figure 101: Hardness versus depth for commercially pure grade 2 titanium rod showing ISE

Contrarily, the standard deviation at the second lowest load/depth for the Ti64 was significantly larger than the samples at greater depth. The data suggests this may be due to the presence of alpha and beta phases in the material with different hardness from each other.

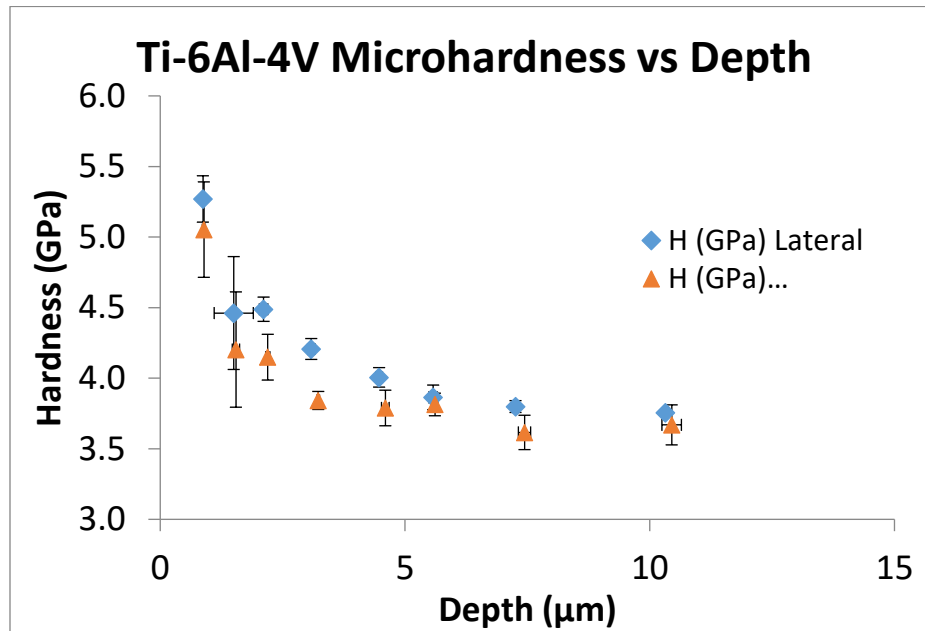


Figure 102: Hardness versus depth for Ti-6Al-4V rod showing ISE in two material orientations

The linearization methods discussed in the literature review and implemented for the 6061 aluminum alloy samples was also used to find the following data for the titanium alloys.

Table 24: Summary of material parameters found by applying Nix and Gao's methods to Vickers microindentation of 6061 aluminum alloy

Material	Measured from Projected Area Microhardness Data		
	H <sub>0</sub> (GPa)	h* (μm)	l (μm)
Ti-6Al-4V ELI Rod Lateral Cross-Section	3.60	0.98	0.32
Ti-6Al-4V ELI Rod Longitudinal Cross-Section	3.41	0.92	0.36
CP Ti Grade 2 -Annealed Rod Cross-Section	1.38	2.18	2.00

#### 4.3.2 Simulation of Low Load Ti-6Al-4V Nanoindentation with Imperfect Berkovich Tip

The nanoindentation simulation done for 6061 aluminum alloy was repeated for Ti-6Al-4V with a 140 nm deep indent versus the 200 nm indent used for 6061. The mechanical properties and

plasticity curves used in the simulation were taken from our tensile testing data for the Ti64 dog-bone specimens. At this low depth, the geometry of the worn tip in the simulation is dominated by a spherical shape rather than ideal Berkovich geometry. Significant pile-up is still seen around the tip of the indent. As a result of this geometry the width of the plastic zone relative to the depth is less than for the deeper indents suggesting that indent spacing could be made closer than the  $d/h \geq 15$  suggested by the 6061 simulation. The size of the plastic zone in this Ti64 indent would require a spacing to depth ratio of 13 to avoid any overlap with other indents of identical depth.

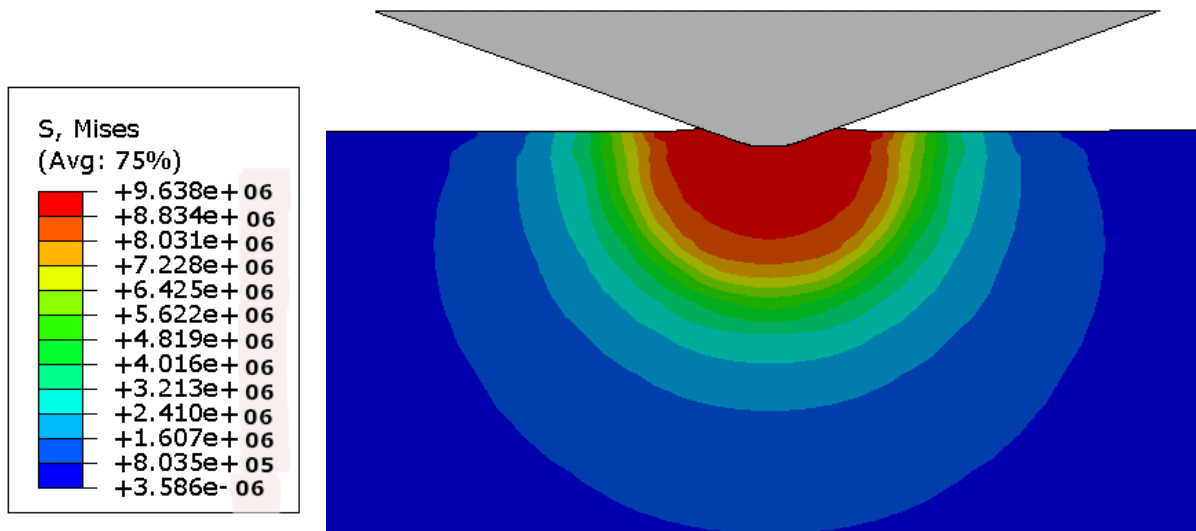
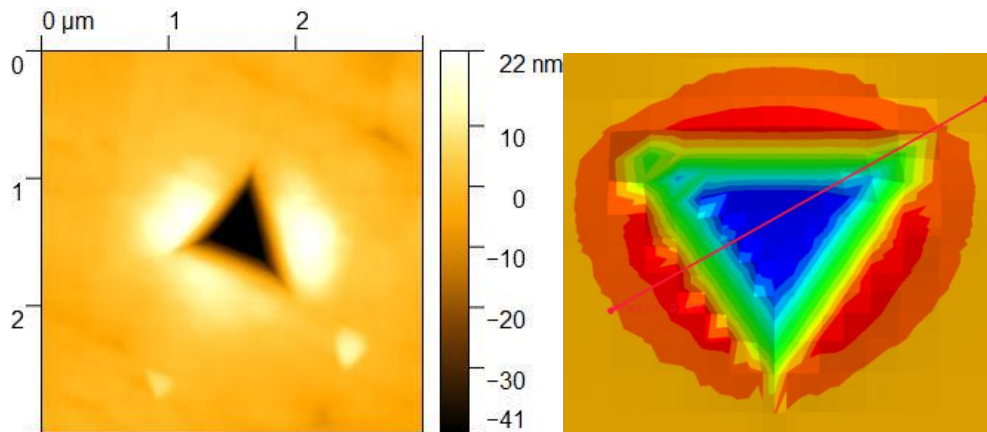


Figure 103: Von-Mises stress in Berkovich indent of Ti-6Al-4V<sup>11</sup>

Another interesting comparison is between the simulated and experimentally measured pileup. An indent under a 2500  $\mu\text{N}$  load resulting in a max indent depth of about 130 nm was performed to produce Figure 104 below. The maximum depth in the simulation was 140 nm. Pileup was measured experimentally using the AFM function on the nanoindenter which samples the height along the surface using the indenter tip shown in Figure 104. The height measurements were taken along a path in Gwyddion and in Abaqus to easily find maximum values for the pileup (Figure 105). The simulated pileup was overall comparable to the pileup from the actual experiment with a maximum height of 24 nm in the simulation compared with 19-22 nm in the AFM data. The maximum depth for the AFM measurements is not accurate as the indenter itself is used for scanning and therefore does not fully reflect the depth at the sharp bottom of the indent. In the experimental results the pileup on each side of the indenter was not identical. This could be due to imperfect geometry of the indenter itself, but is more likely due to microstructural effects in the material. Contrarily, the simulation assumes all faces

<sup>11</sup> Simulation name "Berk 24-Ti64-Exp\_S\_Str/Job-2-2-disp-smaller-min-time-inc.odb"

of the indenter are exactly equivalent and that the material properties of the substrate are isotropic.



*Figure 104: Surface topography scan using Berkovich tip for contact measurement (a). Bright spots surrounding the indent show the pileup from the indent. The small bright spots away from the indent location are likely dust particles. A comparable result is seen in the plot of z displacement from the Abaqus simulation (b)*

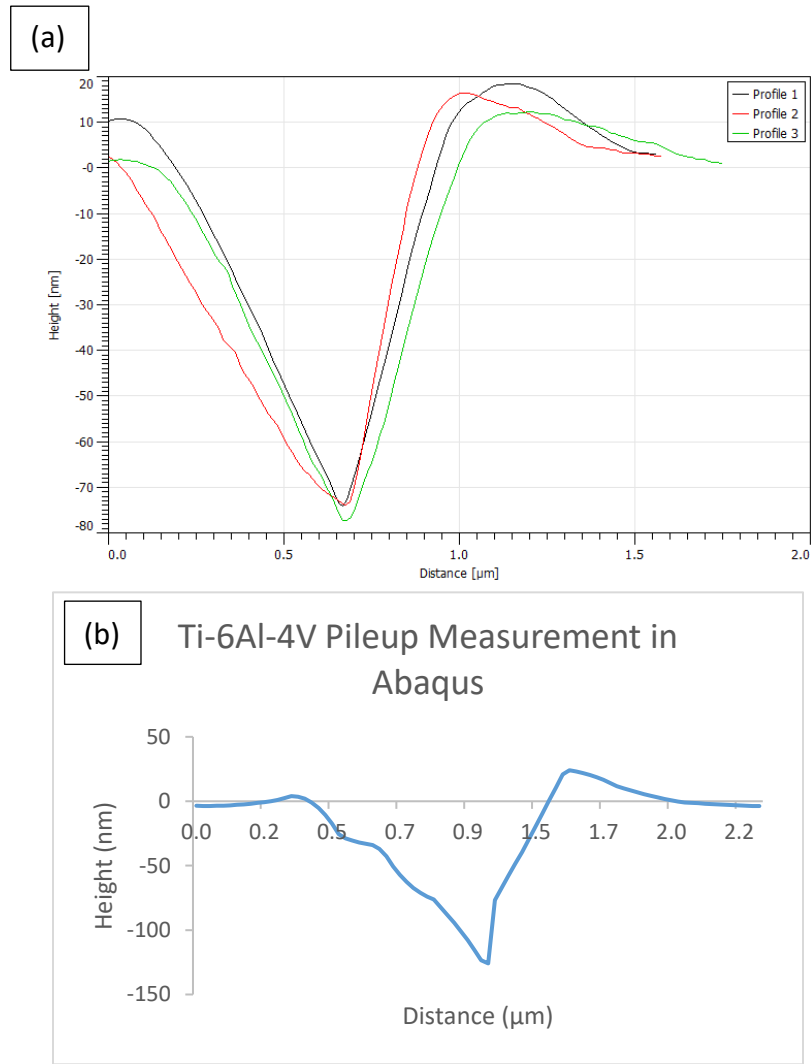


Figure 105: Measurements of pileup along paths using experimental data from AFM in Gwyddion (a) as well as Abaqus (b)

#### [4.4 Simulation of Cold Spray Ti-6Al-4V Impact](#)

The setup of this simulation was identical to the 6061 aluminum alloy simulation with the exception of the material and strain hardening properties. Most of the material properties and the Johnson-Cook constants used were taken from Lesuer et al. (2001) and seen in Table 25 below. The first particle velocity used was slightly higher than the critical velocity of around 800 m/s determined for titanium by Schmidt et al. (2006). Reported temperature ranges for the spray vary widely, but a temperature was chosen for this simulation which was similar to that in work by Khun et al. (2016).

Table 25: Parameters used in Ti-6Al-4V cold spray particle impact simulation

Spray Properties		Material Properties		Bilinear Johnson-Cook Parameters (Lesuer et al., 2001)						
Temperature	Particle Velocity	Young's Modulus	Poisson's Ratio	A	B	n	C <sub>1</sub>	C <sub>2</sub>	m	$\dot{\epsilon}_c$
600K	600 - 1300 m/s	110 GPa	0.3	862 MPa	331 MPa	0.34	0.012	0.029	0.8	1

The TiO<sub>2</sub> oxide layer was assumed to have bulk material properties, but this is likely a poor assumption given the thickness (5 nm) of the oxide layer in the simulation. Future work should update the model with fracture properties of thin film TiO<sub>2</sub> determined from experiments or simulations such as molecular dynamics. The JC Ti64 results were similar overall to those for 6061 particles. However, a significant portion of the oxide layer was left unbroken in the Ti64 simulation, suggesting a higher velocity or temperature would provide a better bond for this material.

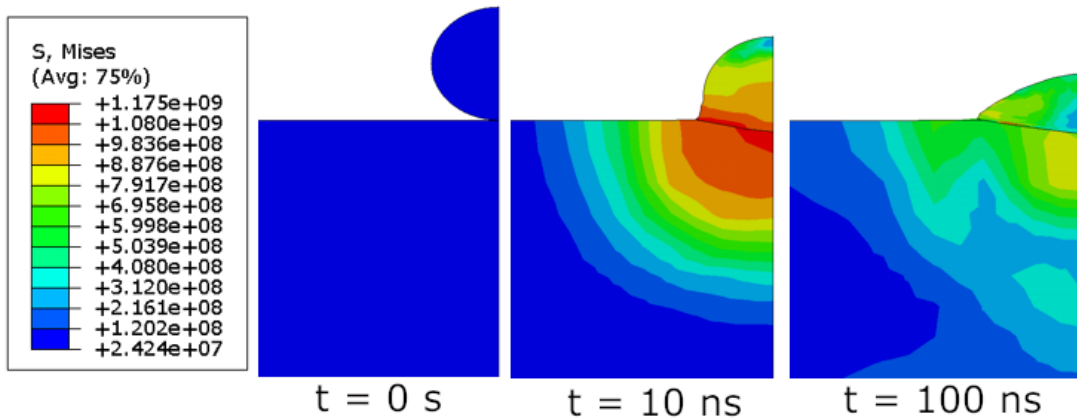


Figure 106: Stress evolution of an 800m/s Ti-6Al-4V particle impacting Ti-6Al-4V substrate without an oxide layer and using Johnson-Cook plasticity<sup>12</sup>

<sup>12</sup> Simulation name "job1-imp2-ti64-ljc-400ksub"

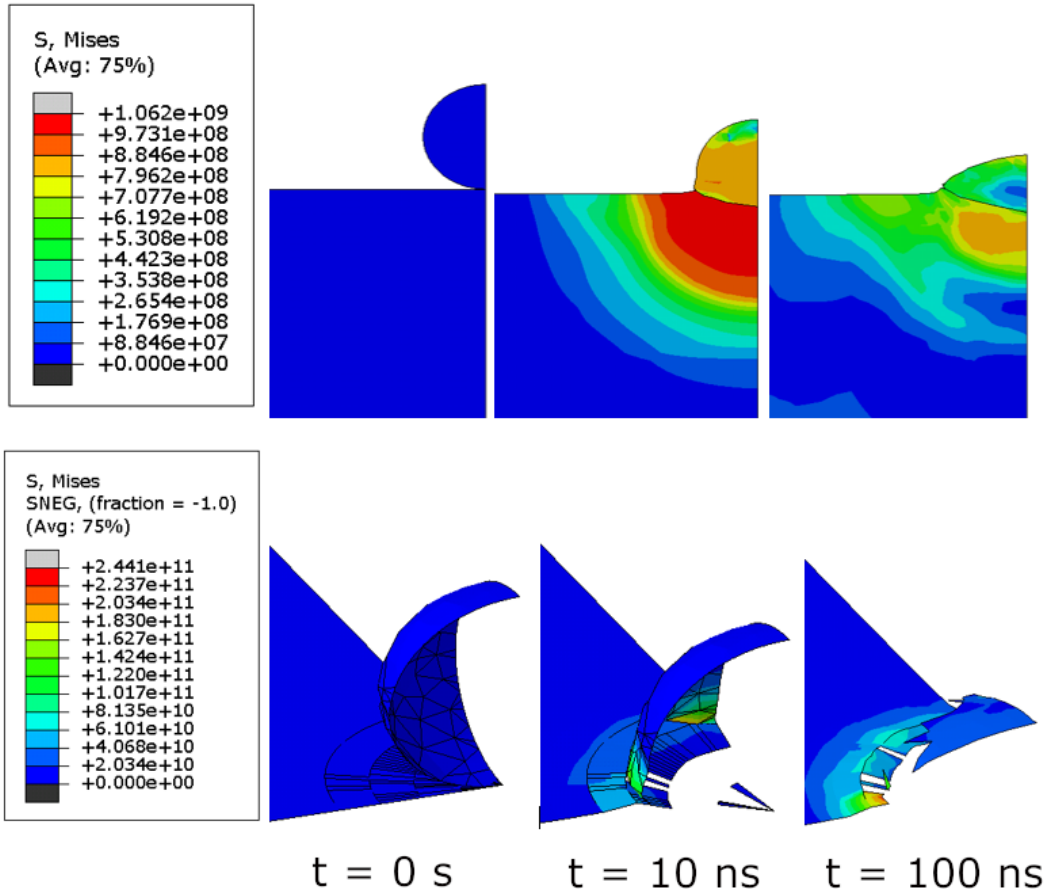


Figure 107: Stress evolution of Ti-6Al-4V particle impacting Ti-6Al-4V substrate with a titanium dioxide layer and using Johnson-Cook plasticity for Ti-6Al-4V<sup>13</sup>

Parameters for the BJC model were identical to those used in the JC model, with the exception of a  $C_2$  parameter of 0.029. This value was taken as the  $C_2$  value from the 6061 simulations and is used as a first approximation only. The author is unaware of any published data on the bilinear Johnson-Cook constant for Ti-6Al-4V. As was seen with the 6061 simulations, the BJC model for Ti-6Al-4V had similar stress concentrations, but higher overall Von Mises stress as a result of the additional hardening at higher strain rates.

<sup>13</sup> Model name "job1-imp1-ti64-ljc-400ksub"

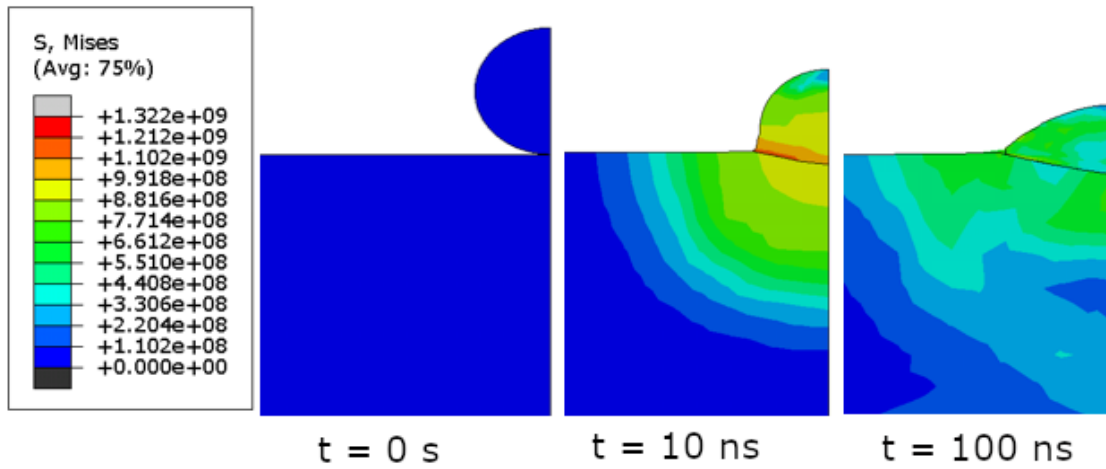


Figure 108: Stress evolution of an 800m/s Ti-6Al-4V particle impacting a Ti-6Al-4V substrate using bilinear Johnson-Cook plasticity<sup>14</sup>

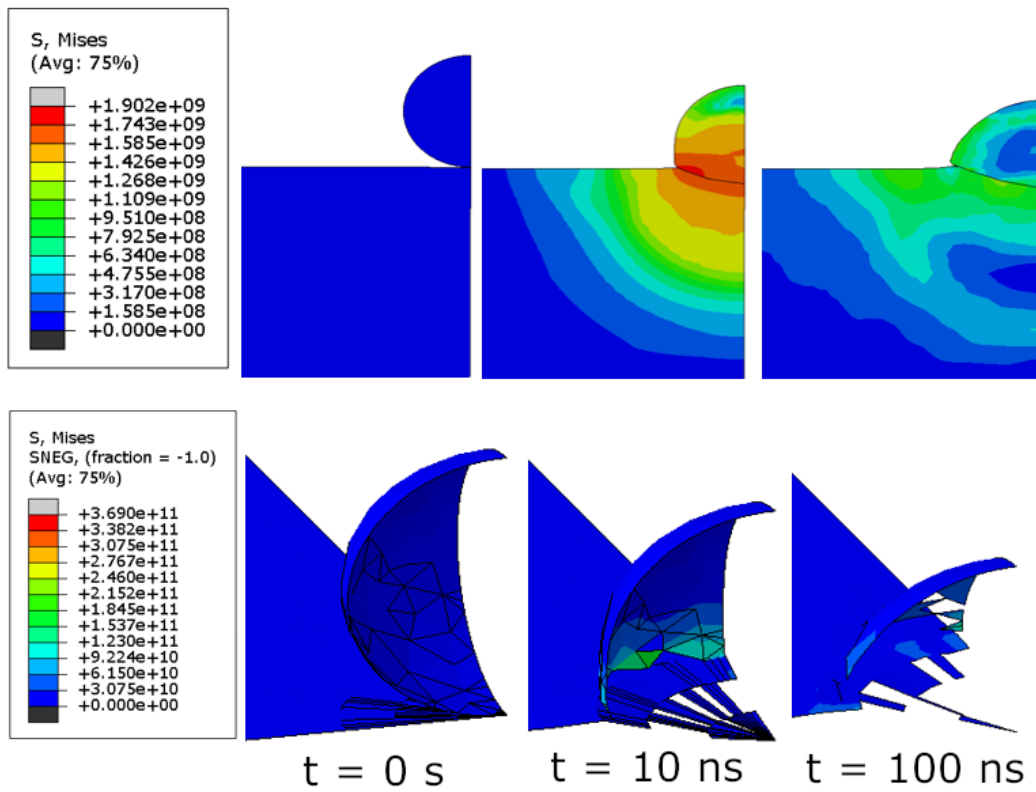


Figure 109: Stress evolution of an 800m/s Ti-6Al-4V particle impacting Ti-6Al-4V substrate with a titanium dioxide layer and using Johnson-Cook plasticity<sup>15</sup>

<sup>14</sup> Simulation name "bjc\_ti64"

<sup>15</sup> Simulation name "imp1-ti64-bjc-600k-v2"

When using a velocity of 1020 m/s (just above the reported critical velocity for Ti64 (Assadi et al. 2016), much more of the oxide layer is removed from the simulation. In fact, the oxide layer now appears similar to that for 6061 at its reported critical velocity.

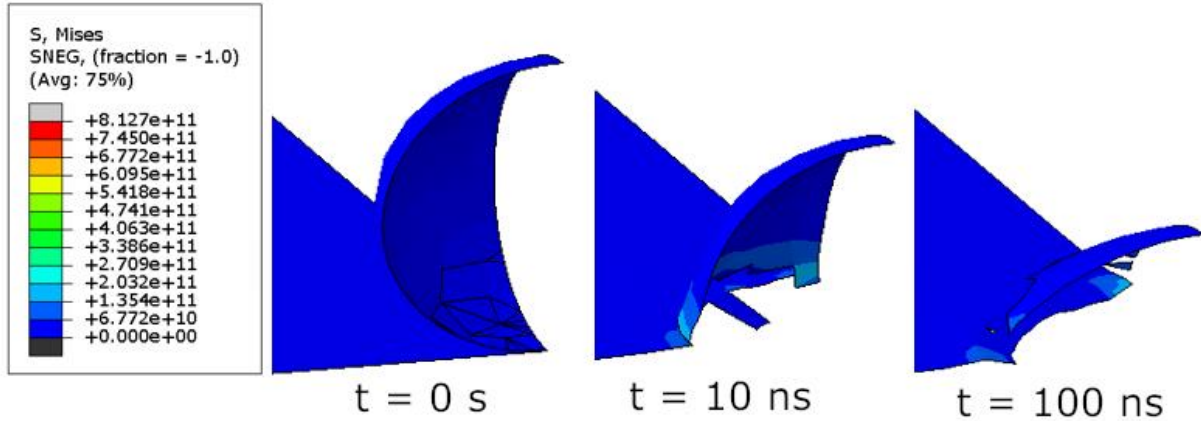


Figure 110: Stress evolution of a 1020 m/s Ti-6Al-4V particle oxide layer impacting Ti-6Al-4V substrate using bilinear Johnson-Cook plasticity<sup>16</sup>

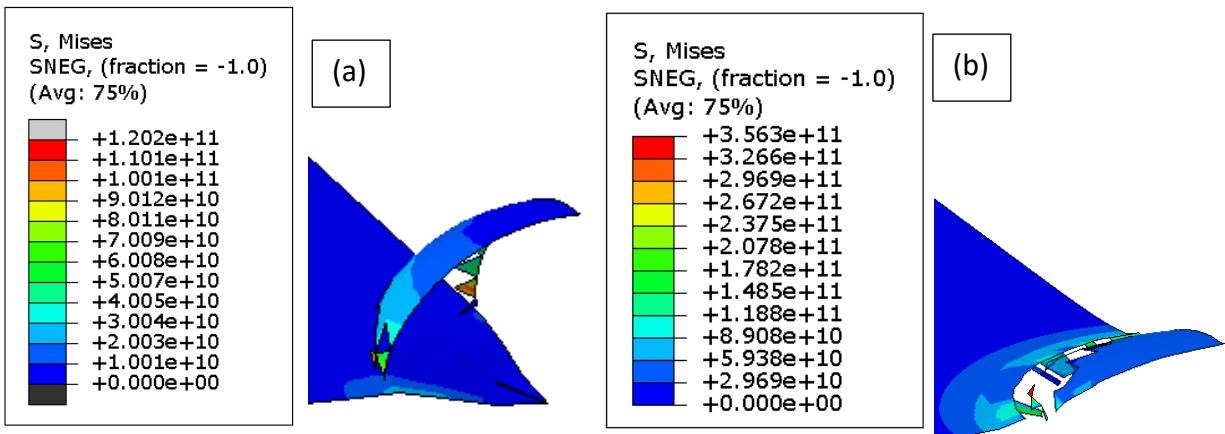


Figure 111: : Titanium oxide layer left after 100 ns in the bilinear Johnson-Cook simulation at 600 m/s (a)<sup>17</sup> and 1300 m/s (b)<sup>18</sup>

#### 4.5 Implications

Faster cooling rates also create significant microstructural differences between Ti64 powder and Ti64 bulk substrate. The plate and rod Ti64 substrates have equiaxed or elongated alpha grains, while the Ti64 powders have acicular structures. Frequently, martensitic microstructures have reduced ductility which is detrimental to cold spray bonding and mechanical properties. However, Matsumoto et al. (2011) have found increased ductility for acicular martensitic

<sup>16</sup> Simulation name "imp1-ti64-bjc-600k-1020ms"

<sup>17</sup> Simulation name "imp1-ti64-600k-600ms"

<sup>18</sup> Simulation name "imp1-ti64-600k-1300ms"

microstructures in Ti64, so the impact of the powder acicular structure is unclear. Ti-6Al-4V in general has some interesting stress-strain responses. Despite fractography showing less necking in Ti64 than 6061 aluminum alloy, the overall ductility was comparable or higher. The orientations of transformation alpha and retained beta reduce barriers to slip and can increase ductility (Wanhill and Barter 2012). Small scale Ti64 tensile specimens also produced accurate stress-strain responses after the grip size was increased to reduce slipping. Logically, indentation on commercially pure titanium produced less variability for a given hardness during indentation testing. Ti64 contains two phases with different hardness values which contribute to the additional measured variability. However, both the commercially pure titanium and Ti64 substrates displayed a strong indentation size effect. The nanoindentation simulation in Ti64 was set to the same depth as experimental measurements and the experimental pileup measurements matched closely with those for the simulation. Additionally, the simulation suggested a spacing to depth ratio of 13, which was slightly lower than that for the 6061.

The cold spray particle impact simulation was repeated for Ti64 with altered process conditions based off of experimental results. At the reported critical velocity for titanium of 800 m/s a large amount of oxide remained in the simulation. However, above the reported critical velocity of 1015 m/s for Ti-6Al-4V, there is much less remaining oxide in the simulation. This suggests the simulation may have value as a first approximation of velocities required for stronger bonding.

## [Chapter 5: Conclusions and Future Work](#)

### [5.1 Conclusions of 6061 Aluminum Alloy Findings](#)

A holistic approach was used for the study of these materials. Microstructural results in 6061 aluminum alloys provided insights into the mechanical properties observed experimental tests. Sites for ductile dimpling and much of the hardness variation at a given load can be explained through second phases present in the material. The 6061 powder on the other hand did not display iron-based inclusions and had grain boundaries an order of magnitude small than the wrought 6061 aluminum. Tensile and singled edged bend fatigue samples were developed to fit cold spray deposit thicknesses and tested for accuracy in wrought 6061. An indentation size effect was observed in both 6061-O and 6061-T6 alloys which allowed measurement of the hardness due to statistically stored dislocations, depth dependence of hardness, and the material length scale (see Table 19) using Nix and Gao mechanistic strain gradient plasticity. An FEA simulation of a used Berkovich nanoindenter tip was used to suggest a spacing between indents of at least 15 times the depth of the indent and predict pileup effects. A machine learning approach used an autoencoder to output an image of an indent, but more data is needed before the approach can be used to successfully predict hardness in the material based on image data. FEA simulations of a cold spray particle impact with oxide layers were used to provide first approximations of the impact of velocity on the remaining oxide layer. This information in turn can be used to make predictions about the strength of the bond between the particle and substrate.

### [5.2 Conclusions of Ti-6Al-4V Findings](#)

Microstructural work on Ti-6Al-4V bulk substrate as well as CP-Ti and Ti-6Al-4V powders showed significant microstructural differences between the bulk and powder forms. The annealed bulk Ti-6Al-4V plate had equiaxed alpha and discontinuous beta structures, while both of the powders displayed acicular structures inside of alpha phase titanium alloy. Sub-size tensile samples were developed and tested for bulk Ti64 substrate for future comparison with bulk cold sprayed Ti64. A strong ISE was observed in both Ti64 and CP-Ti substrates so that hardness due to statistically stored dislocations, depth dependence of hardness, and the material length scale (see Table 24) were successfully measured. Nanoindentation FEA simulations of a Berkovich indenter tip accurately predicted pile-up when compared to experimental AFM measurements. Simulation of the plastic zone size suggest a spacing to depth ratio of 13. A Ti-6Al-4V particle impacting a Ti-6Al-4V plate with oxide layers was simulated to provide information on the oxide damage behavior at different velocities.

### [5.3 Future Work](#)

The work discussed throughout the paper is intended to serve as the basis for additional work on these and other structural materials. The metallography work should be extended to bulk

cold sprayed 6061 and Ti64 alloys to better understand how the particles interact with the substrate and change after impact. Micro and nanohardness data and techniques are intended to serve as part of a larger database of material length scales for structural materials. Simulations of high strain gradient events such as nanoindentation and cold spray impacts should be done using the mechanistic strain gradient plasticity and the material length scales found in this work. The fracture and fatigue specimen designs should be used on bulk sprayed 6061 aluminum and Ti64 and the experimental test results should be compared with those for the wrought materials. Finally, the cold spray simulations should be extended to include multiple particle impacts

## References

1. "Alclad Aluminum 6061-T6, T651." Accessed Nov 1, 2018. <http://www.matweb.com/search/DataSheet.aspx?MatGUID=3a2e111b27ef4e5d813bad6044b3f318&ckck=1>.
2. A. Hall, P. Yang, L. Brewer, T. Buchheit. (2008). *Preparation and mechanical properties of cold sprayed nanocrystalline aluminum*. Sandia National Laboratories, Albuquerque, NM, USA
3. Altschuh, P., Yabansu, Y. C., Hötzer, J., Selzer, M., Nestler, B., & Kalidindi, S. R. (2017). Data science approaches for microstructure quantification and feature identification in porous membranes. *Journal of Membrane Science*, 540, 88–97. <https://doi.org/10.1016/j.memsci.2017.06.020>
4. Ambriz, R. R., Chicot, D., Benseddiq, N., Mesmacque, G., & de la Torre, S. D. (2011). Local mechanical properties of the 6061-T6 aluminium weld using micro-traction and instrumented indentation. *European Journal of Mechanics - A/Solids*, 30(3), 307–315. <https://doi.org/10.1016/j.euromechsol.2010.12.007>
5. Askeland, Donald R., and Wendelin J. Wright. *The Science and Engineering of Materials*. SI Edition, 7th. Cengage Learning, 2016.
6. ASM Handbook Committee. (1991). *Heat Treating of Aluminum Alloys*. In ASM Handbook, Volume 4: Heat Treating (Vol. 4, pp. 841–879). 10.1361/asmhba0001205
7. ASM International Handbook Committee. (1996). *ASM Handbook, Volume 19 - Fatigue and Fracture - 4.5 Aluminum Alloy Fracture Toughness*. ASM International. Retrieved from <https://app.knovel.com/hotlink/pdf/id:kt007RG351/asm-handbook-volume-19/aluminum-alloy-fracture>
8. ASM International Handbook Committee. (1996). *ASM Handbook, Volume 19 - Fatigue and Fracture - 4.7 Alpha and Alpha-Beta Alloys*. ASM International. Retrieved from <https://app.knovel.com/hotlink/pdf/id:kt007RG374/asm-handbook-volume-19/alpha-alpha-beta-alloys>
9. Assadi, H., Gärtner, F., Stoltenhoff, T., & Kreye, H. (2003). Bonding mechanism in cold gas spraying. *Acta Materialia*, 51(15), 4379-4394. doi:10.1016/s1359-6454(03)00274-x
10. Assadi, H., Kreye, H., Gärtner, F., & Klassen, T. (2016). Cold spraying—A materials perspective. *Acta Materialia*, 116, 382-407.
11. ASTM International. (2014). *ASTM B209M-14 Standard Specification for Aluminum and Aluminum-Alloy Sheet and Plate (Metric)*. Retrieved from <https://doi.org/10.1520/B0209M-14>
12. ASTM International. (2015). *ASTM B265-15 Standard Specification for Titanium and Titanium Alloy Strip, Sheet, and Plate*. Retrieved from <https://doi.org/10.1520/B0265-15>
13. ASTM International. (2016). *ASTM E8/E8M-16a Standard Test Methods for Tension Testing of Metallic Materials*. Retrieved from [https://doi.org/10.1520/E0008\\_E0008M-16A](https://doi.org/10.1520/E0008_E0008M-16A)
14. ASTM International. (2017). *ASTM E92-17 Standard Test Methods for Vickers Hardness and Knoop Hardness of Metallic Materials*. Retrieved from <https://doi.org/10.1520/E0092-17>
15. ASTM International. *ASTM E1820-18ae1 Standard Test Method for Measurement of Fracture Toughness*. West Conshohocken, PA; ASTM International, 2018. doi: <https://doi.org/10.1520/E1820-18AE01>

16. ASTM International. *B645-10(2015) Standard Practice for Linear-Elastic Plane–Strain Fracture Toughness Testing of Aluminum Alloys*. West Conshohocken, PA; ASTM International, 2015. doi: <https://doi.org/10.1520/B0645-10R15>
17. Balani, K., Agarwal, A., Seal, S., & Karthikeyan, J. (2005). Transmission electron microscopy of cold sprayed 1100 aluminum coating. *Scripta Materialia*, 53(7), 845–850. <https://doi.org/10.1016/j.scriptamat.2005.06.008>
18. Barsom, J. M., & Rolfe, S. T. (1999). *Fracture and fatigue control in structures: applications of fracture mechanics*.
19. Bathias. (2001). There is no infinite fatigue life in metallic materials. *Fatigue & Fracture of Engineering Materials & Structures*, 22(7). doi: 10.1046/j.1460-2695.1999.00183.x
20. Bedard, B. A., Flanagan, T. J., Ernst, A. T., Nardi, A., Dongare, A. M., Brody, H. D., Aindow, M. (2018). Microstructure and Micromechanical Response in Gas-Atomized Al 6061 Alloy Powder and Cold-Sprayed Splats. *Journal of Thermal Spray Technology*, 27(8), 1563-1578. doi:10.1007/s11666-018-0785-0
21. Bhattiprolu, V. S., Johnson, K. W., Ozdemir, O. C., & Crawford, G. A. (2018). Influence of feedstock powder and cold spray processing parameters on microstructure and mechanical properties of Ti-6Al-4V cold spray depositions. *Surface and Coatings Technology*, 335, 1-12. doi:10.1016/j.surfcoat.2017.12.014
22. Birt, A. M., Champagne, V. K., Sisson, R. D., & Apelian, D. (2015). Microstructural Analysis of Cold-Sprayed Ti-6Al-4V at the Micro- and Nano-Scale. *Journal of Thermal Spray Technology*, 24(7), 1277-1288. doi:10.1007/s11666-015-0288-1
23. Birt, A., Champagne, V., Sisson, R., & Apelian, D. (2015). Microstructural analysis of Ti-6Al-4V powder for cold gas dynamic spray applications. *Advanced Powder Technology*, 26(5), 1335-1347. doi:10.1016/j.apt.2015.07.008
24. Bock, F. E., Aydin, R. C., Cyron, C. J., Huber, N., Kalidindi, S. R., & Klusemann, B. (2019). A Review of the Application of Machine Learning and Data Mining Approaches in Continuum Materials Mechanics. *Frontiers in Materials*, 6. <https://doi.org/10.3389/fmats.2019.00110>
25. Brockenbrough, J. R., Bucci, R. J., Hinkle, A. J., Liu, J., & Magnusen, P. E. (1993). Role of Microstructure on Fatigue Durability of Aluminum Aircraft Alloys. doi: 10.21236/ada272116
26. Bushaev, V. 2017, Stochastic Gradient Descent with momentum. Retrieved from <https://towardsdatascience.com/stochastic-gradient-descent-with-momentum-a84097641a5d>
27. Cai, J., Li, F., Liu, T., & Chen, B. (2011). Investigation of mechanical behavior of quenched Ti-6Al-4V alloy by microindentation. *Materials Characterization*, 62(3), 287-293. doi:10.1016/j.matchar.2011.01.011
28. CES EduPack software, Granta Design Limited, Cambridge, UK, 2014 ([www.grantadesign.com](http://www.grantadesign.com))
29. Champagne, V. K. (2008). The Repair of Magnesium Rotorcraft Components by Cold Spray. *Journal of Failure Analysis and Prevention*, 8(2), 164-175. doi:10.1007/s11668-008-9116-y
30. Champagne, V. K., Helfritch, D. J., Trexler, M. D., & Gabriel, B. M. (2010). The effect of cold spray impact velocity on deposit hardness. *Modelling and Simulation in Materials Science and Engineering*, 18(6), 065011. doi:10.1088/0965-0393/18/6/065011

31. Champagne, V., & Helfritsch, D. (2014). Critical Assessment 11: Structural repairs by cold spray. *Materials Science and Technology*, 31(6), 627-634.  
doi:10.1179/1743284714y.0000000723
32. Champagne, Victor, and Blake Barnett. "Cold Spray Technology for DOD Applications." presented at the ASETS Defense 2012 : Workshop on Sustainable Surface Engineering for Aerospace and Defence, San Diego, CA, August 27, 2012.
33. Champagne, V. (2018). Investigation of the Effect of Oxides on the Critical Impact Velocity during the Cold Spray Process of High Purity Aluminum Powder (Unpublished master's thesis). Worcester Polytechnic Institute. Retrieved from <https://digitalcommons.wpi.edu/etd-dissertations/506/>
34. Choi, W., Li, L., Luzin, V., Neiser, R., Gnäupel-Herold, T., Prask, H., . . . Gouldstone, A. (2007). Integrated characterization of cold sprayed aluminum coatings. *Acta Materialia*, 55(3), 857-866.  
doi:10.1016/j.actamat.2006.09.006
35. Cizek, J., Kovarik, O., Siegl, J., Khor, K. A., & Dlouhy, I. (2013). Influence of plasma and cold spray deposited Ti Layers on high-cycle fatigue properties of Ti6Al4V substrates. *Surface and Coatings Technology*, 217, 23–33. doi: 10.1016/j.surfcoat.2012.11.067
36. Davis, S. O., Tupfer, N. G., & Niemi, R. M. (1968). Effect of specimen type and crack orientation on fracture toughness. *Engineering Fracture Mechanics*, 1(1), 213–233.  
[https://doi.org/10.1016/0013-7944\(68\)90026-X](https://doi.org/10.1016/0013-7944(68)90026-X)
37. Decision Tree Regression. (n.d.). Retrieved from [https://scikitlearn.org/stable/auto\\_examples/tree/plot\\_tree\\_regression.html](https://scikitlearn.org/stable/auto_examples/tree/plot_tree_regression.html)
38. DiMatteo, N. D. (1996). *Fatigue and fracture* (Vol 19), 785. Materials Park, OH: ASM International.
39. Donachie, M. J. (2002). *Titanium: A technical guide* (2nd ed.). Materials Park, OH: ASM International.
40. Dundurs, J. Discussion of 'Edge-Bonded Dissimilar Orthogonal Elastic Wedges Under Normal and Shear Loading', *J. Appl. Mech.*, Vol. 36 (1969), pp. 650–652.
41. Easton, M., & St. John, D. (2008). Improved prediction of the grain size of aluminum alloys that includes the effect of cooling rate. *Materials Science and Engineering: A*, 486(1-2), 8-13.  
doi:10.1016/j.msea.2007.11.009
42. Evans, A. G., Ri, M., Dalgleish, B. J., & Charalambides, P. G. (1990). The fracture energy of bimaterial interfaces. *METALLURGICAL TRANSACTIONS A*, 126(1–2), 53–64.
43. Fischer-Cripps, A. C. (2007). *Introduction to contact mechanics* (2nd ed). New York: Springer.
44. Freundchen (2015). *Pear interaction SEM english*. Wikimedia Commons  
[https://commons.wikimedia.org/wiki/File:Pear\\_interaction\\_SEM\\_english.svg](https://commons.wikimedia.org/wiki/File:Pear_interaction_SEM_english.svg)
45. Gadamchetty, G., Pandey, A., & Gawture, M. (2016). On Practical Implementation of the Ramberg-Osgood Model for FE Simulation. *SAE International Journal of Materials and Manufacturing*, 9(1), 200–205. <https://doi.org/10.4271/2015-01-9086>
46. Gavras, A. G., Lados, D. A., Champagne, V. K., & Warren, R. J. (2018). Effects of processing on microstructure evolution and fatigue crack growth mechanisms in cold-spray 6061 aluminum alloy. *International Journal of Fatigue*, 110, 49-62. doi:10.1016/j.ijfatigue.2018.01.006

47. Ghiles - Own work, CC BY-SA 4.0,  
<https://commons.wikimedia.org/w/index.php?curid=47471056>
48. Goldstein, J. (2017). *Scanning electron microscopy and x-ray microanalysis* (4th edition). New York, NY: Springer Science + Business Media, LLC.
49. Gouldstone, A., Koh, H. J., Zeng, K. Y., Giannakopoulos, A. E., & Suresh, S. (2000). Discrete and continuous deformation during nanoindentation of thin films. *Acta Materialia*, 48(9), 2277-2295.
50. Grujcic, M, C. L Zhao, W. S DeRosset, and D Helfritch. "Adiabatic Shear Instability Based Mechanism for Particles/Substrate Bonding in the Cold-Gas Dynamic-Spray Process." *Materials & Design* 25, no. 8 (December 1, 2004): 681–88. <https://doi.org/10.1016/j.matdes.2004.03.008>.
51. Gupta, R., Kumar, V. A., Mathew, C., & Rao, G. S. (2016). Strain hardening of Titanium alloy Ti6Al4V sheets with prior heat treatment and cold working. *Materials Science and Engineering: A*, 662, 537-550. doi:10.1016/j.msea.2016.03.094
52. Haghshenas, M., Wang, L., & Klassen, R. J. (2012). Depth dependence and strain rate sensitivity of indentation stress of 6061 aluminium alloy. *Materials Science and Technology*, 28(9-10), 1135–1140. doi: 10.1179/1743284712y.0000000019
53. Harrigan, M. J. et al., The Effect of Rolling Texture on the Fracture Mechanics of Ti-6Al-2Sn-4Zr-6Mo Alloy, *Titanium Science and Technology*, Vol 2, Plenum Press, 1973, p 1297- 1317
54. Hassani-Gangaraj, M., Veysset, D., Nelson, K. A., & Schuh, C. A. (2019). Impact-bonding with aluminum, silver, and gold microparticles: Toward understanding the role of native oxide layer. *Applied Surface Science*, 476, 528-532. doi:10.1016/j.apsusc.2019.01.111
55. Hatch, John. "Microstructure of Alloys." *ASM International Aluminum Properties and Physical Metallurgy* (1984): 58–104. <https://doi.org/DOI: 10.1361/appm1984p058>.
56. Henry, Scott D. Davidson, Grace M. Lampman, Steven R. Reidenbach, Faith Boring, Randall L. Scott, Jr., William W.. (1995). *Fatigue Data Book - Light Structural Alloys - 3.6 Fracture Toughness and Crack Growth*. ASM International. Retrieved from <https://app.knovel.com/hotlink/pdf/id:kt00ACYAP4/fatigue-data-book-light/fracture-toughness-crack>
57. Henry, Scott D. Davidson, Grace M. Lampman, Steven R. Reidenbach, Faith Boring, Randall L. Scott, Jr., William W.. (1995). *Fatigue Data Book - Light Structural Alloys - 5.1.3 Metallurgy of Beta Alloys*. ASM International
58. Hill, H. N. (1944). Determination of Stress-strain Relations from "Offset" Yield Strength Values. *Aluminum Company of America*, (927)
59. Hollomon, J. R. (1945). "Tensile deformation," *Transaction of American Institute of Mechanical Engineering*, vol. 162, pp. 268–277
60. Hysitron Service Document Probe Calibration. CSV-T-003 v3.0
61. James, Gareth, Daniela Witten, Trevor Hastie, and Robert Tibshirani. *An Introduction to Statistical Learning*. Vol. 103. Springer Texts in Statistics. New York, NY: Springer New York, 2013. <https://doi.org/10.1007/978-1-4614-7138-7>
62. Kaufman, J. Gilbert. (2008). *Properties of Aluminum Alloys - Fatigue Data and the Effects of Temperature, Product Form, and Processing - 5.1.5 5xxx Alloys*. ASM International.

63. Kay, Charles M., and J. Karthikeyan. *High Pressure Cold Spray: Principles and Applications*. ASM International, 2016.
64. Keech, P. G., Vo, P., Ramamurthy, S., Chen, J., Jacklin, R., & Shoesmith, D. W. (2014). Design and development of copper coatings for long term storage of used nuclear fuel. *Corrosion Engineering, Science and Technology*, 49(6), 425-430. doi:10.1179/1743278214y.0000000206
65. Khun, N. W., Tan, A. W. Y., & Liu, E. (2016). Mechanical and Tribological Properties of Cold-Sprayed Ti Coatings on Ti-6Al-4V Substrates. *Journal of Thermal Spray Technology*, 25(4), 715–724. <https://doi.org/10.1007/s11666-016-0396-6>
66. Klinkov, Sergei Vladimirovich, Vladimir Fedorovich Kosarev, and Martin Rein. “Cold Spray Deposition: Significance of Particle Impact Phenomena.” *Aerospace Science and Technology* 9, no. 7 (October 2005): 582–91. <https://doi.org/10.1016/j.ast.2005.03.005>.
67. Klinkov, Sergei Vladimirovich, Vladimir Fedorovich Kosarev, and Martin Rein. “Cold Spray Deposition: Significance of Particle Impact Phenomena.” *Aerospace Science and Technology* 9, no. 7 (October 2005): 582–91. <https://doi.org/10.1016/j.ast.2005.03.005>.
68. Lawn, B. (1993) *Fracture of Brittle Solids*, 2nd ed. Cambridge University Press, Cambridge, UK.
69. Lee, S., Saito, Y., Sakai, T., & Utsunomiya, H. (2002). Microstructures and mechanical properties of 6061 aluminum alloy processed by accumulative roll-bonding. *Materials Science and Engineering: A*, 325(1-2), 228-235. doi:10.1016/s0921-5093(01)01416-2
70. Lemiale, V., King, P., Rudman, M., Prakash, M., Cleary, P., Jahedi, M., & Gulizia, S. (2014). Temperature and strain rate effects in cold spray investigated by smoothed particle hydrodynamics. *Surface and Coatings Technology*, 254, 121–130. doi: 10.1016/j.surfcoat.2014.05.071
71. Lesuer, D. R., Kay, G. J., LeBlanc, M. M. (2001). *Modeling Large-Strain, High-Rate Deformation in Metals*
72. Lyman, T. (1972). *Atlas of microstructures of industrial alloys* (8th ed., Vol. 7). Metals Park, OH: ASM International.
73. Ma, Qing, and David R. Clarke. “Size Dependent Hardness of Silver Single Crystals.” *Journal of Materials Research* 10, no. 04 (April 1995): 853–63. <https://doi.org/10.1557/JMR.1995.0853>.
74. Matsumoto, H., Yoneda, H., Sato, K., Kurosu, S., Maire, E., Fabregue, D., ... Chiba, A. (2011). Room-temperature ductility of Ti–6Al–4V alloy with  $\alpha'$  martensite microstructure. *Materials Science and Engineering: A*, 528(3), 1512–1520. <https://doi.org/10.1016/j.msea.2010.10.070>
75. Mayer, H., Papakyriacou, M., Zettl, B., & Stanzl-Tschegg, S. (2003). Influence of porosity on the fatigue limit of die cast magnesium and aluminium alloys. *International Journal of Fatigue*, 25(3), 245–256. doi: 10.1016/s0142-1123(02)00054-3
76. Moridi, A., Hassani-Gangaraj, S., Vezzú, S., Trško, L., & Guagliano, M. (2015). Fatigue behavior of cold spray coatings: The effect of conventional and severe shot peening as pre-/post-treatment. *Surface and Coatings Technology*, 283, 247–254. doi: 10.1016/j.surfcoat.2015.10.063
77. Moridi, A., S. M. Hassani-Gangaraj, M. Guagliano, and M. Dao. “Cold Spray Coating: Review of Material Systems and Future Perspectives.” *Surface Engineering* 30, no. 6 (June 2014): 369–95. <https://doi.org/10.1179/1743294414Y.0000000270>.
78. Munagala, V. N., Akinyi, V., Vo, P., & Chromik, R. R. (2018). Influence of Powder Morphology and Microstructure on the Cold Spray and Mechanical Properties of Ti6Al4V Coatings. *Journal of Thermal Spray Technology*, 27(5), 827-842. doi:10.1007/s11666-018-0729-8

79. Nakai, M., & Itoh, G. (2014). The Effect of Microstructure on Mechanical Properties of Forged 6061 Aluminum Alloy. *Materials Transactions*, 55(1), 114-119.  
[doi:10.2320/matertrans.ma201324](https://doi.org/10.2320/matertrans.ma201324)
80. Neikov, O. D. (2009). *Handbook of non-ferrous metal powders: Technologies and applications* (1st ed.). Amsterdam: Elsevier. doi:978-1-85617-422-0
81. Neikov, O. D. (2019). Chapter 4—Atomization and Granulation. In O. D. Neikov, S. S. Naboychenko, & N. A. Yefimov (Eds.), *Handbook of Non-Ferrous Metal Powders (Second Edition)* (pp. 125–185). <https://doi.org/10.1016/B978-0-08-100543-9.00004-X>
82. Nesterov, Yuri 2004, Introductory Lectures on Convex Optimization. A Basic Course, Springer ISBN 1-4020-7553-7)
83. Nix, W. D., & Gao, H. (1998). Indentation size effects in crystalline materials: a law for strain gradient plasticity. *Journal of the Mechanics and Physics of Solids*, 46(3), 411-425.
84. Oh, S., & Ki, H. (2019). Deep learning model for predicting hardness distribution in laser heat treatment of AISI H13 tool steel. *Applied Thermal Engineering*, 153, 583–595.  
<https://doi.org/10.1016/j.applthermaleng.2019.01.050>
85. Olegalexandrov at English Wikipedia.derivative work: Zerodamage - This file was derived from: Gradient descent.png., Public Domain,  
<https://commons.wikimedia.org/w/index.php?curid=20569355>
86. Oliver, W., & Pharr, G. (2004). Measurement of hardness and elastic modulus by instrumented indentation: Advances in understanding and refinements to methodology. *Journal of Materials Research*, 19(1), 3–20. doi: 10.1557/jmr.2004.0002
87. Paffenroth, R 2019, *Class 2 lecture notes, MA463x: Statistical Learning*, Worcester Polytechnic Institute, delivered 12 March 2019.
88. Paris, P. C., Gomez, M. P., & Anderson, W. E. (1961). A rational analytic theory of fatigue. *The Trend in Engineering*.
89. Pattison, J., S. Celotto, R. Morgan, M. Bray, and W. O’Neill. “Cold Gas Dynamic Manufacturing: A Non-Thermal Approach to Freeform Fabrication.” *International Journal of Machine Tools and Manufacture* 47, no. 3–4 (March 2007): 627–34.  
<https://doi.org/10.1016/j.ijmachtools.2006.05.001>.
90. Phani, P., and W.C. Oliver. “A Critical Assessment of the Effect of Indentation Spacing on the Measurement of Hardness and Modulus Using Instrumented Indentation Testing.” *Materials & Design* 164 (February 2019): 107563. <https://doi.org/10.1016/j.matdes.2018.107563>.
91. Pharr, G. M., Herbert, E. G., & Gao, Y. (2010). The Indentation Size Effect: A Critical Examination of Experimental Observations and Mechanistic Interpretations. *Annual Review of Materials Research*, 40(1), 271–292. <https://doi.org/10.1146/annurev-matsci-070909-104456>
92. Picklum, M., & Beetz, M. (2019). MatCALO: Knowledge-enabled machine learning in materials science. *Computational Materials Science*, 163, 50–62.  
<https://doi.org/10.1016/j.commatsci.2019.03.005>
93. Polmear, Ian StJohn, David Nie, Jian-Feng Qian, Ma. (2017). *Light Alloys - Metallurgy of the Light Metals (5th Edition) - 4.4.2 Al-Cu-Mg Alloys (2xxx Series)*.Elsevier. Retrieved from  
<https://app.knovel.com/hotlink/pdf/id:kt011G5ZS1/light-alloys-metallurgy/al-cu-mg-alloys-2xxx>

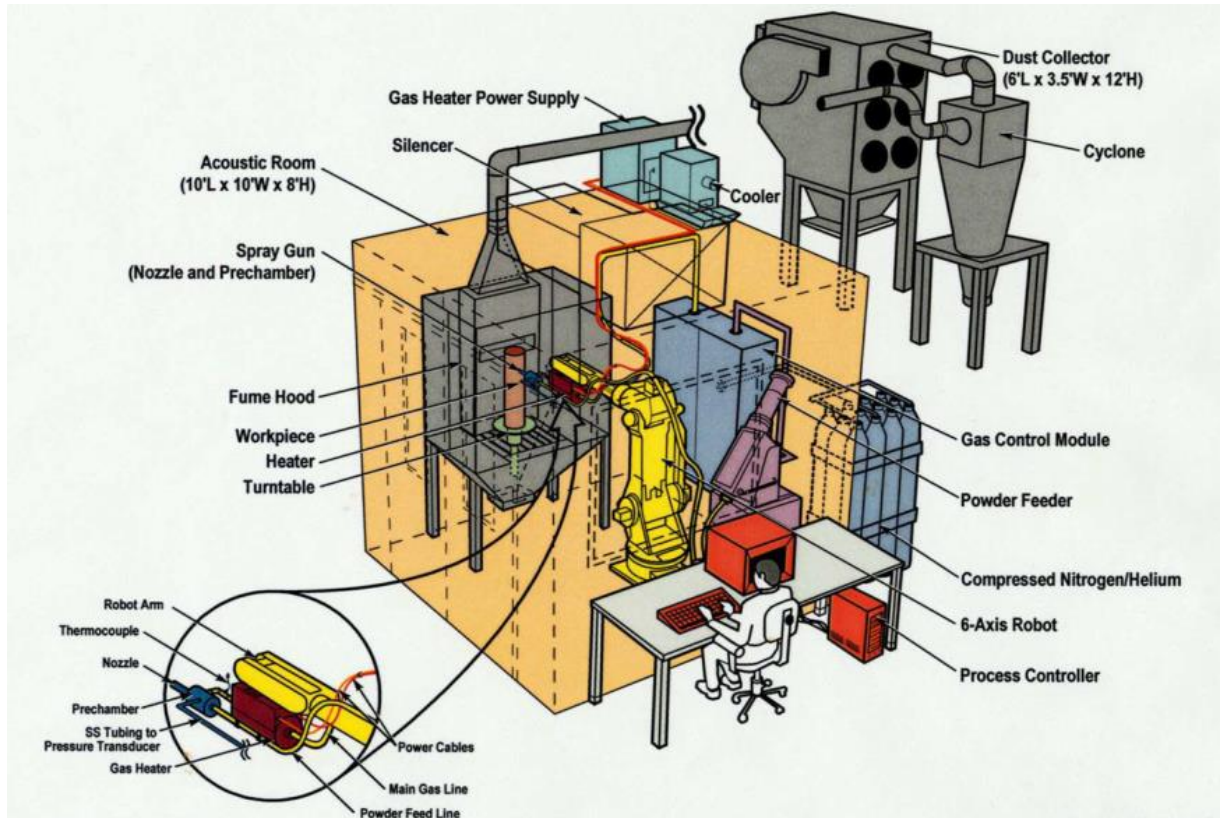
94. Price, T., Shipway, P., & McCartney, D. (2006). Effect of Cold Spray Deposition of a Titanium Coating on Fatigue Behavior of a Titanium Alloy. *Journal of Thermal Spray Technology*, 15(4), 507–512. doi: 10.1361/105996306x147108
95. Qiao, X. G., Starink, M. J., & Gao, N. (2010). The influence of indenter tip rounding on the indentation size effect. *Acta Materialia*, 58(10), 3690-3700.
96. R.J. Bucci, *Engineering Fracture Mechanics*, Vol 12, 1979, p 407-441
97. R.R. Ferguson and R.G. Berryman, "Fracture Mechanics Evaluation of B-1 Materials," Report AFML-TR-76-137, Vol I, *Rockwell International*, Los Angeles, 1976
98. Rahneshin, V. (2019). Bilinear Johnson-Cook Abaqus UMAT Code. Worcester Polytechnic University
99. Ramberg, W., & Osgood, W. R. (1943). Description of stress–strain curves by three parameters. *Technical Note No. 902*, National Advisory Committee For Aeronautics, Washington DC.
100. Rech, S., Trentin, A., Vezzù, S., Legoux, J., Irissou, E., & Guagliano, M. (2010). Influence of Pre-Heated Al 6061 Substrate Temperature on the Residual Stresses of Multipass Al Coatings Deposited by Cold Spray. *Journal of Thermal Spray Technology*, 20(1-2), 243-251. doi:10.1007/s11666-010-9596-7
101. Rech, S., Trentin, A., Vezzù, S., Vedelago, E., Legoux, J.-G., & Irissou, E. (2014). Different Cold Spray Deposition Strategies: Single- and Multi-layers to Repair Aluminium Alloy Components. *Journal of Thermal Spray Technology*, 23(8), 1237–1250. doi: 10.1007/s11666-014-0141-y
102. Reimann, D., Nidadavolu, K., ul Hassan, H., Vajragupta, N., Glasmachers, T., Junker, P., & Hartmaier, A. (2019). Modeling Macroscopic Material Behavior With Machine Learning Algorithms Trained by Micromechanical Simulations. *Frontiers in Materials*, 6. <https://doi.org/10.3389/fmats.2019.00181>
103. Ritchie, R. O. (1979). Near-threshold fatigue-crack propagation in steels. *International Materials Reviews*, 24(1), 205–230. doi: 10.1179/095066079790136381
104. Ritchie, R., & Knott, J. (1973). Mechanisms of fatigue crack growth in low alloy steel. *Acta Metallurgica*, 21(5), 639–648. doi: 10.1016/0001-6160(73)90073-4
105. Rokni, M. R., C. A. Widener, and V. R. Champagne. "Microstructural Evolution of 6061 Aluminum Gas-Atomized Powder and High-Pressure Cold-Sprayed Deposition." *Journal of Thermal Spray Technology* 23, no. 3 (December 2013): 514–24. <https://doi.org/10.1007/s11666-013-0049-y>.
106. Rokni, M. R., Nardi, A. T., Champagne, V. K., & Nutt, S. R. (2018). Effects of Preprocessing on Multi-Direction Properties of Aluminum Alloy Cold-Spray Deposits. *Journal of Thermal Spray Technology*, 27(5), 818-826. doi:10.1007/s11666-018-0723-1
107. Rokni, M., Widener, C., & Champagne, V. (2014). Microstructural stability of ultrafine grained cold sprayed 6061 aluminum alloy. *Applied Surface Science*, 290, 482-489. doi:10.1016/j.apsusc.2013.11.127
108. Rokni, M., Widener, C., Ozdemir, O., & Crawford, G. (2017). Microstructure and mechanical properties of cold sprayed 6061 Al in As-sprayed and heat treated condition. *Surface and Coatings Technology*, 309, 641-650. doi:10.1016/j.surfcoat.2016.12.035

109. Schmidt, Tobias, Frank Gärtner, Hamid Assadi, and Heinrich Kreye. "Development of a Generalized Parameter Window for Cold Spray Deposition." *Acta Materialia* 54, no. 3 (February 2006): 729–42. <https://doi.org/10.1016/j.actamat.2005.10.005>.
110. Sinha, V., Mercer, C., & Soboyejo, W. (2000). An investigation of short and long fatigue crack growth behavior of Ti–6Al–4V. *Materials Science and Engineering: A*, 287(1), 30–42. doi: 10.1016/s0921-5093(00)00817-0
111. Soboyejo, A., Foster, M., Mercer, C., Papritan, J., & Soboyejo, W. (1998). A New Multiparameter Model for the Prediction of Fatigue Crack Growth in Structural Metallic Materials. *Fatigue and Fracture Mechanics: 30th Volume*. doi: 10.1520/stp13412s
112. Soboyejo, Wole. *Mechanical Properties of Engineered Materials*. CRC Press, 2002. <https://doi.org/10.1201/9780203910399>.
113. Sun, W., Tan, A. W. Y., Khun, N. W., Marinescu, I., & Liu, E. (2017). Effect of substrate surface condition on fatigue behavior of cold sprayed Ti6Al4V coatings. *Surface and Coatings Technology*, 320, 452–457. doi: 10.1016/j.surfcoat.2016.11.093
114. Tan, A. W., Sun, W., Bhowmik, A., Lek, J. Y., Marinescu, I., Li, F., . . . Liu, E. (2018). Effect of coating thickness on microstructure, mechanical properties and fracture behaviour of cold sprayed Ti6Al4V coatings on Ti6Al4V substrates. *Surface and Coatings Technology*, 349, 303–317. doi:10.1016/j.surfcoat.2018.05.060
115. Tan, A. W., Sun, W., Phang, Y. P., Dai, M., Marinescu, I., Dong, Z., & Liu, E. (2017). Effects of Traverse Scanning Speed of Spray Nozzle on the Microstructure and Mechanical Properties of Cold-Sprayed Ti6Al4V Coatings. *Journal of Thermal Spray Technology*, 26(7), 1484-1497. doi:10.1007/s11666-017-0619-5
116. User A1, "Vickers Hardness Test." *Wikipedia*, December 25, 2018. [https://en.wikipedia.org/w/index.php?title=Vickers\\_hardness\\_test&oldid=875259643](https://en.wikipedia.org/w/index.php?title=Vickers_hardness_test&oldid=875259643).
117. User Jzahr, "Ramberg–Osgood relationship." *Wikipedia*, January 29, 2018. [https://en.wikipedia.org/wiki/Ramberg%E2%80%93Osgood\\_relationship](https://en.wikipedia.org/wiki/Ramberg%E2%80%93Osgood_relationship).
118. User Twisp, "Fracture mechanics." *Wikipedia*, 2008. [https://en.wikipedia.org/wiki/Fracture\\_mechanics](https://en.wikipedia.org/wiki/Fracture_mechanics).
119. Vo, P., Irissou, E., Legoux, J., & Yue, S. (2013). Mechanical and Microstructural Characterization of Cold-Sprayed Ti-6Al-4V After Heat Treatment. *Journal of Thermal Spray Technology*, 22(6), 954-964. doi:10.1007/s11666-013-9945-4
120. Voort, V. (2004). *Metallography and microstructures (Vol. 9)*. Metals Park, OH: American Society for Metals.
121. Wanhill, Russell, and Simon Barter. "Metallurgy and Microstructure." In *Fatigue of Beta Processed and Beta Heat-Treated Titanium Alloys*, by Russell Wanhill and Simon Barter, 5–10. Dordrecht: Springer Netherlands, 2012. [https://doi.org/10.1007/978-94-007-2524-9\\_2](https://doi.org/10.1007/978-94-007-2524-9_2).
122. Weaver, J. S., Khosravani, A., Castillo, A., Kalidindi, S. R.; 2016; Tensile and Microindentation Stress-Strain Curves of Al-6061; NIST; <http://dx.doi.org/10.17021/1265166>
123. Wiso - from en: Image: Neural network example.svg, vectorialization of en: Image: Neural network example.png, Public Domain, <https://commons.wikimedia.org/w/index.php?curid=5084582>

124. Yang, M. (2019, March 28). Refractory Metal Powders. Lecture, Worcester Polytechnic University.
125. Yovanovich, Milan. "Micro and Macro Hardness Measurements, Correlations, and Contact Models." In *44th AIAA Aerospace Sciences Meeting and Exhibit*. Reno, Nevada: American Institute of Aeronautics and Astronautics, 2006. <https://doi.org/10.2514/6.2006-979>.
126. Zehnder, A. T. (2012). *Fracture mechanics*. London ; New York: Springer Science + Business Media.
127. Zheng, B., Lin, Y., Zhou, Y., & Lavernia, E. J. (2009). Gas Atomization of Amorphous Aluminum Powder: Part II. Experimental Investigation. *Metallurgical and Materials Transactions B*, 40(6), 995-1004. doi:10.1007/s11663-009-9277-4
128. Ziemian, C., Sharma, M., Bouffard, B., Nissley, T., & Eden, T. (2014). Effect of substrate surface roughening and cold spray coating on the fatigue life of AA2024 specimens. *Materials & Design (1980-2015)*, 54, 212–221. doi: 10.1016/j.matdes.2013.08.061
129. Zong, Z. and Soboyejo, W. "Indentation Size Effects in Face Centered Cubic Single Crystal Thin Films." *Materials Science and Engineering: A* 404, no. 1–2 (September 2005): 281–90. <https://doi.org/10.1016/j.msea.2005.05.075>.
130. Zong, Z., J. Lou, W. O. Soboyejo. Size effects on the Nano- and Micro-Hardness of [001] Oriented FCC Single Crystals. *ASME*

## Appendix

### A1.1 Additional Reference Images



Setup Diagram for a Typical Robotically Controlled Cold Spray Cell (Kay and Karthikeyan 2016)